Schmincke, H.-U., Weaver, P.P.E., Firth, J.V., et al., 1995
Proceedings of the Ocean Drilling Program, Initial Reports, Vol. 157

6. SITE 952[1]

Shipboard Scientific Party[2]

HOLE 952A

Date occupied: 15 August 1994

Date departed: 20 August 1994

Time on hole: 5 days

Position: 30°47.449′N, 24°30.574′W

Bottom felt (drill-pipe measurement from rig floor, m): 5442.7

Distance between rig floor and sea level (m): 10.90

Water depth (drill-pipe measurement from sea level, m): 5431.8

Total depth (from rig floor, m): 5868.60

Penetration (m): 425.90

Number of cores (including cores having no recovery): 45

Total length of cored section (m): 425.90

Total core recovered (m): 415.18

Core recovery (%): 97.5

Oldest sediment cored:
Depth (mbsf): 425.90
Nature: clay with nannofossils
Earliest age: middle Miocene

Principal results: Site 952 is located in the southeastern Madeira Abyssal Plain at 30°47.45′N, 24°30.57′W, at a water depth of 5431.8 m in the Cruiser Fracture Zone Valley. Seismic profiles for the area show the same major units as at Sites 950 and 951: an upper unit (0–450 ms) showing relatively high amplitude parallel reflectors and a lower unit which drapes the basement highs. The upper unit can be subdivided into three subunits by relatively strong reflectors at 160 ms and 245 ms. Reflectors within the lower two subunits are weaker than in the upper subunit. This seismic pattern, previously described by Searle (1987), is interpreted as pelagic drape over basement, with the deeper draped sequences being later infilled by rapidly accumulated turbidites.

In combination with the other two abyssal plain sites, the primary objective of this site was to determine the nature of the turbidite fill and to distinguish discrete sources for the various compositional groups of sediment flows. Our objective is to correlate individual turbidite units between the three sites and tie them to the downhole log data and thereby to the extensive seismic profile network on the abyssal plain. This will enable mapping of individual flows or groups of flows, calculations of their volumes, and, in combination with the stratigraphic data, estimates of the amount of sediment contributed from each source since the inception of the plain. A secondary objective at all three sites involved determination of the long-term effects of sediment burial and diagenesis in a sequence of mixed volcanic, organic-rich, and organic-poor sediments.

Hole 952 was drilled to 425.9 mbsf and a total of 15 APC cores (0–142.8 mbsf) and 30 XCB cores (142.8–425.9 mbsf) were retrieved with average recovery rates of 100.6% and 95.9%, respectively. The hole was logged with the quad combo tool between 76 and 295 mbsf.

The sedimentary sequence at Site 952 comprises only one lithologic unit that is comparable to Unit I at Sites 950 and 951. This unit (0–425.9 mbsf) consists of Pleistocene to middle Miocene (0–13 Ma), thick clayey nannofossil mixed sediment and nannofossil clay turbidites, interbedded with pelagic nannofossil oozes, mixed sediments, and clays. The unit has been subdivided into two subunits (Ia and Ib) based on the proportion of calcium carbonate in the pelagic interbeds. Below 100 mbsf (Unit Ib) the pelagic interbeds are all clays. The three primary types of turbidites seen at Sites 950 and 951 are again present: volcaniclastic from the volcanic islands within the basin, organic-rich from the northwestern African margin, and calcareous from seamounts to the west of the plain. Above 243 mbsf all three turbidite types are well represented, but below this depth the turbidites become much thinner with less numerous volcaniclastic and calcareous units. The organic-rich turbidites below about 225 mbsf contain siliceous microfossils (diatoms and sponge spicules), and they are separated by very thin or absent pelagic layers suggesting frequent input of flows. The siliceous components were identified in the deeper turbidites at Site 951 but were not present at Site 950.

Several thick bedded sands occur between 380 and 405.5 mbsf grading up into thick turbidite muds. These contain a mixed assemblage of volcanic and continental minerals suggesting an origin from the east. A distinctive gray to white turbidite with a thick calcareous sand at its base occurs from 373.7 to 377.6 mbsf at Site 952 and appears identical to a unit between 318.5 to 320 mbsf at Site 951. The thick and sandy turbidites between 373.7 and 389 mbsf appear to correlate with the base of seismic Unit A.

Magnetostratigraphy gave a reversal sequence from the Brunhes to the top of the Gauss (C1n–C2An) in the pelagic units between the turbidites. This was the same length of record as in the previous two sites and correlates with the interval of thicker pelagic intervals resulting from the better preservation of calcium carbonate since 2.6 Ma, which was caused by a deepening of the CCD at this time. Planktonic foraminifers provide useful biostratigraphic data from the well-preserved carbonates in the upper 75 m of Hole 952A, but nannofossils were found in pelagic layers to 266 mbsf. Below this, turbidites were sampled to the base of the hole, and the FO of *Discoaster kugleri* was found at 342.8 mbsf indicating an age of around 12.2 Ma. The deepest sediment examined at 415.35 mbsf contains *Reticulofenestra pseudoumbilicus* suggesting an age for this level near the base of the hole of less than 13.1 Ma.

Sediment accumulation rates for the pelagic interbeds average 4.3 m/m.y. from zero to 2.6 Ma and 1.3 m/m.y. from 2.6 to 5.04 Ma. The rate from zero to 2.6 Ma is almost identical to that at Site 951, but it is less than the 5.6 m/m.y. recorded at Site 950. The rate between 2.6 and 5.04 Ma is slightly lower than at Site 950 (1.5 m/m.y.) and considerably less than at Site 951 (2.0 m/m.y.). The total sediment sequence has an accumulation rate of 31.1 m/m.y. from 0 to 5.56 Ma and probably a similar rate beyond 5.56 Ma, although in this interval the estimate is poorly constrained. This rate is similar to those at Sites 950 and 951 for the interval 0–6.5 Ma. At Site 950 from 6.5 to 13.5 Ma rates varied from 9 to 21 m/m.y. This may indicate that the deeper turbidite sequence is different between Sites 950 and 952, and indeed these deeper sediments show many more thin turbidites at Site 952.

Geochemical data obtained at Site 952 correspond very closely to those already described at Sites 950 and 951. Significant differences relate to sulfate reduction-controlled profiles of pore-water sulfate, ammonia, and alkalinity, which are more strongly developed at Site 952, indicating increased rates of sulfate reduction.

[1] Schmincke, H.-U., Weaver, P.P.E., Firth, J.V., et al., 1995. *Proc. ODP, Init. Repts.,* 157: College Station, TX (Ocean Drilling Program).

[2] Shipboard Scientific Party is given in the list preceding the table of contents.

Site 952 is the only one of the Madeira Abyssal Plain sites to yield significant quantities of headspace methane, with over 30,000 ppm being recorded below 400 mbsf, together with significant ethane and increasing C_1/C_2 ratios. These data provide evidence of diagenetic methanogenesis below the cored interval, probably within a continuation of the thinly bedded organic-rich turbidites that occur at the base of Hole 952A. The anomalously high rates (for a deep-water, open-ocean site) of bacterially mediated diagenesis occurring in MAP sediments is a consequence of the high organic matter content (typically around 2% C_{org}) of the buried turbidite sequence.

Physical properties data from Site 952 revealed a similar pattern to that seen at Sites 950 and 951. *P*-wave velocities correlate well with the gamma-ray porosity and are inversely correlated with the magnetic susceptibility. Peaks in the magnetic susceptibility are related to negative kicks in velocity, and both are caused by the volcanic turbidites interspersed within the sequence. Cross-plots of these measurements at common depths below seafloor may provide a means to discriminate different lithologies and recognize intermediate mixtures of independent components. Index properties data show a distinctive change in the average porosity below ~370 m as a result of the introduction of coarser sands and occasional debris flows below this level. This change in density supports the inference that Hole 952A penetrated the prominent reflector seen in the site survey data.

Despite encountering difficult logging conditions, downhole logs were successfully recorded down to ~290 mbsf with the quad combination tool string. The logs appear to be of good quality and they characterize the thick sequence of interbedded turbidites; the natural gamma-ray logs delineate the varying clay and carbonate composition of the turbidites. Comparison of the downhole logging data from Sites 950 and 952 show that there is an excellent correlation, providing an unequivocal means of high resolution depth correlation, and hence sedimentation rate variations, between the two sites.

The age of the widespread reflector at the base of the main turbidite sequence again approximates 13 Ma and is represented at Site 952 by the series of thick sands and breccia beds. Below this, however, the fracture zone valley appears to be filled with thin green organic-rich turbidites. The reflector may therefore indicate a change from input of small turbidity flows to larger flows that rapidly filled the deeps in the seafloor and spread to form the present broad abyssal plain. Numerous turbidite units can be correlated between all three sites; the seismic network will allow us to map them across the whole abyssal plain, which will enable estimations of their volumes and ultimately calculations of volumes of sediment added to the plain from each of the main sources over the last 15 m.y.

BACKGROUND AND OBJECTIVES

Site 952 is the third of three sites on the Madeira Abyssal Plain aimed at determining the history of sediment mass wasting within the Canary Basin. It lies 69 nmi south-southeast of Site 951 and 65.5 nmi east-southeast of Site 950 (Fig. 1 in "Site 950" chapter, this volume), in the same Cruiser Fracture Zone Valley as Site 950, near the eastern edge of the abyssal plain. This position is therefore more proximal to turbidity currents derived from that part of the northwestern African continental margin south of the Canary Islands and more distal to turbidity currents derived from the seamount chain to the west of the plain. These differences should be reflected by coarser and thicker graded bases to flows from the African margin and finer and thinner graded bases to flows from the west. As at the previous two sites, all seismic reflectors are well developed at this site and the turbidite sequence has about the same thickness. The data from this site will be integrated with data from the other two MAP sites to determine the volumes of individual turbidites and their emplacement ages.

Principal objectives included determination of the nature of the turbidite fill of the abyssal plain and identification of single turbidite units that can be correlated between the three abyssal plain sites. This site was logged, enabling individual turbidites, or groups of turbidites, to be linked to particular reflectors and correlated across the whole plain. This, in turn will allow estimates of volumes of reworked sediment contributed to the abyssal plain through time. Secondary objectives included the following: (1) identifying the volcaniclastic turbidites and their frequencies to determine periods of instability on the Canary and Madeira Islands, and (2) determining the long-term effects of sediment burial and diagenesis in a sequence of mixed volcanic, organic-rich and organic-poor sediments.

UNDERWAY GEOPHYSICS

On our approach to Site 952 an ~17-km-long reflection seismic profile was acquired starting at 30°54′N, 24°32′W and ending at 30°45′N, 24°30′W. An 80 $in.^3$ water gun was used as a seismic source and the signals were recorded on a single channel streamer and displayed on line-scan recorders for immediate inspection. The shot interval was 12 s corresponding to a distance of ~35 m. Data were stored digitally on 8 mm tape and subsequently processed by means of the SIOSEIS software. The processing sequence was as follows: bandpass filter (60–120 Hz), automatic gain control (500 ms window), finite difference migration, bandpass filter (60–120 Hz), trace mix (weights 1 2 1), display (every second trace). The processed profile is shown in Figure 1.

The acoustic basement, most likely basement rocks below the sediments, dips southward from 800 to 1500 ms below the seafloor reflector. Based on internal reflector configurations, three major units, Units A, B, and C, can be discerned in the sediments (Fig. 1). The upper Unit A is characterized by an abundance of horizontal or nearly horizontal reflectors, which drape over the basement high in the northern part of the profile. The base of Unit A is defined by a high-amplitude reflector at ~450 ms. Internally Unit A can be divided into three subunits, Subunits A1, A2, and A3. In Subunit A1, reflectors have high amplitudes and are coherent and horizontal. Subunit A2 has a nearly transparent upper part and a lower part with three parallel and coherent reflectors. The base of the subunit is defined by the lowermost of these reflectors. The thicknesses of Subunits A1 and A2 are approximately 160 and 85 ms respectively.

Subunit A3 has a thickness of ~220 ms at Site 952, but it thins over the basement high. Subunit A3 is almost transparent, but a couple of low-amplitude reflectors can be discerned. Close above the base an incoherent reflector with relatively high amplitude occurs.

Subunits A2 and A3 are affected by a small normal fault downfaulted to the north toward the top of the basement high (Fig. 2).

Unit B has a thickness of ~350 ms, somewhat decreasing toward the basement high. The internal reflector pattern in the upper 100 ms is rather complex varying from parallel to shingled and chaotic patterns. At Site 952 the pattern is parallel. Unit B is flexured in a 3–4 km wide zone from the flank of the basement high. Internal reflectors onlap the flexured, southward dipping base of the unit (Fig. 2). The onlap indicates a preexisting topography and the flexure indicates a postdepositional deformation. The thickness of Unit C increases southward from ~100 ms to ~700 ms. A few reflectors that can be discerned in the upper half of Unit C onlap the basement high.

Based on a combination of MST velocities and velocities obtained from the sonic logs a two-way traveltime–depth relationship was established, as shown in Figure 3. The depth for Subunits A1 and A2 has been calculated by means of this relation. Depths for deeper levels have been estimated by assuming the same velocity gradient as found at Site 950.

OPERATIONS

Site 951 to Site 952 Transit

The 69 nmi voyage to Site 952 (MAP-3) was made at an average speed of 10.3 kt. At 0815, local time, 15 August, the vessel slowed to

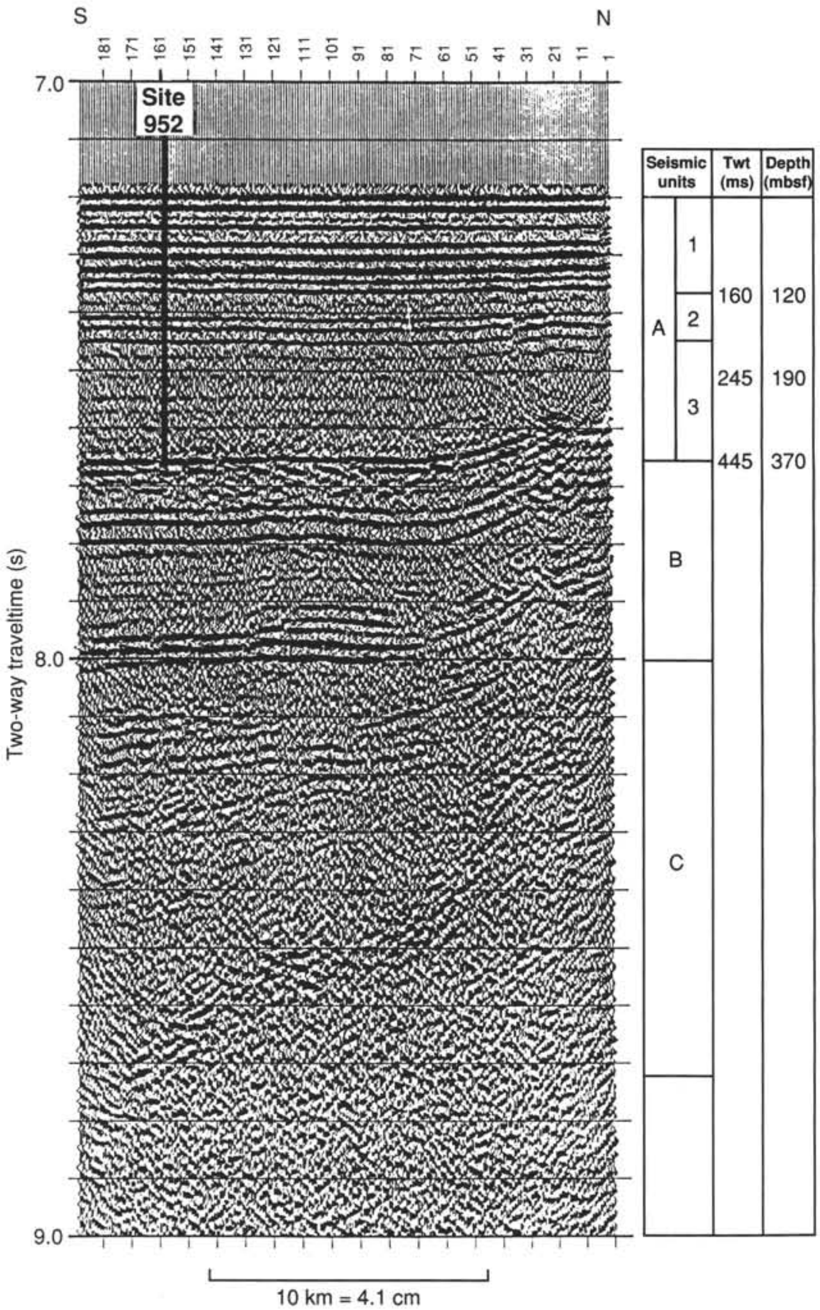

Figure 1. Processed seismic profile acquired during approach to Site 952. The two-way traveltimes and depths (in milliseconds and meters below seafloor) refer to Site 952.

6.5 kt and conducted a short survey over the MAP area. By 1100, the survey had been completed and the beacon was dropped on location at 1101.

Hole 952A (MAP-3)

The standard short-collar APC/XCB BHA used on the previous sites was made up with the LFV for logging. Core 1H recovered 9.82 m of nannofossil ooze (Table 1) and established the mud line at 5431.8 mbsl. APC coring advanced to 142.8 mbsf (Core 15H) and recovered 143.7 m (100.6% recovery). Coring continued with the XCB assembly after Core 15H did not extend to full stroke. Cores 3H to 15H were oriented. Coring with the XCB system advanced to total depth (TD) at 425.9 mbsf with excellent recovery (95.9%). The total recovery for the hole was 97.5%. Because all the subsequent sites of the leg are in shallower water, the coring line was coated with a preservative from 5868 to 3500 m while retrieving Core 45X.

At 1430, 18 August, the hole was flushed with 30 bbl of sepiolite mud. The first wiper trip found 18 m of fill at the bottom of the hole. The hole was washed and reamed to 425.9 mbsf (TD). Another treatment of mud followed, and the pipe was then pulled up to logging depth (92 mbsf).

At 2230, 18 August, the logging equipment was rigged up and the quad combo tool assembled. Despite the difficult hole conditions encountered, downhole logs were successfully recorded with the quad combination tool string down to approximately 290 mbsf. The quad tool string comprising NGT, LSS, CNT, HLDT, and DIT was deployed on three separate occasions with drill pipe set at different levels in an attempt to pass obstructions in the borehole. The initial deployment reached a depth of 202 mbsf and data were recorded

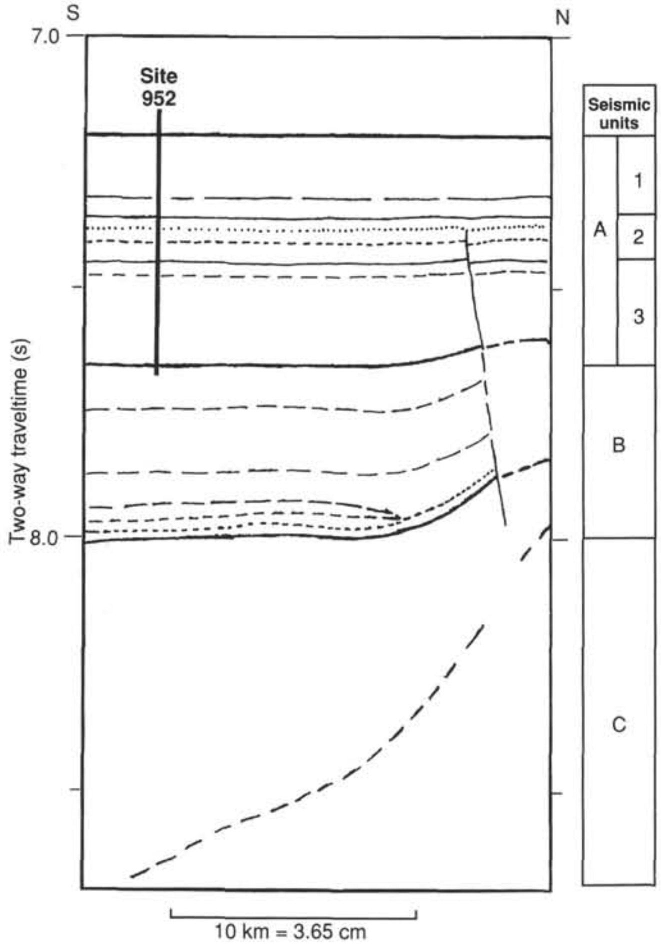

Figure 2. Structural and seismic-stratigraphic interpretation of the seismic profile at Site 952.

from here to the end of pipe at 76 mbsf. The tool string was then removed from the hole and the pipe was reset below the obstruction at 207 mbsf and the tool deployed again. A secondary obstruction was encountered at 293 mbsf and data were recorded from this depth to 179 mbsf. The tool string was removed from the hole for a second time and the hole flushed with 50 bbl of sepiolite in an attempt to log the bottom section of the hole. The pipe was reset at 304 mbsf and the tool string deployed again, but no significant progress could be made down into open hole from the end of the drill string. Logging operations were then terminated owing to time constraints.

After the logging equipment was rigged down, the drill pipe was started out of the hole at 2400, 19 August. Concurrent with the pulling of the pipe, the beacon was recalled, recovered, and on deck at 0420, 20 August. The drilling equipment was secured and the thrusters and hydrophones retracted by 1100, 20 August, as the vessel began the transit to the VICAP area.

LITHOSTRATIGRAPHY

Sedimentary units recovered at Site 952 consist of 425 m of distal turbidite deposits and interbedded pelagic ooze and clay ranging in age from Pleistocene to middle Miocene. Turbidite deposits in the upper part of the cored interval (0–225 mbsf) are composed dominantly of interbedded green and gray clayey nannofossil mixed sediment and white nannofossil ooze (Figs. 4 and 5). Turbidite deposits

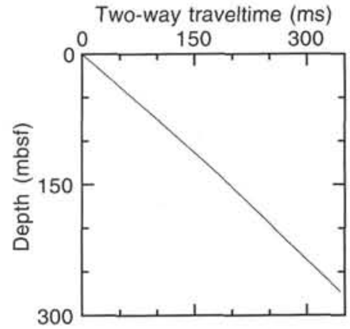

Figure 3. Relationship between depth and two-way traveltime, measured from the seafloor reflector.

in the lower part of the cored sequence (225–425 mbsf) are generally green clay with nannofossils and/or clay with siliceous microfossils (Figs. 4 and 5). This downward change in the lithology has been observed at Sites 950 and 951 and is reflected in the decreasing calcium carbonate content with depth (Fig. 6). The turbidite deposits in the upper 100 m are separated by thin interbeds of pelagic nannofossil ooze, clayey nannofossil mixed sediment, and clay. Below 100 mbsf, the pelagic sediments are generally clay to clay with nannofossils. The sedimentary sequence recovered at Site 952 is generally correlative to Unit I in Sites 950 and 951 (see "Lithostratigraphy," Sites 950 and 951, this volume). As in the previous sites, Unit I has been separated into two subunits, Ia and Ib, based on a decrease in calcium carbonate content in the pelagic deposits. At both Sites 952 and 951, siliceous microfossils (diatoms and sponge spicules) increase in abundance within Subunit Ib, but are absent in Subunit Ib at Site 950. Interbedded within Subunit Ib at Site 952 are several poorly sorted silty sand and matrix-supported clay clast breccia beds, representing coarse turbidite and debris flow deposits, referred to herein as Subunit Ib1 (Fig. 4).

Unit I

Interval: Sections 157-952A-1H-1 through 157-952A-45X-CC
Depth: 0–425 mbsf

Unit I is a minimum of 425 m thick at Site 952 and consists of interbedded green, gray, and white turbidites separated by thin pelagic deposits. The overall lithologic characteristics of these turbidite and pelagic deposits are generally the same as those described in the "Lithostratigraphy" section of the "Site 950" chapter (this volume) and will not be reiterated in this chapter; the reader is referred to the Unit 1 subheading of that chapter section (this volume) for a complete description of the general lithologies. Here we address some of the significant lithologic and stratigraphic similarities and differences between Site 952, and Sites 950 and 951.

Calcium Carbonate Content

A decrease in $CaCO_3$ content occurs in the pelagic sediments at approximately 100 mbsf (Fig. 6) and marks the compositional change from clayey nannofossil mixed sediments to clay. Thus, the boundary between Subunits Ia and Ib is placed at 100 mbsf. A similar compositional change in the green, organic-rich and gray, volcanic-rich turbidites from clayey nannofossil mixed sediment to clay with nannofossils and clay with siliceous microfossils occurs between 230 and 290 mbsf (Figs. 4 and 6).

In all three of the Madeira Abyssal Plain (MAP) drill sites the decrease in $CaCO_3$ is generally at the same depths. Pelagic sediments within the MAP sites below 100–150 mbsf contain <10% $CaCO_3$. Individual green turbidite beds show considerable variability but there

Table 1. Coring summary, Hole 952A.

Core	Date (August 1994)	Time (UTC)	Sub-bottom (m) Top	Sub-bottom (m) Bottom	Cored (m)	Recovered (m)	Recovery (%)	Section	Length (m)	Depth (mbsf) Top	Depth (mbsf) Bottom	Samples
157-952A-												
1H	15	2330	0.0	9.8	9.8	9.82	100.0					
								1	1.50	0.00	1.50	
								2	1.50	1.50	3.00	
								3	1.50	3.00	4.50	
								4	1.50	4.50	6.00	IW 145–150
								5	1.50	6.00	7.50	HS 0–5
								6	1.50	7.50	9.00	
								7	0.55	9.00	9.55	
								CC	0.27	9.55	9.82	
2H	16	0055	9.8	19.3	9.5	9.85	103.0					
								1	0.57	9.80	10.37	
								2	1.07	10.37	11.44	
								3	1.50	11.44	12.94	
								4	1.50	12.94	14.44	
								5	1.50	14.44	15.94	IW 145–150
								6	1.50	15.94	17.44	HS 0–5
								7	1.50	17.44	18.94	
								8	0.50	18.94	19.44	
								CC	0.21	19.44	19.65	
3H	16	0220	19.3	28.8	9.5	9.87	104.0					
								1	1.50	19.30	20.80	
								2	1.50	20.80	22.30	
								3	1.50	22.30	23.80	
								4	1.50	23.80	25.30	IW 145–150
								5	1.50	25.30	26.80	HS 0–5
								6	1.50	26.80	28.30	
								7	0.63	28.30	28.93	
								CC	0.24	28.93	29.17	
4H	16	0340	28.8	38.3	9.5	9.79	103.0					
								1	1.50	28.80	30.30	
								2	1.50	30.30	31.80	
								3	1.50	31.80	33.30	
								4	1.50	33.30	34.80	IW 145–150
								5	1.50	34.80	36.30	HS 0–5
								6	1.50	36.30	37.80	
								7	1.50	37.80	39.30	
								CC	0.23	39.30	39.53	
5H	16	0500	38.3	47.8	9.5	9.97	105.0					
								1	1.50	38.30	39.80	
								2	1.50	39.80	41.30	
								3	1.50	41.30	42.80	
								4	1.50	42.80	44.30	IW 145–150
								5	1.50	44.30	45.80	HS 0–5
								6	1.50	45.80	47.30	
								7	0.67	47.30	47.97	
								CC	0.30	47.97	48.27	
6H	16	0635	47.8	57.3	9.5	9.71	102.0					
								1	1.50	47.80	49.30	
								2	1.50	49.30	50.80	
								3	1.50	50.80	52.30	
								4	1.50	52.30	53.80	IW 145–150
								5	1.50	53.80	55.30	HS 0–5
								6	1.50	55.30	56.80	
								7	0.56	56.80	57.36	
								CC	0.15	57.36	57.51	
7H	16	0800	57.3	66.8	9.5	9.75	102.0					
								1	1.50	57.30	58.80	
								2	1.50	58.80	60.30	
								3	1.50	60.30	61.80	
								4	1.50	61.80	63.30	IW 145–150
								5	1.50	63.30	64.80	HS 0–5
								6	1.50	64.80	66.30	
								7	0.55	66.30	66.85	
								CC	0.20	66.85	67.05	
8H	16	0915	66.8	76.3	9.5	8.55	90.0					
								1	1.50	66.80	68.30	
								2	1.50	68.30	69.80	
								3	1.50	69.80	71.30	
								4	1.50	71.30	72.80	IW 145–150
								5	1.50	72.80	74.30	HS 0–5
								6	1.05	74.30	75.35	
								CC	0.00	75.35	75.35	
9H	16	1030	76.3	85.8	9.5	9.60	101.0					
								1	1.50	76.30	77.80	
								2	1.51	77.80	79.31	
								3	1.50	79.31	80.81	
								4	1.50	80.81	82.31	IW 145–150
								5	1.50	82.31	83.81	HS 0–5
								6	1.50	83.81	85.31	
								7	0.40	85.31	85.71	
								CC	0.20	85.71	85.91	
10H	16	1140	85.8	95.3	9.5	9.28	97.7					
								1	1.50	85.80	87.30	
								2	1.50	87.30	88.80	
								3	1.50	88.80	90.30	
								4	1.50	90.30	91.80	IW 145–150

Table 1 (continued).

Core	Date (August 1994)	Time (UTC)	Sub-bottom (m) Top	Sub-bottom (m) Bottom	Cored (m)	Recovered (m)	Recovery (%)	Section	Length (m)	Depth (mbsf) Top	Depth (mbsf) Bottom	Samples
								5	1.50	91.80	93.30	HS 0–5
								6	1.60	93.30	94.90	
								CC	0.28	94.90	95.18	
11H	16	1305	95.3	104.8	9.5	9.42	99.1					
								1	1.50	95.30	96.80	
								2	1.50	96.80	98.30	
								3	1.50	98.30	99.80	
								4	1.50	99.80	101.30	
								5	1.50	101.30	102.80	HS 0–5
								6	1.50	102.80	104.30	
								7	0.42	104.30	104.72	
								CC	0.00	104.72	104.72	
12H	16	1420	104.8	114.3	9.5	9.60	101.0					
								1	1.50	104.80	106.30	
								2	1.50	106.30	107.80	
								3	1.50	107.80	109.30	
								4	1.50	109.30	110.80	IW 145–150
								5	1.50	110.80	112.30	HS 0–5
								6	1.50	112.30	113.80	
								7	0.60	113.80	114.40	
								CC	0.00	114.40	114.40	
13H	16	1545	114.3	123.8	9.5	9.59	101.0					
								1	1.50	114.30	115.80	
								2	1.50	115.80	117.30	
								3	1.50	117.30	118.80	
								4	1.50	118.80	120.30	
								5	1.50	120.30	121.80	HS 0–5
								6	1.50	121.80	123.30	
								7	0.32	123.30	123.62	
								CC	0.27	123.62	123.89	
14H	16	1715	123.8	133.3	9.5	9.04	95.1					
								1	1.50	123.80	125.30	
								2	1.50	125.30	126.80	
								3	1.50	126.80	128.30	
								4	1.50	128.30	129.80	IW 145–150
								5	1.50	129.80	131.30	HS 0–5
								6	0.66	131.30	131.96	
								CC	0.88	131.96	132.84	
15H	16	1845	133.3	142.8	9.5	9.84	103.0					
								1	1.50	133.30	134.80	
								2	1.50	134.80	136.30	
								3	1.50	136.30	137.80	
								4	1.50	137.80	139.30	
								5	1.50	139.30	140.80	HS 0–5
								6	1.50	140.80	142.30	
								7	0.58	142.30	142.88	
								CC	0.26	142.88	143.14	
16X	16	2020	142.8	149.2	6.4	8.49	132.0					
								1	1.50	142.80	144.30	
								2	1.50	144.30	145.80	
								3	1.50	145.80	147.30	
								4	1.50	147.30	148.80	IW 145–150
								5	1.50	148.80	150.30	HS 0–5
								6	0.50	150.30	150.80	
								CC	0.49	150.80	151.29	
17X	16	2135	149.2	155.6	6.4	6.25	97.6					
								1	1.50	149.20	150.70	
								2	1.50	150.70	152.20	
								3	1.50	152.20	153.70	
								4	1.43	153.70	155.13	HS 0–5
								CC	0.32	155.13	155.45	
18X	16	2310	155.6	165.2	9.6	9.89	103.0					
								1	1.50	155.60	157.10	
								2	1.50	157.10	158.60	
								3	1.50	158.60	160.10	
								4	1.50	160.10	161.60	IW 140–150
								5	1.50	161.60	163.10	HS 0–5
								6	1.50	163.10	164.60	
								7	0.47	164.60	165.07	
								CC	0.42	165.07	165.49	
19X	17	0030	165.2	174.9	9.7	9.92	102.0					
								1	1.50	165.20	166.70	
								2	1.51	166.70	168.21	
								3	1.50	168.21	169.71	
								4	1.50	169.71	171.21	
								5	1.50	171.21	172.71	HS 0–5
								6	1.50	172.71	174.21	
								7	0.47	174.21	174.68	
								CC	0.42	174.68	175.10	
20X	17	0145	174.9	184.5	9.6	9.80	102.0					
								1	1.50	174.90	176.40	
								2	1.50	176.40	177.90	
								3	1.50	177.90	179.40	
								4	1.50	179.40	180.90	IW 140–150
								5	1.50	180.90	182.40	HS 0–5
								6	1.50	182.40	183.90	
								7	0.41	183.90	184.31	
								CC	0.39	184.31	184.70	
21X	17	0315	184.5	194.1	9.6	9.94	103.0					

Table 1 (continued).

Core	Date (August 1994)	Time (UTC)	Sub-bottom (m) Top	Sub-bottom (m) Bottom	Cored (m)	Recovered (m)	Recovery (%)	Section	Length (m)	Depth (mbsf) Top	Depth (mbsf) Bottom	Samples
								1	1.50	184.50	186.00	
								2	1.50	186.00	187.50	
								3	1.50	187.50	189.00	
								4	1.50	189.00	190.50	
								5	1.50	190.50	192.00	HS 0–5
								6	1.50	192.00	193.50	
								7	0.53	193.50	194.03	
								CC	0.41	194.03	194.44	
22X	17	0440	194.1	203.8	9.7	9.91	102.0					
								1	1.50	194.10	195.60	
								2	1.50	195.60	197.10	
								3	1.50	197.10	198.60	
								4	1.50	198.60	200.10	
								5	1.50	200.10	201.60	HS 0–5
								6	1.50	201.60	203.10	
								7	0.53	203.10	203.63	
								CC	0.38	203.63	204.01	
23X	17	0615	203.8	213.4	9.6	9.87	103.0					
								1	1.50	203.80	205.30	
								2	1.50	205.30	206.80	
								3	1.50	206.80	208.30	
								4	1.50	208.30	209.80	IW 140–150
								5	1.50	209.80	211.30	HS 0–5
								6	1.50	211.30	212.80	
								7	0.47	212.80	213.27	
								CC	0.40	213.27	213.67	
24X	17	0740	213.4	223.1	9.7	9.87	102.0					
								1	1.50	213.40	214.90	
								2	1.50	214.90	216.40	
								3	1.50	216.40	217.90	
								4	1.50	217.90	219.40	
								5	1.50	219.40	220.90	HS 0–5
								6	1.50	220.90	222.40	
								7	0.46	222.40	222.86	
								CC	0.41	222.86	223.27	
25X	17	0910	223.1	232.7	9.6	8.09	84.3					
								1	1.50	223.10	224.60	
								2	1.50	224.60	226.10	
								3	1.50	226.10	227.60	
								4	1.50	227.60	229.10	
								5	1.50	229.10	230.60	HS 0–5
								6	0.30	230.60	230.90	
								CC	0.29	230.90	231.19	
26X	17	1035	232.7	242.4	9.7	4.57	47.1					
								1	1.50	232.70	234.20	
								2	1.50	234.20	235.70	
								3	1.14	235.70	236.84	HS 0–5
								CC	0.43	236.84	237.27	
27X	17	1210	242.4	252.0	9.6	7.75	80.7					
								1	1.50	242.40	243.90	
								2	1.50	243.90	245.40	
								3	1.50	245.40	246.90	
								4	1.50	246.90	248.40	IW 140–150
								5	1.50	248.40	249.90	HS 0–5
								CC	0.25	249.90	250.15	
28X	17	1350	252.0	261.6	9.6	4.48	46.6					
								1	1.50	252.00	253.50	
								2	1.50	253.50	255.00	HS 0–5
								3	1.12	255.00	256.12	
								CC	0.36	256.12	256.48	
29X	17	1530	261.6	271.3	9.7	9.89	102.0	1	1.50	261.60	263.10	
								2	1.50	263.10	264.60	
								3	1.50	264.60	266.10	
								4	1.50	266.10	267.60	
								5	1.50	267.60	269.10	HS 0–5
								6	1.50	269.10	270.60	
								7	0.50	270.60	271.10	
								CC	0.39	271.10	271.49	
30X	17	1655	271.3	281.0	9.7	9.90	102.0					
								1	1.50	271.30	272.80	
								2	1.50	272.80	274.30	
								3	1.50	274.30	275.80	
								4	1.50	275.80	277.30	IW 140–150
								5	1.50	277.30	278.80	HS 0–5
								6	1.50	278.80	280.30	
								7	0.49	280.30	280.79	
								CC	0.41	280.79	281.20	
31X	17	1830	281.0	290.6	9.6	9.76	101.0					
								1	1.50	281.00	282.50	
								2	1.50	282.50	284.00	
								3	1.50	284.00	285.50	
								4	1.50	285.50	287.00	Split at 90° to usual plane
								5	1.50	287.00	288.50	HS 0–5
								6	1.50	288.50	290.00	
								7	0.46	290.00	290.46	
								CC	0.30	290.46	290.76	
32X	17	2000	290.6	300.2	9.6	9.89	103.0					
								1	1.50	290.60	292.10	
								2	1.50	292.10	293.60	

Table 1 (continued).

Core	Date (August 1994)	Time (UTC)	Sub-bottom (m) Top	Sub-bottom (m) Bottom	Cored (m)	Recovered (m)	Recovery (%)	Section	Length (m)	Depth (mbsf) Top	Depth (mbsf) Bottom	Samples
								3	1.50	293.60	295.10	
								4	1.50	295.10	296.60	
								5	1.50	296.60	298.10	HS 0–5
								6	1.50	298.10	299.60	
								7	0.51	299.60	300.11	
								CC	0.38	300.11	300.49	
33X	17	2115	300.2	309.9	9.7	9.89	102.0					
								1	1.50	300.20	301.70	
								2	1.50	301.70	303.20	
								3	1.50	303.20	304.70	
								4	1.50	304.70	306.20	IW 140–150
								5	1.50	306.20	307.70	HS 0–5
								6	1.50	307.70	309.20	
								7	0.48	309.20	309.68	
								CC	0.41	309.68	310.09	
34X	17	2235	309.9	319.5	9.6	9.13	95.1					
								1	1.50	309.90	311.40	
								2	1.50	311.40	312.90	
								3	1.50	312.90	314.40	
								4	1.50	314.40	315.90	
								5	1.50	315.90	317.40	HS 0–5
								6	1.16	317.40	318.56	
								CC	0.47	318.56	319.03	
35X	17	2355	319.5	329.2	9.7	9.84	101.0	1	1.50	319.50	321.00	
								2	1.50	321.00	322.50	
								3	1.50	322.50	324.00	
								4	1.50	324.00	325.50	
								5	1.50	325.50	327.00	HS 0–5
								6	1.50	327.00	328.50	
								7	0.45	328.50	328.95	
								CC	0.39	328.95	329.34	
36X	17	0125	329.2	338.9	9.7	9.90	102.0					
								1	1.50	329.20	330.70	
								2	1.50	330.70	332.20	
								3	1.50	332.20	333.70	
								4	1.50	333.70	335.20	IW 140–150
								5	1.50	335.20	336.70	HS 0–5
								6	1.50	336.70	338.20	
								7	0.49	338.20	338.69	
								CC	0.41	338.69	339.10	
37X	17	0250	338.9	348.6	9.7	9.47	97.6					
								1	1.50	338.90	340.40	
								2	1.50	340.40	341.90	
								3	1.50	341.90	343.40	
								4	1.50	343.40	344.90	
								5	1.50	344.90	346.40	HS 0–5
								6	1.50	346.40	347.90	
								CC	0.47	347.90	348.37	
38X	17	0420	348.6	358.2	9.6	8.88	92.5					
								1	1.50	348.60	350.10	
								2	1.50	350.10	351.60	
								3	1.50	351.60	353.10	
								4	1.50	353.10	354.60	
								5	1.50	354.60	356.10	HS 0–5
								6	1.00	356.10	357.10	
								CC	0.38	357.10	357.48	
39X	17	0550	358.2	367.9	9.7	9.47	97.6					
								1	1.50	358.20	359.70	
								2	1.50	359.70	361.20	
								3	1.50	361.20	362.70	
								4	1.50	362.70	364.20	IW 140–150
								5	1.50	364.20	365.70	HS 0–5
								6	1.50	365.70	367.20	
								CC	0.47	367.20	367.67	
40X	17	0725	367.9	377.6	9.7	9.57	98.6					
								1	1.50	367.90	369.40	
								2	1.50	369.40	370.90	
								3	1.50	370.90	372.40	
								4	1.50	372.40	373.90	
								5	1.50	373.90	375.40	HS 0–5
								6	1.50	375.40	376.90	
								7	0.57	376.90	377.47	
								CC	0.00	377.47	377.47	
41X	17	0900	377.6	387.2	9.6	9.90	103.0					
								1	1.50	377.60	379.10	
								2	1.50	379.10	380.60	
								3	1.50	380.60	382.10	
								4	1.50	382.10	383.60	
								5	1.50	383.60	385.10	HS 0–5
								6	1.50	385.10	386.60	
								7	0.52	386.60	387.12	
								CC	0.38	387.12	387.50	
42X	17	1035	387.2	396.9	9.7	8.69	89.6					
								1	1.50	387.20	388.70	
								2	1.50	388.70	390.20	
								3	1.50	390.20	391.70	
								4	1.50	391.70	393.20	IW 140–150
								5	1.50	393.20	394.70	HS 0–5
								6	0.78	394.70	395.48	

Table 1 (continued).

Core	Date (August 1994)	Time (UTC)	Sub-bottom (m) Top	Sub-bottom (m) Bottom	Cored (m)	Recovered (m)	Recovery (%)	Section	Length (m)	Depth (mbsf) Top	Depth (mbsf) Bottom	Samples
								CC	0.41	395.48	395.89	
43X	17	1205	396.9	406.6	9.7	9.92	102.0					
								1	1.50	396.90	398.40	
								2	1.50	398.40	399.90	
								3	1.50	399.90	401.40	
								4	1.50	401.40	402.90	
								5	1.50	402.90	404.40	HS 0–5
								6	1.50	404.40	405.90	
								7	0.50	405.90	406.40	
								CC	0.42	406.40	406.82	
44X	17	1330	406.6	416.2	9.6	9.48	98.7					
								1	1.50	406.60	408.10	
								2	1.50	408.10	409.60	
								3	1.50	409.60	411.10	
								4	1.50	411.10	412.60	HS 0–5
								5	1.50	412.60	414.10	
								6	1.50	414.10	415.60	
								CC	0.48	415.60	416.08	
45X	17	1615	416.2	425.9	9.7	9.09	93.7					
								1	1.50	416.20	417.70	
								2	1.50	417.70	419.20	
								3	1.50	419.20	420.70	
								4	1.50	420.70	422.20	IW 140–150
								5	1.50	422.20	423.70	HS 0–5
								6	1.21	423.70	424.91	
								CC	0.38	424.91	425.29	
Coring totals					425.9	415.18	97.50					

Notes: Hole 952A located at 30°47.449′N, 24°30.574′W. Water depth from sea surface = 5431.8 m.

is a general decrease in $CaCO_3$ content from 40%–60% to <30% at ~200–250 mbsf at all MAP sites. $CaCO_3$ content in the gray turbidites decreases from about 50%–80% to 30% slightly deeper than in the green turbidites (at ~290 mbsf). Calcareous ooze turbidites occur throughout Unit I in all MAP sites but contribute only a minor amount to the overall sedimentary sequence and do not show any significant decrease in $CaCO_3$.

General Stratigraphy

Subunit Ia

Interval: Sections 157-952A-1H-1 through 157-952A-11H-3
Depth: 0–100 mbsf

Subunit Ia at Site 952 consists of medium to very thick beds of green and gray clayey nannofossil mixed sediment and white nannofossil ooze, which represent distal turbidite flows derived from several different source areas (see "Introduction," this volume). Pelagic sediment within Subunit Ia are generally very thin to medium bedded, gray and brown, clayey nannofossil mixed sediment to clay and white nannofossil oozes.

Subunit Ib

Interval: Sections 157-952A-11H-4 through 157-952A-45X-CC
Depth: 100–425 mbsf

The boundary between Subunit Ia and Ib is placed at ~100 mbsf at Site 952, based on the decrease in $CaCO_3$ in the pelagic sediments to <10%. A decrease in $CaCO_3$ also occurs in the turbidite deposits but at a deeper level (225–290 mbsf). Below these depths, the green turbidite deposits, and to a lesser extent the gray turbidites, change from clayey nannofossil mixed sediment to clay, clay with nannofossils, or clay with siliceous microfossils (mainly diatoms and sponge spicules).

Below ~243 mbsf, thin green turbidite beds are the dominant lithology and gray and white turbidites become less common (Fig. 5). These very thin to medium bedded turbidites have sharp basal contacts and upper contacts are either sharp or slightly bioturbated. The oxidized upper part of individual turbidites are pale blue-green with a sharp to gradational change to dark olive green in the lower part of the deposit. Pelagic clays are thin and rare to absent.

Interbedded within Subunit Ib between 380 and 405.5 mbsf are several thick bedded sands, herein referred to as Subunit Ib1 (Fig. 4). Subunit Ib1 consists of green clay rip-up clasts supported in a matrix of poorly sorted sand, silt, and clay (Fig. 7). A typical Subunit Ib1 sequence consists of coarse to medium sand with clay rip-up clasts (ranging in size from coarse sand to pebble) grading upward into structureless silty sand and overlain by thick clays. Basal contacts are sharp (Fig. 8) but do not appear erosional.

Thin section analysis of sand collected at the base of one of the Ib1 units consists of ~30% quartz, 4% feldspar, 10% volcanic rock fragments, 5% vesicular sideromelane fragments (slightly altered volcanic glass), 10% carbonate and bioclastic fragments, 40% clay matrix, and trace amounts of amphibole and glauconite. Quartz grains are dominantly well-rounded and monocrystalline. Polycrystalline quartz and quartzite grains are also common (Fig. 9). Feldspars include slightly altered plagioclase and microcline. Volcanic rock fragments consist of moderately to well rounded basalt, tachylite, and traces of trachyte(?) and pumice. The volcanic glass shards are angular. Carbonate fragments consist of benthic foraminifers, shell fragments, and micrite.

Stratigraphic correlations between Site 952 and Sites 950 and 951 are generally good in the thicker turbidite deposits in the upper part of the sequence. For example, a thick gray turbidite at Site 952, between 189 and 200 mbsf (Fig. 5) is present as a grayish green to gray turbidite at Site 951, between 192 and 199.7 mbsf (Fig. 4, "Site 951" chapter, this volume) and at Site 950, between 190.8 and 198.7 mbsf (Fig. 6, "Site 950" chapter, this volume). Correlation between thinner deposits is more difficult and will require more thorough analysis.

An important change in the microfossil content occurs at ~295 mbsf at Site 952, with a sharp increase in the amount of diatoms and sponge spicules. Conversely, the amount of nannofossils decreases below this depth, corresponding to the decrease in $CaCO_3$ content within the turbidite deposits. An increase in siliceous microfossils and decrease in nannofossils also occurs at about 280 mbsf at Site

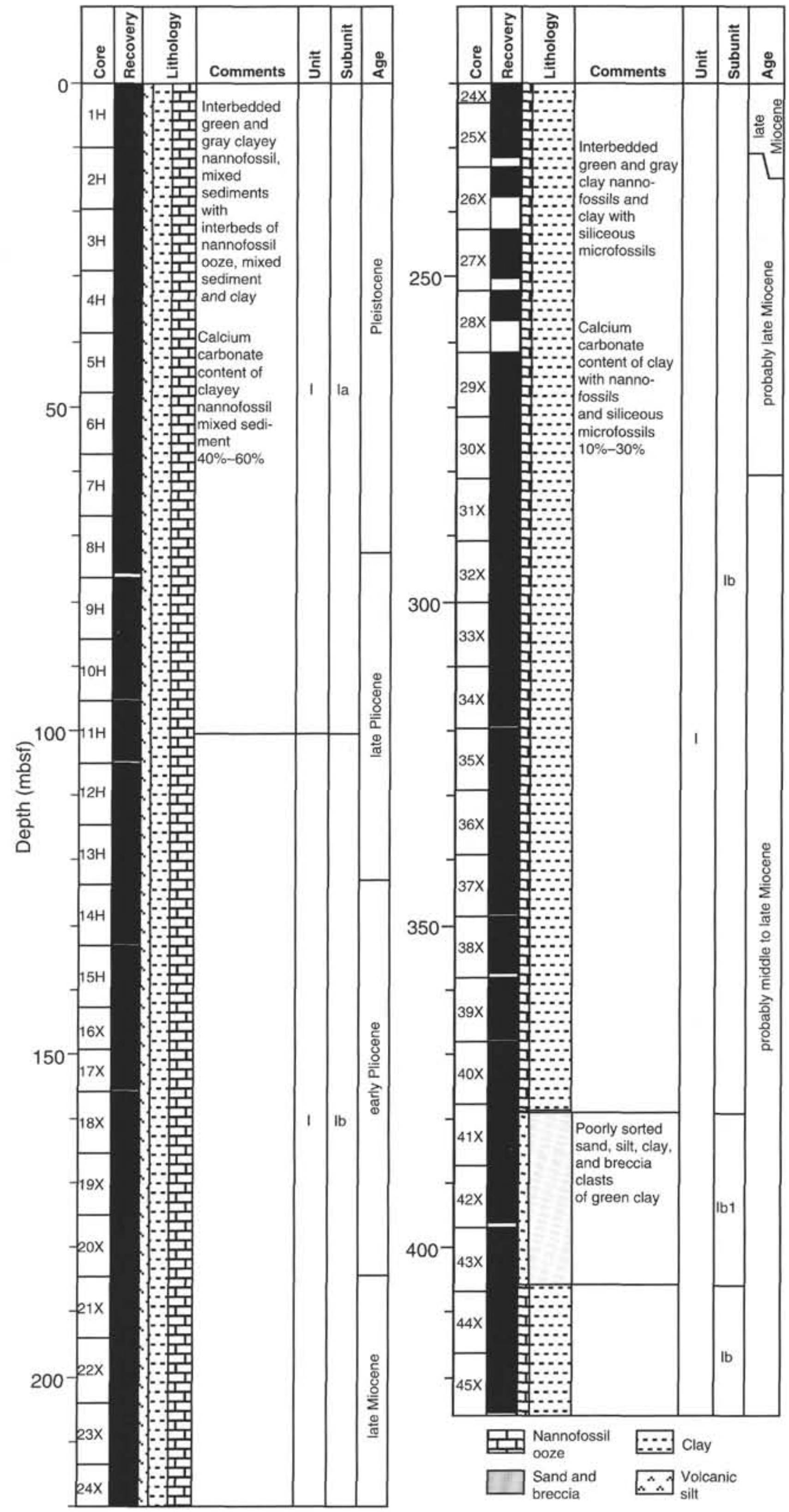

Figure 4. Lithologic summary for Hole 952A, showing the main lithologic units and ages.

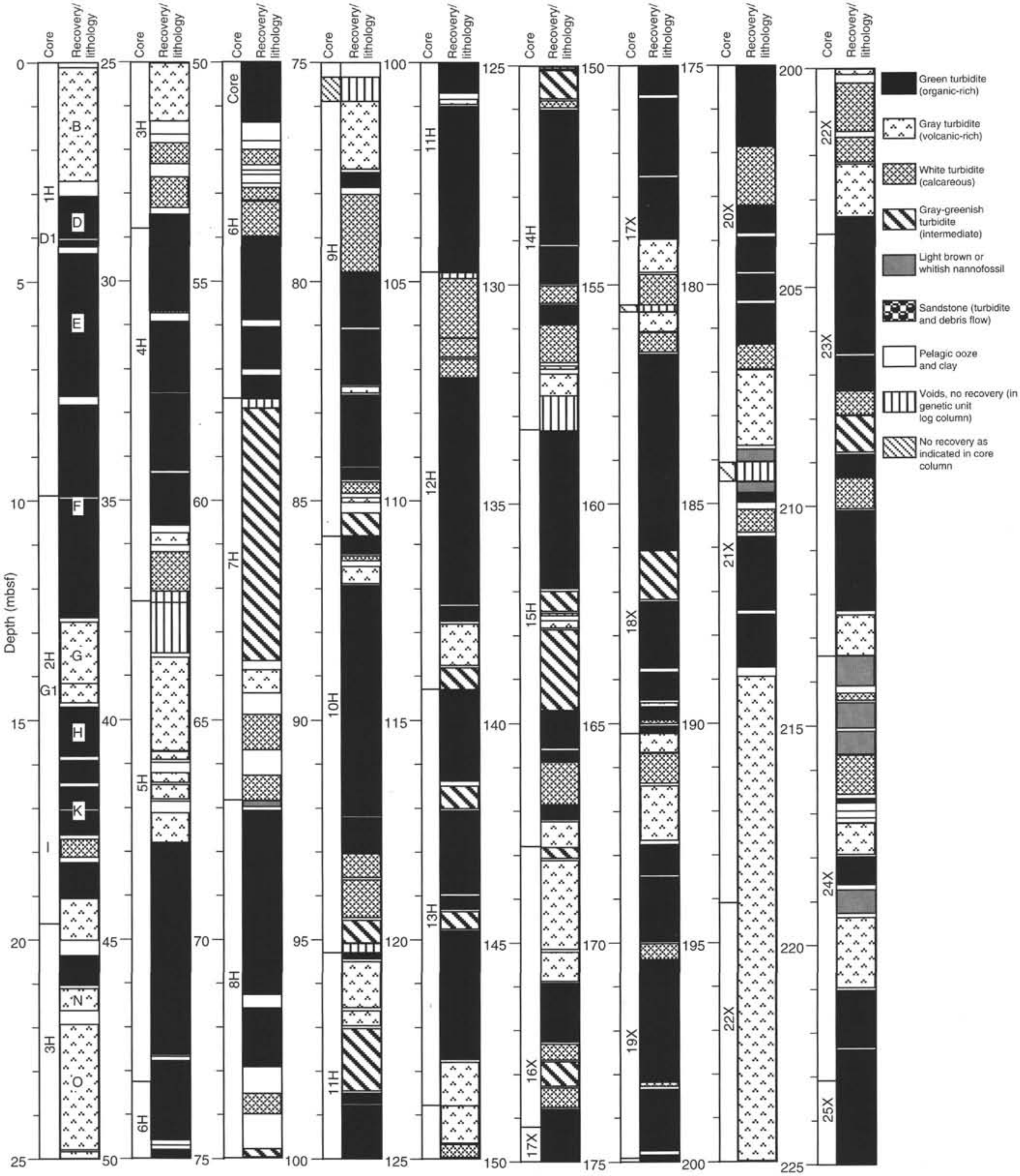

Figure 5. Genetic lithologic log of the sedimentary succession cored at Hole 952A, showing the occurrence and compositional types of turbidite deposits and position of pelagic interbeds.

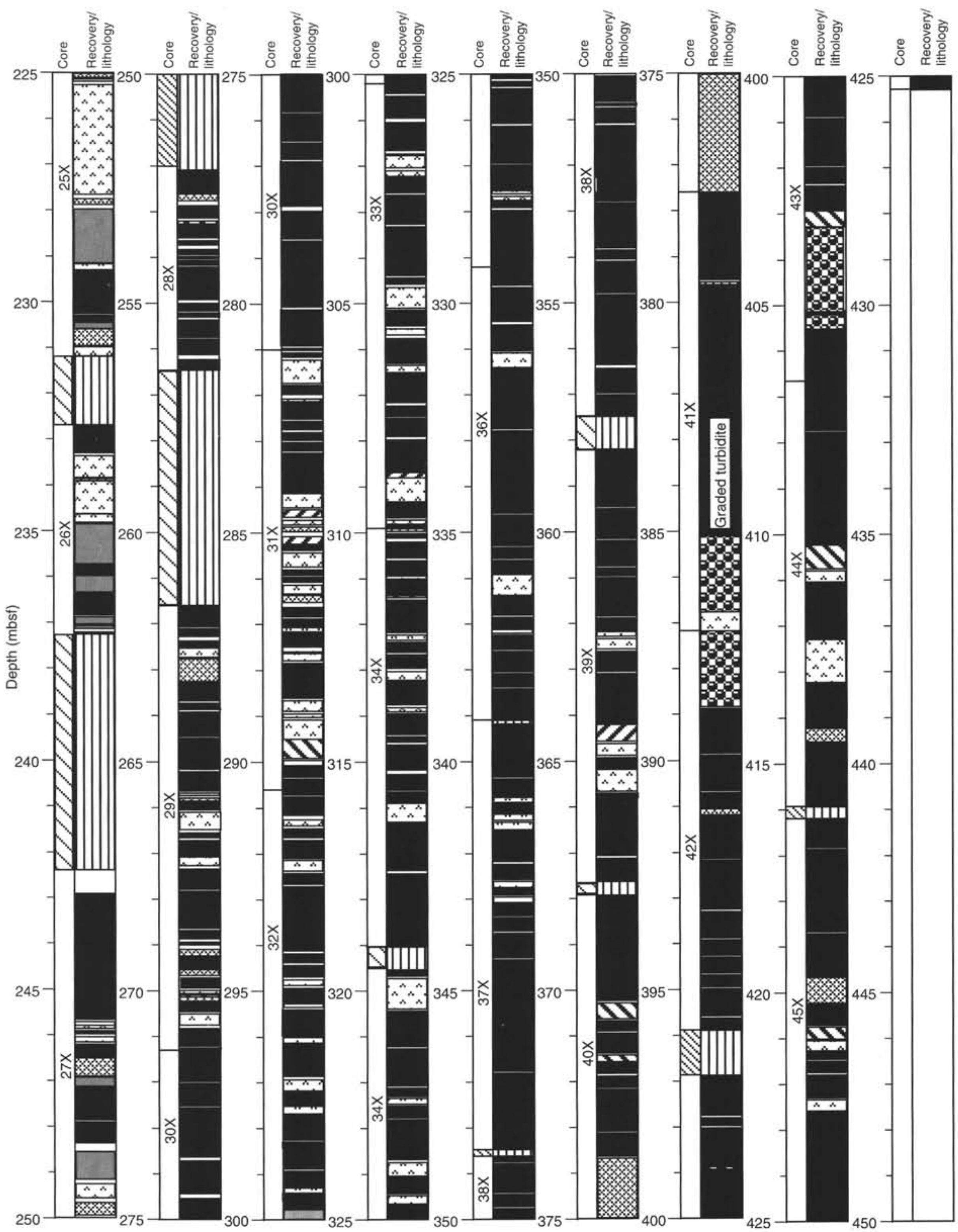

Figure 5 (continued).

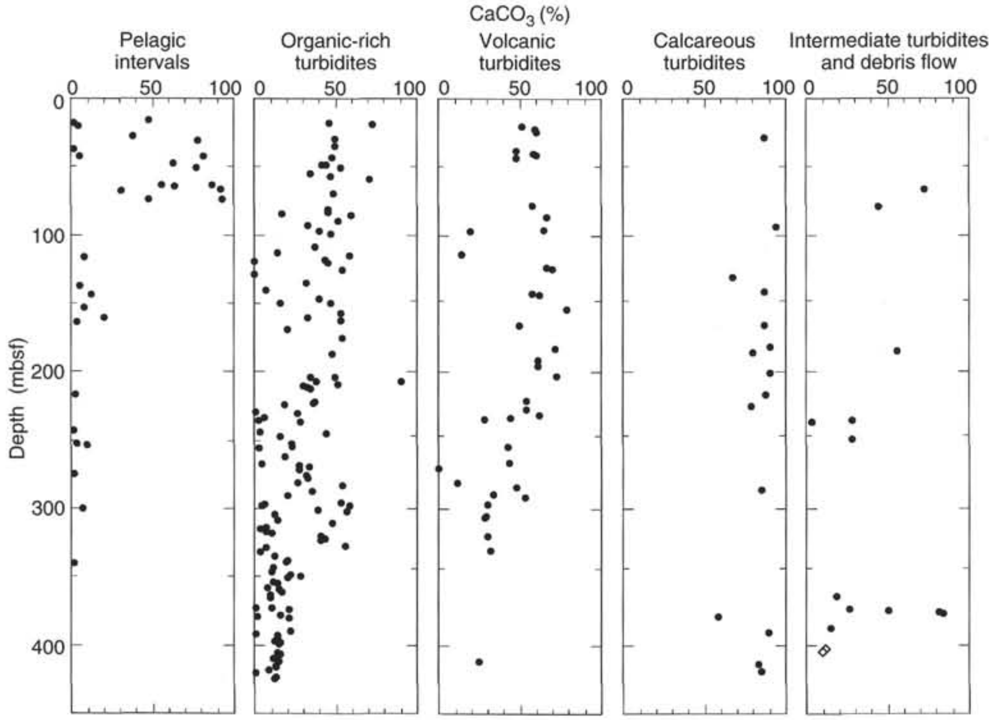

Figure 6. Calcium carbonate content (%) vs. depth below seafloor for the different turbidite types and pelagic sediments in Site 952. In intermediate turbidites and debris flow plot, filled circles = intermediate turbidites and open diamonds = debris flow.

951. Although nannofossils and $CaCO_3$ content decrease within the turbidite units at Site 950 at about 200 mbsf, siliceous microfossils are rare throughout the site.

Depositional History

The deepest sediments cored at Site 952 are lithologically correlative with Subunit Ib at Site 951 and are middle Miocene(?) in age. Subunit Ib at these two sites is lithologically dissimilar to Subunit Ib at Site 950 because of the lack of thin green turbidites and siliceous microfossils.

From at least the middle Miocene to early late Miocene a thick sequence of dominantly green, organic-rich turbidites were deposited at the Site 952. This thick sedimentary sequence consists of thin to medium bedded, distal turbidites derived from the continental margin of northwestern Africa. These turbidite deposits are thickest at Site 952 and thin rapidly to the west and northwest. For example, a distinctive (greenish gray to white) calcareous turbidite occurs at 373.7 to 377.6 mbsf at Site 952 (Fig. 5), at 318.5 to 320 mbsf at Site 951, and possibly at 306 to 307 mbsf at Site 950. The rapid thinning of this sequence to the west and northwest indicates slower sedimentation rates during the middle and late Miocene in the western Madeira Abyssal Plain.

Interbedded within these distal turbidites are several thick and coarse-grained debris flows and turbidites of middle to late Miocene age. Green clay rip-up clasts within the debris flow deposits were derived from erosion of the underlying turbidite deposits, whereas the sand component suggests a mixed continental-volcanic source. Rounded quartz, quartzite, and microcline suggest a contribution from the African craton. Bioclastic and glauconitic grains indicate possible shelf-derived sediment, whereas moderate- to well-rounded basaltic rock fragments indicate an additional volcanic source.

Overlying the thick sequence of thin to medium bedded green turbidites and interbedded debris flow and sandy turbidite sequences is a 100-m-thick sequence (Subunit Ia) of interbedded, medium to very thick bedded green organic-rich, gray volcanic-rich, and white calcareous turbidites. Subunit Ia ranges in age from late Pliocene to Pleistocene. The green turbidites comprise a greater proportion of the sequence, followed by lesser amounts of gray volcanic-rich and white calcareous turbidites. Stratigraphic correlation is good in the thicker turbidite deposits between the three MAP sites drilled during Leg 157, suggesting that from late Miocene to Pleistocene turbidity current transported sediment unimpeded across much of the Madeira Abyssal Plain.

Sediment accumulation from the late Miocene to present has been dominated by periodic influxes of large volumes of material that contribute several decimeters to meters of sediment during each event. The source of the material has varied between the continental margin of Africa, the Canary volcanic islands, and seamounts to the west of the abyssal plain (de Lange et al., 1987; Rothwell et al., 1992; Weaver and Kuijpers, 1983; Weaver and Rothwell, 1987; Weaver et al., 1989, 1992). Between these events sediment accumulated by pelagic deposition in intervals only a few centimeters thick and with lithologies that reflect changes in the depth of the CCD related the glacial/interglacial cycles (Weaver et al., 1989).

BIOSTRATIGRAPHY

Hole 952A penetrated 425.29 m of turbidites with thin interbedded hemipelagic oozes, marls, and clays. These sediments range in age from Pleistocene to probably middle Miocene (Fig. 10) and are essentially similar to those from Sites 950 and 951. The quality of calcareous microfossil biostratigraphy was heavily dependent on the calcium carbonate content of the hemipelagic units. In lithologic Subunit Ia (0 to 100 mbsf), the carbonate content of hemipelagic sediments is high, while in Subunit Ib (100 to 425.29 mbsf) it declines to much lower amounts. The higher carbonate content above 100 mbsf may be related to the onset of Northern Hemisphere glaciation with attendant depression of the CCD at about 2.6 Ma in the late Pliocene. Below this level, only calcareous turbidites have appreciable

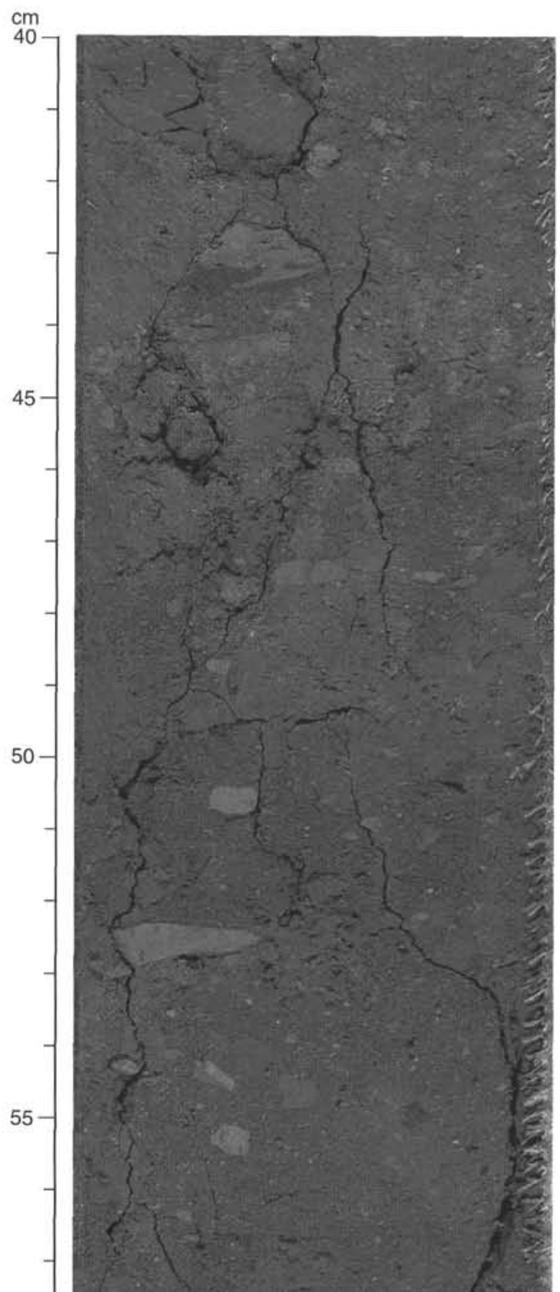

Figure 7. Matrix-supported clay rip-up clasts in a poorly sorted silty sand; Subunit Ib1. Interval 157-952A-41X-6, 40–60 cm.

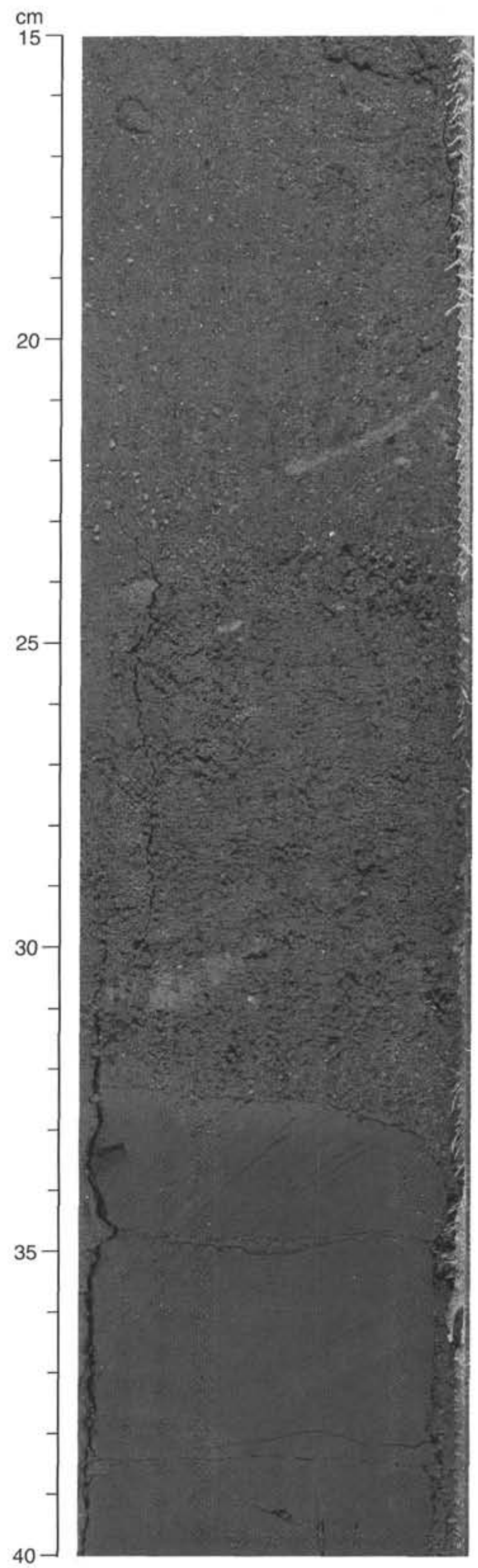

Figure 8. Poorly sorted sand overlying clay of an organic-rich turbidite. Note the sharp basal contact; Subunit Ib1. Interval 157-952A-41X-7, 15–40 cm

amounts of carbonate. Accordingly, mainly hemipelagic sediments were sampled in the upper part of the hole to about 180 mbsf, and mostly turbidites were sampled below this.

The Pliocene/Pleistocene boundary was placed between 72.98 and 74.62 mbsf (Samples 157-952A-8H-5, 18 cm, and 157-952A-8H-6, 32–34 cm) based on both the nannofossil and foraminifer data.

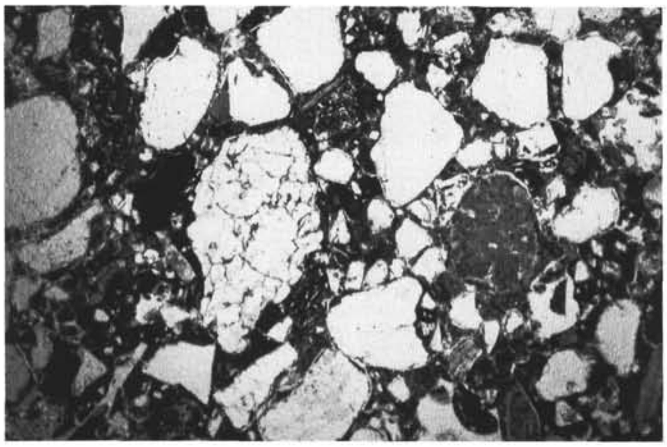

Figure 9. Photomicrograph of sand from Subunit Ib1, Sample 157-952A-42X-1, 149 cm. Note the well-rounded monocrystalline quartz, polycrystalline quartz (quartzite), and glauconite grains. Field of view is 6.0 mm wide.

The Pliocene/Miocene boundary is tentatively placed between 184.33 mbsf and 185.43 mbsf based solely on nannofossil data.

Calcareous Nannofossils

Recovery of autochthonous nannofossils from hemipelagic sediments (Table 2) was relatively good in lithologic Subunit Ia and the upper part of Subunit Ib down to about 125.47 mbsf (Sample 157-952A-14H-2, 17 cm). Specimens were moderately to well preserved, abundant, and they had diverse assemblages in the hemipelagic sediments. Less well preserved assemblages with very low to moderate abundances were recovered from lithologic Subunit Ib down to 179.71 mbsf (Sample 157-952A-20X-4, 31 cm). Between 179.71 and 265.63 mbsf (Sample 157-952A-29X-3, 103 cm) nannofossil recovery was much less consistent, and below 265.63 mbsf most pelagic clays were barren of nannofossils, so turbidites were sampled.

Relatively good, reliable biostratigraphic data can be gained from turbidites only by using FO events as datums. The youngest FO in a turbidite constrains the maximum age of the unit. Unfortunately, in the middle and lower upper Miocene sequence at this site, there are only a few such events, which are widely spaced in time. Some of the marker species for these events are rare or not present (e.g., several species of *Discoaster,* such as *D. hamatus*), some have a variable occurrence (e.g., *Triquetrorhabdulus rugosus*), and others are known to be diachronous in some areas (e.g., *Reticulofenestra pseudoumbilicus*). This has severely reduced the biostratigraphic resolution obtainable in this interval. Shore-based study of the youngest FOs in turbidites from Site 952 should refine the biostratigraphy presented here.

Pleistocene

Pleistocene nannofossils were recovered down to Sample 157-952A-8H-6, 68 cm (74.98 mbsf). The first, Sample 157-952A-1H-6, 16 cm (7.66 mbsf), is below the acme of *E. huxleyi,* indicating an age older than 82 ka. The boundary between Zones CN14 and 15 is tentatively placed between Samples 157-952A-3H-2, 93 cm (21.73 mbsf), and 157-952A-2H-7, 24 cm (17.68 mbsf). It was extremely difficult to determine the lowest occurrence of *E. huxleyi* in the light microscope so the placement of this boundary is tentative. The highest consistent occurrence of *Pseudoemiliania lacunosa* in Sample 157-952A-3H-2, 93 cm (21.73 mbsf), marks the top of Zone CN14a. The lowest occurrence of *Gephyrocapsa oceanica*–like forms defines the base of Zone CN14a in Sample 157-952A-4H-3, 69 cm (32.49

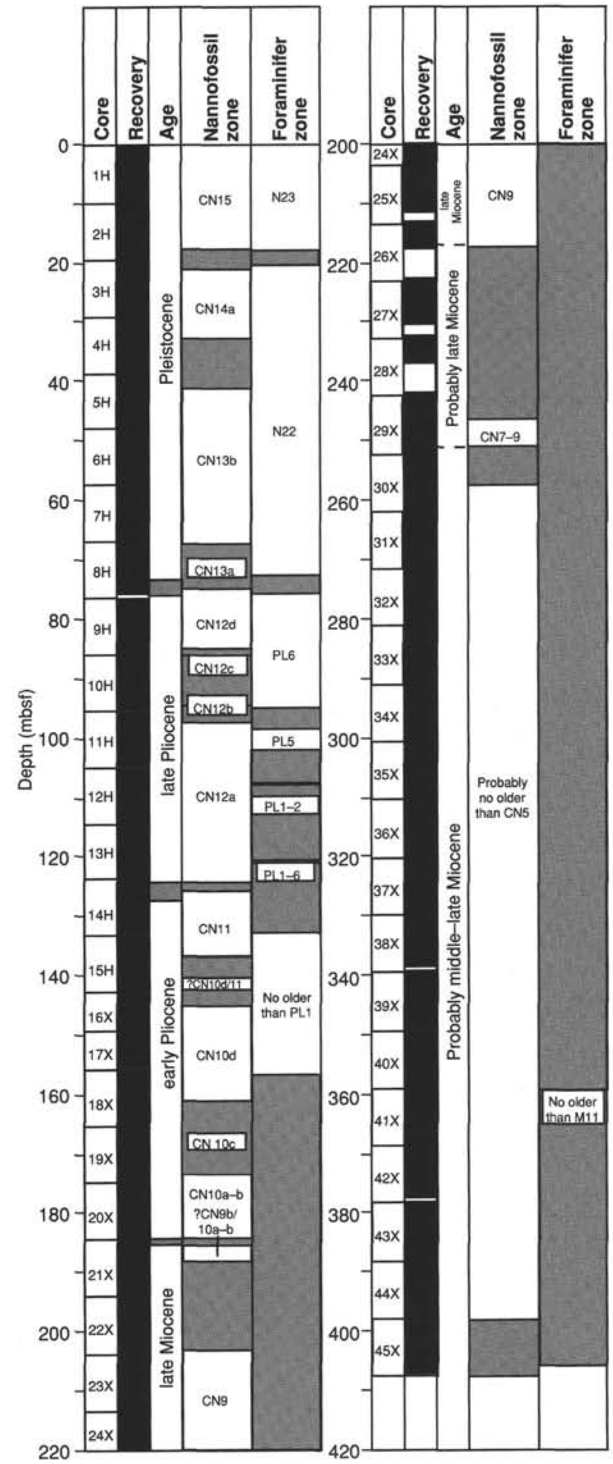

Figure 10. Nannofossil and foraminifer zonations at Hole 952A.

mbsf). The highest occurrence of *Reticulofenestra asanoi,* which occurs in the lower part of Zone CN14a, is also in this sample. The underlying Sample 157-952A-4H-6, 75.5 cm (37.06 mbsf), is barren.

The highest occurrence of the small *Gephyrocapsa* interval (absence of *Gephyrocapsa* spp. larger than 4 µm) was observed in Sample 157-952A-5H-3, 59 cm (41.89 mbsf). *Reticulofenestra asanoi* appears to have a lower occurrence in this hole than at the other two sites. Here it ranges below the base of *Gephyrocapsa oceanica* into

Table 2. Abundance, preservation, and lithology of samples used in nannofossil zonation, Hole 952A.

Core, section, interval (cm)	Depth (mbsf)	Abundance	Preservation	Zone	Lithology
157-952A-					
1H-6, 16–16	7.66	VH	G	CN15	Hemipelagic marl
2H-3, 120–120	12.64	VL	P	CN15	Hemipelagic clay
2H-7, 24–24	17.68	VH	G	CN15	Hemipelagic marl
2H-7, 77–77	18.21	B		Barren	Hemipelagic clay
3H-2, 93–93	21.73	H	G	CN14a	Hemipelagic ooze
3H-5, 111–111	26.41	VH	G	CN14a	Hemipelagic ooze
3H-6, 72–72	27.52	VH	G	CN14a	Hemipelagic marl
4H-2, 48–48	30.78	H	G	CN14a	Hemipelagic ooze
4H-3, 69–69	32.49	VH	G	CN14a	Hemipelagic ooze
4H-6, 75.5–75.5	37.06	B		Barren	Hemipelagic clay
5H-2, 122–122	41.02	H	G	CN13b	Hemipelagic ooze
5H-3, 59–59	41.89	VH	G	CN13b	Hemipelagic ooze
5H-7, 38–38	47.68	H	M	CN13b	Hemipelagic clay
6H-3, 39–39	51.19	VH	G	CN13b	Hemipelagic ooze
6H-6, 43–43	55.73	VH	G	CN13b	Hemipelagic ooze
7H-5, 14–14	63.44	VH	M	CN13b	Hemipelagic ooze
7H-CC, 12–12	66.97	VH	M	CN13b	Hemipelagic marl
8H-5, 18–18	72.98	VH	M	CN13a	Hemipelagic ooze
8H-6, 68–68	74.98	VH	M	CN12d	Hemipelagic ooze
9H-2, 116–116	78.96	VH	M	CN12d	Hemipelagic marl
9H-5, 14.5–14.5	82.45	VL	P	CN12d	Hemipelagic clay
9H-6, 127.5–127.5	85.08	VH	M	CN12d	Hemipelagic marl
10H-1, 108.5–108.5	86.89	L	P	CN12c	Hemipelagic clay
10H-6, 119–119	94.49	H	M	CN12b	Hemipelagic marl
11H-2, 70–70	97.50	VH	M	CN12a	Hemipelagic clay
11H-4, 95–95	100.75	VH	M	CN12a	Hemipelagic marl
12H-6, 50–50	112.80	H	P	CN12a	Hemipelagic clay
13H-2, 58–58	116.38	M	P	CN12a	Hemipelagic clay
13H-6, 89–89	122.69	VH	M	CN12a	Hemipelagic marl
14H-2, 17–17	125.47	VH	M	CN11b	Hemipelagic clay
14H-6, 29–29	131.59	M	M	CN11b	Hemipelagic clay
15H-3, 61–61	136.91	L	P	CN11b	Hemipelagic clay
15H-5, 120–120	140.62	VL	P	CN10d/11	Hemipelagic clay
16X-2, 83–83	145.13	M	P	CN10d	Hemipelagic clay
16X-6, 4–4	150.34	M	M	CN10d	Hemipelagic marl
17X-3, 31–31	152.51	M	G	CN10d	Hemipelagic clay
18X-4, 91–91	161.01	M	G	CN10d	Hemipelagic clay
18X-CC, 6.5–6.5	165.14	B		Barren	Hemipelagic clay
19X-1, 115–115	166.35	M	G	CN10c	Hemipelagic clay
19X-6, 58–58	173.28	L	M	CN10b–a	Hemipelagic clay
20X-3, 92–92	178.82	B		CN10b–a	Hemipelagic clay
20X-4, 31–31	179.71	VH	G	CN10b–a	Hemipelagic ooze
20X-4, 99–99	180.39	B		Barren	Hemipelagic clay
20X-CC, 2–2	184.33	VL	P	CN10b–a	Hemipelagic clay
21X-1, 25.5–25.5	184.76	B		Barren	Hemipelagic clay
21X-1, 49–49	184.99	B		Barren	Brown clay
21X-1, 93–93	185.43	VH	G	CN9b/10a–b	Turbidite
21X-3, 132.5–132.5	188.83	B		Barren	Brown clay
22X-7, 28.5–28.5	203.39	M	M	CN9b	Hemipelagic clay
23X-2, 125.5–125.5	206.56	H	M	CN9	Hemipelagic brown marl
24X-2, 14.5–14.5	215.05	B		Barren	Brown clay
24X-6, 12–12	221.02	B		Barren	Hemipelagic clay
24X-6, 56–56	221.46	B		Barren	Hemipelagic clay
25X-6, 10–10	230.70	VH	G	CN9	Turbidite
26X-1, 113–113	233.83	L	M	CN9	Hemipelagic clay
26X-3, 91–91	236.61	VH	M	CN9	Turbidite
27X-3, 45–45	245.85	B		Barren	Hemipelagic clay
27X-4, 111–111	248.01	B		Barren	Turbidite
28X-2, 8–8	253.58	B		Barren	Hemipelagic clay
28X-3, 47–47	255.47	B		Barren	Turbidite
29X-3, 103–103	265.63	VL	P	CN9 CN7	Hemipelagic clay
29X-6, 110–110	270.20	VH	M	CN9 CN7	Turbidite
29X-6, 124–124	270.34	B		Barren	Hemipelagic
30X-4, 122–122	277.02	H	M	No older than CN5	Turbidite
31X-2, 64–64	283.14	VH	P	No older than CN5	Turbidite
32X-4, 32–32	295.42	VH	P	No older than CN5	Turbidite
33X-CC, 10–10	309.78	VL	M	No older than CN5	Turbidite
34X-5, 6–6	315.96	M	M	No older than CN5	Turbidite
35X-3, 117–117	323.67	B		Barren	Hemipelagic clay
35X-6, 87–87	327.87	VH	G	No older than CN5	Turbidite
36X-6, 48–48	337.18	M	M	No older than CN5	Turbidite
37X-3, 90–90	342.80	H	M	No older than CN5	Turbidite
38X-1, 81–81	349.41	B		Barren	Hemipelagic clay
38X-CC, 22–22	357.32	B		Barren	Turbidite
39X-5, 29.5–29.5	364.50	L	P	No older than CN5	Turbidite
40X-2, 80.5–80.5	370.21	B		Barren	Hemipelagic clay
40X-6, 99–99	376.39	M	P	No older than CN5	Turbidite
42X-3, 89–89	391.09	H	P	No older than CN5	Turbidite
42X-4, 62–62	392.32	M	P	No older than CN5	Turbidite
43X-6, 135–135	405.75	VL	P	No older than CN5	Turbidite
44X-6, 125–125	415.35	L	P	No older than CN5	Turbidite
45X-1, 64.5–64.5	416.85	B		Barren	Hemipelagic clay
45X-6, 17–17	423.87	B		Barren	Turbidite

Note: Key to abbreviations for abundance and preservation in "Explanatory Notes" (this volume).

the upper part of Zone CN13b, down to Sample 157-952A-5H-7, 38 cm (47.68 mbsf). The lowest occurrence of the small *Gephyrocapsa* interval is found in Sample 157-952A-6H-3, 39 cm (51.19 mbsf). The lowest occurrence of *Gephyrocapsa caribbeanica,* marking the base of Zone CN13b, occurs in Sample 157-952A-7H-CC, 12 cm (66.97 mbsf). This event approximates closely the boundary between the Pliocene and Pleistocene, and agrees with the boundary determined by planktonic foraminifers.

Pliocene

Zone CN13a is indicated in Sample 157-952A-8H-5, 18 cm (72.98 mbsf), by the absence of both *Gephyrocapsa caribbeanica* and *Discoaster brouweri.* The highest consistent occurrence of *D. brouweri* is in Sample 157-952A-8H-6, 68 cm (74.98 mbsf), where it occurs with abundant *D. triradiatus* and marks the top of Zone CN12d. The lowest occurrence of abundant *D. triradiatus* occurs in the underlying Sample 157-952A-9H-2, 116 cm (78.96 mbsf), indicating the upper part of Zone CN12d. Sample 157-952A-10H-1, 108.5 cm (86.89 mbsf), contains the highest occurrence of *D. pentaradiatus,* marking the top of Zone CN12c. The underlying Sample 157-952A-10H-6, 119 cm (94.49 mbsf), contains the highest occurrence of *D. surculus,* marking the top of Zone CN12b. The highest occurrence of *D. tamalis,* marking the top of Zone CN12a, occurs immediately below in Sample 157-952A-11H-2, 70 cm (97.50 mbsf).

The highest consistent occurrences of *Reticulofenestra pseudoumbilicus* and *Sphenolithus abies* are in Sample 157-952A-14H-2, 17 cm (125.47 mbsf), marking the top of Zone CN11b. The base of this zone is marked by the lowest occurrence of *Discoaster tamalis* in Sample 157-952A-15H-3, 61 cm (136.91 mbsf). Sample 157-952A-15H-5, 120 cm (140.62 mbsf), has too few nannofossils to be diagnostic and may belong to Zone CN10d or CN11. Sample 157-952A-16X-2, 83 cm (145.13 mbsf), contains the highest occurrence of *Amaurolithus delicatus* and marks the top of Zone CN10d. The base of this zone is marked by the lowest occurrence of common *D. asymmetricus* in Sample 157-952A-18X-4, 91 cm (161.01 mbsf). Sample 157-952A-18X-CC, 6.5 cm (165.14 mbsf), is barren. Zone CN10c occurs in Sample 157-952A-19X-1, 115 cm (166.35 mbsf), based on the lowest occurrence of *Ceratolithus rugosus.* Samples 157-952A-19X-6, 58 cm (173.28 mbsf), to 157-952A-20X-CC, 2 cm (184.33 mbsf), do not contain *C. rugosus* and hence belong to Zones CN10a–b.

Miocene

Sample 157-952A-21X-1, 93 cm (185.43 mbsf), from a turbidite, contains *Discoaster quinqueramus,* the marker for Zone CN9, which was the first indication of the upper Miocene at this site. The presence of *D. surculus* in this sample indicates the upper part of Zone CN9, probably Zone CN9b. As the sample is from a turbidite, with the potential for reworking, it could belong to Zones CN9b or CN10a–b. The highest occurrence of *D. quinqueramus* in a hemipelagic sediment was in Sample 157-592A-22X-7, 28.5 cm (203.39 mbsf). The lowest occurrence of *D. quinqueramus* was in Sample 157-952A-26X-3, 91 cm, which was a turbidite, indicating an age no older than Zone CN9. As this sample is overlain by a sample well constrained to Zone CN9, then it, too, must belong in Zone CN9. Samples 157-952A-27X-3, 45 cm, to -28X-3, 47 cm (245.85–255.47 mbsf), are barren of nannofossils.

Sample 157-952A-29X-3, 103 cm (265.63 mbsf), a hemipelagic clay, contained a poorly preserved nondiagnostic assemblage. The underlying Sample 157-952A-29X-6, 110 cm (270.20 mbsf), contained *D. prepentaradiatus* and a questionable specimen of *D. neohamatus,* suggesting an assignment to Zones CN9 to CN7. Below this level, most hemipelagic sediments and some turbidites are barren of nannofossils. In Samples 157-952A-36X-6, 48 cm (337.18 mbsf), and 157-952A-37X-3, 90 cm (342.80 mbsf), the youngest FO is that of *D. kugleri,* which defines the base of Zone CN5b. Below this level, the youngest FO in the turbidites sampled is that of *Reticulofenestra pseudoumbilicus,* a datum which is known to be diachronous, but which in this area of the Atlantic Ocean occurs near the base of Zone CN5 (Young et al., 1994). This constrains the age of these samples to between Zones CN5 and CN9. Two samples examined from the deepest core, Core 157-952A-45X, are barren.

Planktonic Foraminifers

Planktonic foraminifers are abundant and well preserved (Table 3) in hemipelagic marls and oozes from the surface to Sample 157-952A-8H-6, 32–34 cm (74.62 mbsf), from lithologic Subunit Ia. Below this depth, we sampled pale green turbidites and the sandy bases and ungraded muds of calcareous turbidites because foraminifers were no longer preserved in the hemipelagic intervals. We were able to assign some of these samples to zones, but samples from lithologic Subunit Ib, Samples 157-952A-14H-6, 18–20 cm, to 157-952A-21X-1, 113–115 cm (131.48–185.63 mbsf), contain an impoverished, reworked assemblage of small and size-selected foraminifers, and no age diagnostic taxa were present. We found no other foraminifers suitable for stratigraphic analysis until several sand units were encountered below 370 mbsf.

The Pleistocene is divided into two zones (Table 3 and Figure 10): Zone N23, the base of which is marked in Sample 157-952A-2H-7, 31–33 cm (17.75 mbsf), by the lowest occurrence of *Globigerina calida calida,* and Zone N22, which ranges from the sample immediately below this, Sample 157-952A-3H-2, 98–100 cm (21.78 mbsf), down to the lowest occurrence of *Globorotalia truncatulinoides* in Sample 157-952A-8H-4, 12–14 cm (71.42 mbsf). The Pleistocene assemblage is characterized by repeated occurrences and absences of *Globorotalia menardii* and *Globorotalia tumida,* which Ericson and Wollin (1956 and 1968) and Ericson et al. (1961) used to define their zonation of the tropical to subtropical Atlantic Ocean. *Globorotalia menardii menardii* and *Globorotalia menardii cultrata* are common in Samples 157-952A-2H-7, 31–33 cm, 157-952A-4H-2, 52–54 cm, and 157-952A-4H-3, 75–77 cm. *Pulleniatina obliquiloculata obliquiloculata, Globorotalia inflata,* and *Globorotalia crassaformis* are common to abundant in many samples.

A distinctive succession occurs as the Pliocene/Pleistocene boundary is approached downsection. *Globorotalia truncatulinoides* is absent from Samples 157-952A-7H-5, 15–17 cm, to 157-952A-7H-6, 104–106 cm, but because sinistral *Globorotalia tumida* is present, we assigned this interval (63.45 to 65.84 mbsf) to Zone N22 (following Pujol and Duprat, 1983). We correlate the interval to Ericson and Wollin's (1968) Zone R. *Globorotalia truncatulinoides* recurs in low abundance in Sample 157-952A-7H-CC, 8–10 cm, and is rare in Sample 157-952-8H-4, 12–14 cm, where it makes its lowest appearance in the sequence. The Pliocene/Pleistocene boundary lies between 71.42 and 74.62 mbsf.

The top of the Pliocene lies above Sample 157-952A-8H-6, 32–34 cm (74.62 mbsf), but the base was not defined. PL6 was recognized in four samples (Table 3). The upper part of the zone above the lowest occurrence of *Globorotalia inflata* occurs in Sample 157-952A-8H-6, 32–34 cm. Samples 157-952-9H-2, 114–116 cm, 157-952-10H-1, 45–47 cm, and 157-952-10H-6, 30–32 cm, contain poorly preserved faunas that do not contradict an assignment to Zone PL6 as they do not contain *Globorotalia puncticulata* or *Globorotalia miocenica.* The highest occurrence of the latter defines the base of the zone. Samples 157-952A-11H-2, 68–70 cm (97.48 mbsf), and 157-952A-11H-4, 94–96 cm (100.74 mbsf), are assigned to Zone PL5 based on the presence of *Globorotalia puncticulata* without *Dentoglobigerina altispira,* the highest occurrence of which defines the base of the zone. Sample 157-952A-12H-1, 143–145 cm (106.23 mbsf), from the ungraded mud of a calcareous turbidite was tentatively assigned to Zones PL2–PL1, based on common occurrences of *Globorotalia margaritae, Globorotalia crassaformis,* and *Dentoglo-*

Table 3. Abundance, preservation, and lithology of samples used in foraminifer zonation, Hole 952A.

Core, section, interval (cm)	Depth (mbsf)	Abundance	Preservation	Zone	Lithology
157-952A-					
1H-1, 0–2	0.00	A	G	N23	Hemipelagic ooze mixed with turbidite *a*1
1H-6, 18–20	7.68	C	P	N23	Hemipelagic marl
2H-7, 31–33	17.75	A	M	N23	Hemipelagic marl
3H-2, 98–100	21.78	C	M	N22	Hemipelagic ooze
4H-2, 52–54	30.82	A	G	N22	Hemipelagic ooze
4H-3, 75–77	32.55	A	G	N22	Hemipelagic ooze
5H-2, 133–135	41.13	C	M	N22	Hemipelagic ooze
5H-7, 41–43	47.71	A	M	N22	Hemipelagic ooze
6H-3, 140–142	52.20	A	M	N22	Hemipelagic marl
6H-6, 61–63	55.91	A	G	N22	Green turbidite
7H-5, 15–17	63.45	A	G	N22	Hemipelagic ooze
7H-6, 104–106	65.84	A	G	N22	Hemipelagic ooze
7H-CC, 8–10	66.93	A	G	N22	Hemipelagic marl
8H-4, 12–14	71.42	A	M	N22	Hemipelagic ooze
8H-6, 32–34	74.62	A	M	PL6	Hemipelagic ooze
9H-2, 114–116	78.94	C	P	PL6	Hemipelagic marl
10H-1, 45–47	86.25	C	P	PL6	Calcareous turbidite?
10H-6, 30–32	93.60	F	P	PL6	Hemipelagic marl
11H-2, 68–70	97.48	F	P	PL5	Pale green turbidite
11H-4, 94–96	100.74	F	P	PL5	Hemipelagic marl
12H-1, 143–145	106.23	A	G	PL2 PL1	Sandy base of calcareous turbidite
13H-4, 48–50	119.28	F	P	PL6 PL1	Top of pale green turbidite
14H-6, 18–20	131.48	C	M	No older than PL1	Sandy base of calcareous turbidite
15H-6, 105–107	141.85	A	M	No older than PL1	Ungraded mud of a calcareous turbidite
16X-5, 4–6	148.84	A	G	No older than PL1	Ungraded mud of a calcareous turbidite
17X-4, 135–137	155.05	A	G	No older than PL1	Ungraded mud of a calcareous turbidite
18X-1, 87–89	156.47	A	G	?	Sandy base of calcareous turbidite
18X-1, 89–91	156.49			?	Sandy base of calcareous turbidite
19X-1, 102–104	166.22	A	G	?	Ungraded mud of a calcareous turbidite
20X-5, 107–109	181.97	A	G	?	Sandy base of calcareous turbidite
21X-1, 113–115	185.63	A	M	?	Ungraded mud of a calcareous turbidite
40X-7, 14–16	377.04	F	P	No older than M9	Calcareous sand
42X-1, 122–124	388.42	C	M	?	Sand with few clasts
43X-6, 46–48	404.86	C	P	?	Sand

Note: Key to abbreviations for abundance and preservation in "Explanatory Notes" (this volume).

bigerina altispira. This sample also contains one specimen close to *Globorotalia exilis.* Sample 157-952A-13H-4, 48–50 cm (119.28 mbsf), which was sampled from the top of a pale green turbidite, has few planktonic foraminifers with poorly preserved specimens of *Globigerinoides obliquus* and *Globorotalia crassaformis.* We assign it to a range from Zone PL1 to Zone PL6.

Samples 157-952A-14H-6, 18–20 cm (131.48 mbsf), to 157-952A-21X-1, 113–115 cm (185.63 mbsf), were sampled from the ungraded muds and sandy bases of a sequence of calcareous turbidites (Table 3). They contain strongly reworked assemblages of small, size-sorted foraminifers with no age diagnostic species except sporadic occurrences of *Globorotalia crassaformis.* The samples cannot be assigned to zones but must be no older than Zone PL1, in which *Globorotalia crassaformis* makes its lowest occurrence.

Sample 157-952A-40X-7, 14–16 cm (377.04 mbsf), was taken from a distinctive calcareous sand (Table 3) that was also found at Site 950 (Core 157-950A-34X) and Site 951B (Core 157-951B-7X). It contained few and poorly preserved planktonic foraminifers that can be no older than Zone M11, based on the presence of *Globigerinoides kennetti.* The sample also contained *Globigerina nepenthes, Globigerina woodi, Globigerinoides trilobus,* and *Globorotaloides* cf. *suteri,* the latter ranging into the lower Miocene and may indicate reworking. The turbidite was assigned to a general age of early to middle Miocene at Sites 950 and Zone M9 to M11 at Site 951.

Samples 157-952A-42X-1, 122–124 cm (388.42 mbsf), and 157-952A-43X-6, 46–48 cm (404.86 mbsf), were sampled from thick sands that underlie the distinctive turbidite mentioned above. The sand contains benthic foraminifers including *Amphistegina* and planktonic foraminifers from the latter sample were common but very poorly preserved. Species included *Globorotalia peripheroronda, Globoquadrina venezuelana,* and *Globigerinoides trilobus.* The sands may correspond to those beneath the marker turbidite at Site 950. Sands at both sites bear *Amphistegina* and *Globorotalia peripheroronda,* which range from early to early middle Miocene (top boundary of Zone M7). The specimens may be reworked and their time significance is unclear without further study.

PALEOMAGNETISM

Introduction

Paleomagnetic measurements of the NRM after demagnetization to 25 mT were made on all the APC cores recovered from Hole 952A and analyzed for magnetostratigraphy. The results showed the familiar bias toward normal polarity, but it was not as strong in this core, as at Sites 950 and 951.

The XCB cores, 16X to 31X, were all measured in the long-core mode on the 2G magnetometer after demagnetization to 25 mT. The results show a stronger bias to normal polarity than the APC cores and appear to have acquired a stronger drill component, which was again directed vertically downward. When the XCB cores became so indurated that "biscuiting" was obvious and they had to be cut with the saw rather than split, long-core measurements were terminated. The XCB data have not yet been analyzed for magnetostratigraphy because of the difficulty caused by the drill effects.

Discrete samples from APC and XCB cores were measured. They were compared with the whole-core measurement for quality control. We used primarily the gray turbidites and pelagics, which are the most strongly magnetized material. In addition to standard analysis by Zijderveld plots and Schmidt nets, the NRM, ARM, and IRM characteristics were utilized in an attempt to discriminate reliable primary DRM and PDRM from remagnetized and drilling contaminated magnetizations. A King plot of ARM against k was again used to monitor variations in magnetic phases present in the various lithologies.

Magnetostratigraphy

Plots of declination and inclination, and inclination from pelagic interbeds, with interpreted chron boundaries are shown in Figure 11 and the locations of the various chron boundaries are given in Table 4. The intensity and the susceptibility results from MST measurements are shown in Figure 12. During the analysis of samples from

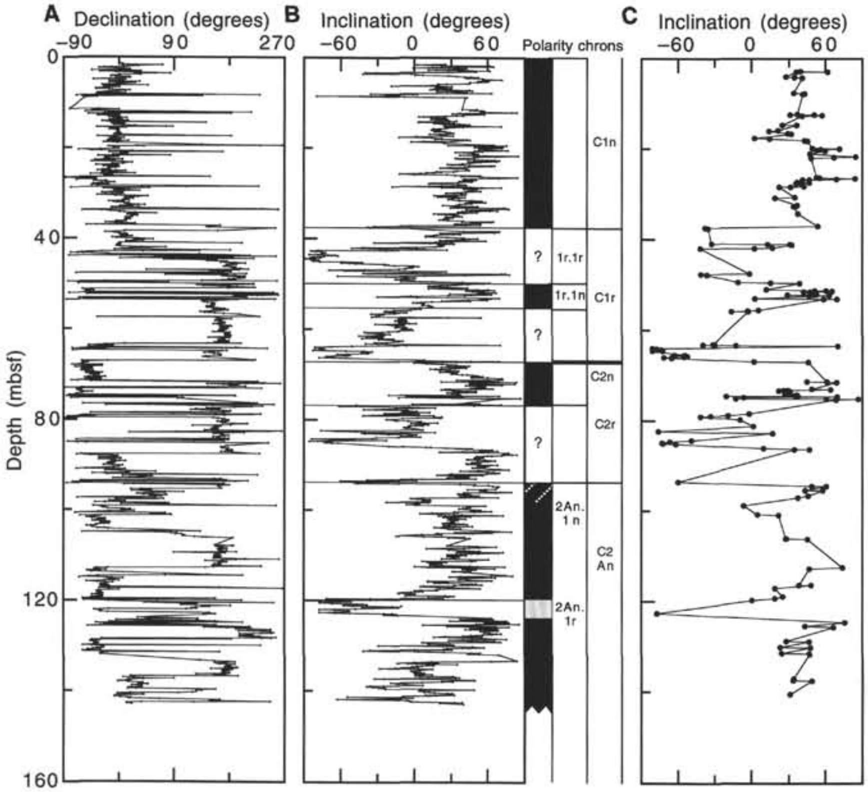

Figure 11. Magnetic data, NRM (25 mT), and interpreted polarity chrons from APC cores, Hole 952A. **A.** Declination. **B.** Inclination from all measurements. **C.** Inclination from measurements of pelagic interbeds. Filled areas = problematic intervals, shaded area = normal chrons, hatched area = probable subchrons.

Table 4. Polarity chrons: ages and correlated core intervals.

Boundary	Name	Age (Ma)	Reference	Depth (mbsf)	Core, Section	Length (cm)
C1n (o)	Brunhes	0.78	SBP90	35–36	4H-6	70–90
C1r.1n (o)	Jaramillo	1.07	SBP90	41–42	5H-2	110
					5H-3	80
C2n (t)	Olduvai	1.77	SBP90	67	8H-1	20
C2n (o)	Olduvai	1.95	SBP90	74.5–77.5	8H-6	100
					9H-2	70
C2An.1n (t)	Gauss	2.60	SBP90,	87–99	10H-1	60
			H91		10H-6	120
C2An.1r (t)	Kaena	3.04	H91	119.8	13H-4	90

Notes: (o) = onset, (t) = top. References as in "Explanatory Notes" (this volume).

this hole, a remarkable correlation between the intensity of NRM in the records from Holes 950A, 951A, and 952A became evident, which reflects the different lithologies in the cores. This correlation revealed a systematic offset of recovered core from Hole 951A with respect to core from Holes 950A and 952A. This offset is caused by a missing interval of 7.5 to 8 m between Cores 157-951A-1H and 157-951A-2H. The correlation of intensity allowed us to resolve an ambiguity in the interpretation of the location of the Brunhes/ Matuyama boundary and of the Jaramillo. The strong correlation of susceptibility maxima with the occurrence of gray (volcanic) turbidites afforded an independent lithological based correlation between the three holes. Nevertheless, we are not entirely confident of this magnetostratigraphy as a result of inadequate signal from the pelagic interbeds at critical points.

The inclination change recording the onset of the Brunhes was observed between 35 and 36 mbsf and is accompanied by a change in declination seen in the tensor tool corrected data. This occurs in Sample 157-952A-4H-6, 70–90 cm, which is a clay interbed. The clay interbed is at the base of a long sequence of green turbidites as at Site 950, and indeed it is at the same depth. As in the previous cores, the last part of the Matuyama is represented by a region of mixed polarities.

The transition to normal inclination at the top of C1r.1n (Jaramillo) is not seen in this record because of very high drilling disturbance at the end of Core 157-952A-4H and the beginning of the next, Core 157-952A-5H. The inclination transition at the bottom of C1r.1n appears in a sequence of pelagic interbeds between the intervals 157-952A-5H-2, 110 cm, and 157-952A-5H-3, 80 cm. These nannofossil oozes are bedded between gray turbidites similar to those at Sites 950 and 951.

The reversed interval from the Jaramillo to the Olduvai is not obscured by the turbidites in this core and is evident in both inclination plots (Fig. 11) and also in the Tensor tool corrected declination. Consequently, there is a sharp transition in inclination at the top of C2n (Olduvai), which is seen in both results from interbedded pelagics only and all sample records. It falls in nannofossil ooze at 67 mbsf in Core 157-952A-8H-1, 20 cm. The base of the Olduvai is defined by a normally magnetized clay at 78.5 mbsf in Core 157-952A-9H-2, 80 cm. The remainder of the Matuyama, C2r, is not clearly seen as a reversed interval in this core and unfortunately there are no significant pelagic interbeds to resolve the polarity interval.

Because of the absence of reliable recorders close to the beginning of the Matuyama, it is hard to locate the end of the Gauss reliably. We have therefore given an interval of between 87 and 94 mbsf for the top boundary of the Gauss. Very few reversed directions are seen over a depth interval of 15 m from 82 mbsf, which we interpret to be the top of C2 An.1, the Gauss normal. A short reversed interval from ~120 to 123 mbsf appears to represent the Kaena. The magnetostratigraphy of the XCB cores has not yet been analyzed and will require further shore-based analyses.

Rock Magnetism

The demagnetization characteristics of NRM, ARM, and IRM, and measurements of weak field susceptibility were conducted as

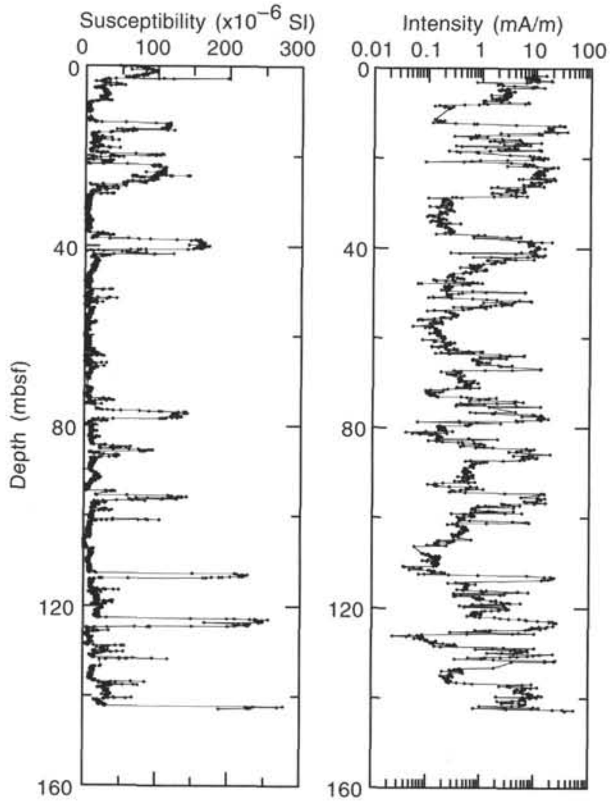

Figure 12. Susceptibility and intensity (NRM, 25 mT) from APC cores, Hole 952A

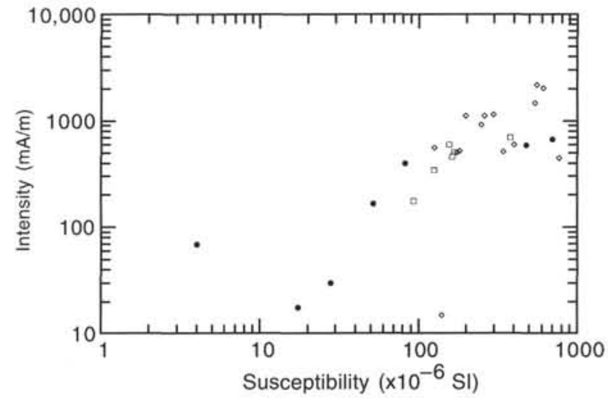

Figure 13. King diagram. 0.1;100 mT ARM vs. weak field susceptibility for turbidites (filled circles), marls (open squares), and clays (open diamonds).

part of the preliminary rock magnetism analyses, the magnitudes of which have also revealed systematic differences between the various lithologies. For example, in Figure 13 the intensity of ARM is plotted against weak field susceptibility (King Diagram) for turbidites, marls, and clays, respectively. While the turbidites have a wide range of susceptibilities, the marls and clays have predominantly stronger susceptibility and ARM, with the clays having the strongest ARM.

Conclusions

A preliminary magnetostratigraphy for the APCs has been generated and is consistent with that from Holes 950A and 951A and the proposed biostratigraphy at each site. By correlating the intensity records between the various cores, magnetostratigraphies obtained from the individual cores were correlated to resolve an ambiguity that otherwise existed in the interpretation of the uppermost sequence of reversals in Hole 952A. However, the magnetostratigraphy is difficult to establish where there are no significant pelagic interbeds, as in the XBC cores. The systematic $+x$ component of the cores measured in the long-core mode appears to be resolved in terms of the radial magnetization in the cores acquired before they are brought aboard ship. At these latitudes the horizontal magnetization does not present a severe problem for recording magnetostratigraphy in the APC cores.

INORGANIC GEOCHEMISTRY

Introduction and Operation

A total of 23 interstitial-water samples were taken at Site 952 from one hole (Hole 952A) between 5.95 and 422.10 mbsf (Table 5). The sampling strategy and analytical methods were identical to those employed at Sites 950 and 951 (see "Explanatory Notes," this volume). Samples were analyzed for pH, salinity, chlorinity, alkalinity, sulfate, ammonia, sodium, potassium, silica, calcium, and magnesium. The bulk mineralogies of pore-water squeeze cakes and some additional samples were determined qualitatively by XRD analysis (Table 6).

As at the other two MAP sites, changes in pore-water composition are driven by the bacterially mediated oxidation of organic matter from organic-rich turbidites, dissolution of biogenic silica, and diagenetic reactions in the siliciclastic fraction, particularly the appearance of smectites and zeolites forming at the expense of volcanic glass.

Chloride and Salinity

Salinity decreases from near-seawater values (34.5–35 g/kg) in the upper 30 m to a minimum of 32 g/kg around 110–170 mbsf. Chloride shows no systematic depletion in this interval. Salinity temporarily increases to 34 g/kg around 170 mbsf, but falls again to 32 g/kg from 150 mbsf to the bottom of the hole.

Chloride fluctuates, but is generally present at levels of around 561–562 mmol/L (slightly above the 559 mmol/L of seawater), in the upper 350 m of sediment, but falls to 548 mmol/L toward the base of the hole. This Cl– minimum may result from the release of chemically bound water at depth from clays.

Sulfate and Alkalinity

The interstitial water SO_4^{2-} profile (Fig. 14) shows progressive depletion from 25.8 mmol/L at 6 mbsf (already significantly less than a typical seawater value of 28.9 mmol/L), to constant low values of around 1 mmol/L between 160 mbsf and the bottom of the hole. This profile, which has a steeper gradient and reaches a lower minimum than those at Sites 950 and 951, demonstrates that rates of sulfate reduction are highest at Site 952. In all three cases, decreasing sulfate in the uppermost beds is matched by increasing ammonia production.

Lithologies and sedimentation rates (3.4 cm/ka) in the upper 200 m are essentially identical at Sites 950–952, so the better developed sulfate profile at Site 952 must be driven by reactions deeper in the sediment column. Despite the presence of residual SO_4^{2-} throughout the sequence, methane, which first appears in significant concentrations below 20 mbsf (see "Organic Geochemistry," this chapter), displays a rapid increase below 160 mbsf, and ethane was identified below 190 mbsf. Clearly, active methanogenesis deeper in the sediment column is providing a diffusional supply of CH_4. The generation of significant methane suggests that the thick sequence of thinly bedded organic-rich turbidites recovered at the base of the hole probably continues some considerable distance below the cored interval.

Alkalinity increases from 5.01 mmol/L at 6 mbsf (significantly higher than the 2.3 mmol/L seawater value), to a maximum of 7

Table 5. Interstitial-water geochemistry, Hole 952A.

Core, section, interval (cm)	Depth (mbsf)	pH	Salinity (g/kg)	Cl (mmol/L)	Alkalinity (mmol/L)	SO_4 (µmol/L)	NH_4 (µmol/L)	Na (mmol/L)	K (mmol/L)	SiO_2 (µmol/L)	Ca (mmol/L)	Mg (mmol/L)	Mg/Ca (molar ratio)
157-952A-													
1H-4, 145–150	5.95	7.60	35.0	561	5.01	26.0	214	456	11.5	499	10.3	52.9	5.13
2H-5, 145–150	15.89	7.48	34.5	563	6.12	23.1	417	487	11.4	488	9.78	51.4	5.25
3H-4, 145–150	25.25	7.62	35.0	567	5.28	21.9	520	480	11.3	435	9.11	51.2	5.61
4H-4, 145–150	34.75	7.71	34.0	569	5.89	19.5	657	508	11.7	781	9.04	52.3	5.79
5H-4, 145–150	44.25	7.40	35.0	566	7.10	17.6	733	488	10.9	671	8.21	48.2	5.87
6H-4, 145–150	53.75	7.37	34.0	561	7.02	15.5	837	472	10.4	507	7.71	47.0	6.09
7H-4, 145–150	63.25	7.31	34.0	561	7.18	14.1	888	475	9.18	433	7.47	45.4	6.08
8H-4, 145–150	72.75	7.37	33.0	560	5.51	12.0	994	485	9.90	512	6.68	42.8	6.41
9H-4, 145–150	82.25	7.60	33.0	563	6.45	10.8	1110	488	11.1	317	6.40	41.5	6.48
10H-4, 145–150	91.75	7.62	33.0	562	5.23	9.04	1150	483	9.19	265	6.31	39.9	6.32
12H-4, 145–150	110.75	7.62	32.0	570	6.25	5.70	1230	473	8.74	287	5.96	34.9	5.85
14H-4, 145–150	129.75	7.53	32.0	562	5.97	3.57	1300	472	9.71	217	6.25	33.8	5.40
16X-4, 145–150	148.75	7.33	32.0	560	5.30	3.54	1230	487	7.94	197	7.00	33.6	4.79
18X-4, 140–150	161.50	7.46	32.0	564	4.90	1.66	1370	476	7.89	304	7.01	30.6	4.36
20X-4, 140–150	180.80	7.70	34.0	563	5.01	1.38	1440	500	7.75	221	7.77	31.8	4.09
23X-4, 140–150	209.70	7.75	33.0	561	4.83	1.12	1470	482	6.51	202	7.89	30.8	3.90
27X-4, 140–150	248.30	7.94	32.0	561	5.04	0.89	1280	472	5.81	234	9.40	31.4	3.34
30X-4, 140–150	277.20	7.77	32.0	561	7.80	1.58	1290	471	6.33	457	11.1	30.6	2.77
33X-4, 140–150	306.10	7.80	32.0	565	10.12	ND	1370	ND	ND	1150	ND	ND	ND
36X-4, 140–150	335.10	6.99	32.0	560	11.24	1.02	967	472	4.88	1190	18.3	28.7	1.56
39X-4, 140–150	364.10	7.77	32.0	559	9.93	1.40	1570	474	5.92	1010	20.7	26.4	1.28
42X-4, 140–150	393.10	ND	ND	550	ND	1.16	1620	477	6.24	846	21.3	23.9	1.13
45X-4, 140–150	422.10	7.98	32.0	548	10.39	1.64	1370	463	4.62	1100	24.5	24.4	1.00

Note: ND = not determined due to insufficient pore water.

mmol/L at 40–65 mbsf (Fig. 14), before declining to a minimum of 5 mmol/L at 160 mbsf (the top of the sulfate minimum). Alkalinity concentrations remain at this level down to 250 mbsf, then increase sharply to >10 mmol/L below 300 mbsf. High alkalinity in the upper beds may be attributed to H_2S and HCO_3^- production accompanying sulfate reduction. As at the other MAP sites, the upper alkalinity maximum occurs above the sulfate and calcium minima and the ammonia maximum, indicating that carbonate precipitation at and below 110 mbsf is consuming alkalinity.

The marked increase in alkalinity in the lower part of the section occurs just above the lithological change to a carbonate-depleted, organic-rich turbidite dominated sequence (see Fig. 6 of "Lithostratigraphy," this chapter) and, as at Site 951, may be caused by enhanced bacterial activity in this interval.

Ammonia

Ammonia increases progressively from 214 to 1470 µmol/L at around 210 mbsf (Fig. 14), and then remains high but variable (967–1570 µmol/L) below. The inverse relationship between sulfate and ammonia displayed in the pore waters at Hole 952A is best developed of all the MAP sites, following a tightly defined nonlinear trend (Fig. 15) that confirms that NH_4^+ is being generated by sulfate reduction of organic matter in the turbidites. Variation in ammonia concentrations below 210 mbsf may be attributed largely to NH_4^+ reactions with clay minerals.

Calcium and Magnesium

Calcium decreases from close to seawater values of 10.3 mmol/L (Fig. 16) at 6 mbsf to a marked minimum of 5.96 mmol/L at 110 mbsf, indicating Ca^{2+} uptake into the solid phase at that level. Below this, concentrations rise again steadily, producing a maximum of 24.5 mmol/L in the bottom sample. The Ca^{2+} minimum coincides with the base of the upper alkalinity peak, which is consistent with carbonate precipitation around 110 mbsf consuming bicarbonate. The lowest samples taken at Hole 952A contain similar concentrations of Ca^{2+} to equivalent depths at Site 951.

Magnesium contents decline consistently in the pore waters at Hole 952A, from near-seawater values of 52.9 mmol/L at 6 mbsf (Fig. 16), to a minimum of 24 mmol/L below 390 mbsf. The profile displays two separate gradients, an upper steep linear decline between the sediment/water interface and 110 mbsf, which is consistent with the diffusional supply of Mg^{2+} from seawater to that depth, and below that, a more gentle linear decline toward the bottom of the section. The Mg/Ca ratio peaks around 80 mbsf, somewhat above the Ca^{2+} minimum and the change in gradient of the Mg^{2+} profile.

As at Sites 950 and 951, it is suggested that sulfate reduction and alkalinity production are promoting calcite precipitation in the upper 80 m, below which dolomite precipitation and calcite dissolution occurs. Dolomite is again a common diagenetic mineral (Table 6), and could be precipitating through much of the sequence. Lower pore-water Mg^{2+} below 150 mbsf and increasing Ca^{2+} concentrations probably result largely from diagenetic reactions within the silicate fraction, principally the formation of smectites (Table 6).

Shifts in the pore-water profiles of the alkali earths again correspond broadly with major changes in the carbonate content of the sediment. The disappearance of high-carbonate pelagic sediments occurs around 100 m (Fig. 6) and a decline in the carbonate content of both organic-rich and volcanic turbidites occurs somewhere around 300 mbsf.

Silica

Silica climbs sharply from relatively high surficial values of 499 µmol/L, to a maximum of 781 µmol/L at 35 mbsf (Fig. 17), before steadily declining to a minimum of 197 µmol/L at 150 mbsf. Between 150 and 240 mbsf silica fluctuates around 200 µmol/L, with a small peak of 304 µmol/L at 160 mbsf. Below 240 mbsf, silica concentrations rise sharply to around 1100 µmol/L at 300 mbsf and in the beds below.

The upper 200 m of the silica profile at Hole 952A show slightly higher concentrations than, but are absolutely identical in morphology to, those recorded at Site 950 (Fig. 32, "Site 950" chapter, this volume). The maximum around 35 mbsf, which occurs within an equivalent package of organic-rich turbidites, is again attributable to the dissolution of biogenic opal in these sediments. The close correspondence between the silica profiles at all three sites is perhaps not unexpected given the similar nature of their stratigraphic records and the overriding control that lithology exerts on silica pore-water profiles in most sequences.

Low concentrations of pore-water silica in the middle of the sequence (130–250 mbsf) are correlated with the occurrence of increased quantities of diagenetic smectites (Table 6). As at Site 951,

Table 6. Mineralogy of Hole 952A sediments determined by XRD analysis.

Core, section, interval (cm)	Depth (mbsf)	Lithology	Mineralogy	
			Dominant minerals	Accessory phases
157-952A-				
1H-4, 145–150	5.95	Green turbidite	Calcite, quartz	Chlorite, dolomite, feldspar, illite, kaolinite, smectite
2H-3, 63–65	12.07*	Green turbidite	Calcite, quartz	Chlorite, dolomite, feldspar, illite, kaolinite, smectite
2H-5, 145–150	15.89	Hemipelagic marl	Calcite, quartz	Dolomite, illite, kaolinite
3H-2, 105–107	21.85*	Hemipelagic ooze	Calcite	Quartz
3H-4, 145–150	25.25	Gray turbidite	Calcite	Feldspar, illite, quartz
4H-7, 20–21	38.00*	Calcareous turbidite	Calcite	Quartz
5H-1, 24–26	38.54*	Hemipelagic clay	Calcite	Illite, philippsite, quartz, smectite
6H-2, 17–19	49.47*	Green turbidite	Quartz, calcite, feldspar	Illite, dolomite, kaolinite
6H-4,145–150	53.75	Calcareous turbidite	Calcite	
7H-3, 83–85	61.13*	Pale green turbidite	Calcite, quartz	Illite, kaolinite
7H-4, 145–150	63.25	Sandy base of green turbidite	Calcite, quartz, feldspar	Illite
8H-3, 69–71	70.49*	Green turbidite	Calcite, quartz	Chlorite, dolomite, illite, kaolinite, phillipsite, smectite
8H-4, 145–150	72.75	Green turbidite	Calcite, quartz	Illite, kaolinite, smectite
9H-1, 97–100	77.27*	Gray turbidite	Calcite	Feldspar, illite, pyroxene, quartz, smectite
9H-4, 145–150	82.25	Green turbidite	Calcite, quartz	Feldspar, illite, kaolinite, smectite
10H-1, 99–100	86.79*	Gray turbidite	Calcite, quartz	Feldspar, illite, kaolinite, smectite
10H-4, 145–150	91.75	Graded base of green turbidite	Calcite, quartz	Chlorite, feldspar, illite, kaolinite, phillipsite, smectite
11H-3, 39–41	98.69*	Dark green turbidite	Quartz, smectite	Illite, kaolinite
12H-4, 145–150	110.75	Green turbidite	Calcite, quartz	Illite, kaolinite, phillipsite, smectite
13H-7, 19–21	123.49*	Gray turbidite	Calcite	Feldspar, illite, kaolinite, phillipsite, quartz, smectite
14H-4, 145–150	129.75	Hemipelagic clay	Calcite, quartz	Feldspar, illite, kaolinite, phillipsite, smectite
14H-6, 28–30	131.58*	Hemipelagic clay	Quartz, calcite	Chlorite, feldspar, illite, kaolinite, phillipsite, smectite
15H-5, 67–69	139.97*	Dark green turbidite	Quartz, calcite, kaolinite	Illite, smectite
16X-1, 20–21	143.00*	Pale green turbidite	Calcite	Chlorite, illite, kaolinite
16X-4, 145–150	148.75	Calcareous turbidite	Calcite	Quartz
18X-1, 35–37	155.95*	Dark gray turbidite	Calcite, quartz, feldspar	Illite, I ill-sm, phillipsite, smectite
18X-4, 140–150	161.50	Gray/green turbidite	Calcite, quartz	Feldspar, illite, phillipsite, smectite
19X-1, 18–20	165.38*	Dark gray turbidite	Calcite, feldspar	Illite, phillipsite, smectite
19X-3, 116–118	169.36*	Dark green turbidite	Calcite, quartz	Illite, I ill-sm, kaolinite, smectite
19X-5, 27–29	171.47*	Pale green turbidite	Calcite	Illite, phillipsite, smectite
20X-2, 79–80	177.19*	Calcareous turbidite	Calcite	Quartz
20X-3, 88–89	178.78*	Green turbidite base	Quartz, feldspar	Dolomite, illite, phillipsite, smectite
20X-4, 140–150	180.80	Pale green turbidite	Quartz	Illite, I ill-sm, kaolinite
21X-4, 51–53	189.51*	Pale gray turbidite	Calcite, quartz	Dolomite, illite, kaolinite, smectite
22X-4, 93–95	199.53*	Gray turbidite	Calcite, quartz	Dolomite, feldspar, illite, kaolinite, smectite
23X-3, 139–141	208.19*	Pale greenish gray turbidite	Calcite, quartz	Illite, smectite
23X-4, 140–150	209.70	Calcareous turbidite	Calcite	Quartz, smectite
24X-3, 43–45	216.83*	Hemipelagic clay	Quartz	Chlorite, feldspar, illite, I ill-sm, kaolinite
25X-4, 86–88	228.46*	Gray/green turbidite	Calcite, quartz	Chlorite, dolomite, illite, phillipsite
26X-1, 53–55	233.23*	Dark green turbidite	Quartz, smectite, kaolinite	
27X-5, 124–126	249.64*	Hemipelagic clay	Quartz	Calcite, illite, I ill-sm, kaolinite, smectite
28X-1, 64–66	252.64*	Calcareous turbidite	Calcite	Quartz, smectite
29X-4, 32–34	266.42*	Gray turbidite	Calcite	Illite, phillipsite, quartz, smectite
30X-4, 140–150	277.20	Pale green turbidite	Calcite, quartz	Chlorite, illite, I ill-sm, kaolinite, smectite
31X-2, 67–69	283.17*	Pale green turbidite	Calcite	Illite, phillipsite, quartz, smectite
32X-1, 69–71	291.29*	Gray turbidite	Calcite	Feldspar, illite, quartz, smectite
33X-4, 140–150	306.10	Pale green turbidite	Calcite	Feldspar, illite, kaolinite, quartz, smectite
33X-7, 2–4	309.22*	Sandy base of green turbidite	Quartz, calcite	Feldspar, smectite
34X-CC, 43–45	318.99*	Dark green turbidite	Calcite, quartz	Dolomite, feldspar, illite, I ill-sm, kaolinite, smectite
35X-3, 39–41	322.89*	Green turbidite	Calcite	Dolomite, illite, kaolinite, quartz, smectite
36X-2, 59–60	331.29*	Gray turbidite	Calcite, feldspar, smectite	I chl-sm, illite, quartz
37X-5, 70–72	345.60*	Green turbidite	Calcite, quartz, smectite, kaolinite	Illite
37X-6, 12–14	346.52*	Graded base of green turbidite	Quartz, calcite	Dolomite, illite, kaolinite, smectite
40X-6, 50–53	375.90*	White to green turbidite	Calcite	Quartz, smectite
40X-7, 49–51	377.39*	Sandy base of white to green turbidite	Calcite	Clinoptilolite, feldspar, phillipsite, quartz
41X-7, 19–21	386.79*	Sandy base of green turbidite with mud clasts	Quartz, feldspar, smectite	Smectite
42X-1, 144–146	388.64*	Sand with mud clasts	Quartz	Calcite, feldspar, smectite
44X-1, 114–116	407.74*	Green turbidite	Quartz, calcite	Smectite

Notes: All samples are pore-water squeeze-cakes except those marked by an asterisk, which are additional material. I ill-sm = interstratified illite-smectite; I chl-sm = interstratified chlorite-smectite.

high values of dissolved silica (up to 1190 µmol/L) below 300 mbsf are associated with the renewed occurrence of biogenic silica (diatoms) in the section, as well as high smectite contents.

Potassium

Pore-water potassium concentrations (Fig. 17) decline from slightly higher (11 mmol/L) than seawater values, to 4.62 mmol/L in the deepest sample. Potassium uptake may be due to the precipitation of phillipsite in the deeper parts of the sequence.

ORGANIC GEOCHEMISTRY

The shipboard organic geochemistry program at Site 952 followed the same procedures used for Sites 950 and 951.

Volatile Hydrocarbons

Concentrations of methane (C_1) and ethane (C_2) gases were monitored in every core using the standard ODP headspace-sampling technique as part of the SSP program. As distinct from the two previous sites, methane concentrations increased downward from the third core (Fig. 18), reaching a maximum value of 33,900 ppmv at 393 mbsf. Beginning at a methane level of 929 ppm at 191 mbsf, ethane was detected in all samples down to the bottom of the hole (Table 7). A continuously increasing trend indicates that higher methane concentrations may be found at deeper levels. Ethane increased from 0.4 to 30 ppmv at the base of the sequence. The C_1/C_2 ratio varied from 2320 at 191 mbsf to 1030 at the bottom of Hole 952A (Fig. 19).

Safety considerations especially focus on the appearance of ethane and other higher hydrocarbons during core recovery as an in-

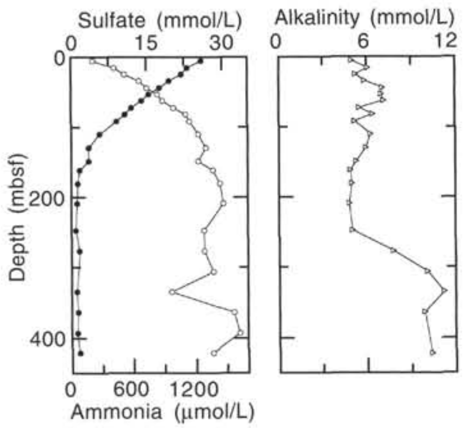

Figure 14. Interstitial-water sulfate (filled circles), ammonia (open circles), and alkalinity, Hole 952A.

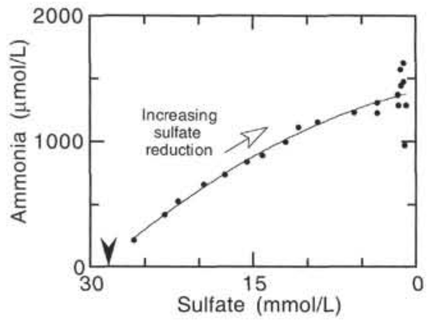

Figure 15. Inverse relationship between interstitial-water ammonia and sulfate, Hole 952A (filled arrow head points to seawater value).

dicator that the underlying sediments could contain gas or oil deposits that would be hazardous for the *JOIDES Resolution* to encounter. If methane reaches high values, ethane and C_{3+} hydrocarbon contents become important. The C_1/C_2 ratio (Fig. 19) did not reach hazardous levels at Site 952, relatively shallow depth to basement should preclude the occurrence of hydrocarbons at deeper levels. However, the overall geochemistry points to an undisturbed, pristine, and immature sedimentary environment, which is evidence against significant biogenic methane formation in situ. The steady increase of C_1 and C_2 with depth indicates that part of the gas originates from below the drilled section.

Carbon, Nitrogen, and Sulfur Concentrations

XResults for determinations of organic carbon, total carbon, total nitrogen, and total sulfur are presented in Figure 20 and Table 8. All told, 247 carbonate analyses were made at Site 952 and form the basis of a more detailed stratigraphy, as at Sites 950 and 951. The calcium carbonate content of the organic turbidites (Fig. 6) shows a decrease in the lower parts of the hole as it does for the volcanic turbidites. Analyses of organic carbon, nitrogen, and sulfur show very good correlation for the organic turbidites (Table 8), especially in the lower part of the hole. Organic carbon varied between 0.57% and 1.97%, with nitrogen between 0.02% and 0.16%, and sulfur from 0.60% to 3.95%.

C/N values were generally low (8–12) in the upper part of the hole (Fig. 21), but increased at the bottom of the sequence to 10–20. A marine source is indicated for the organic matter at Site 952, but samples with lower levels may have admixtures of terrigenous material. Occasional low values of C/N probably indicate the presence of nitrogen in clay minerals.

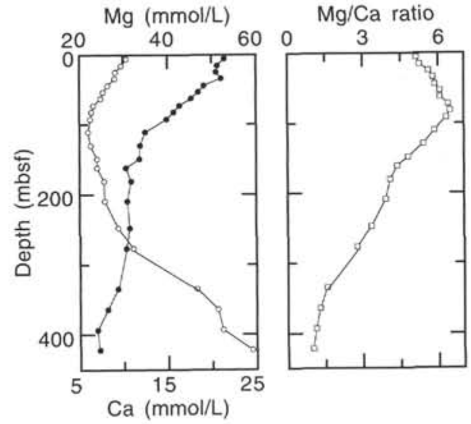

Figure 16. Interstitial-water magnesium (filled circles), calcium (open circles), and Mg/Ca ratio, Hole 952A.

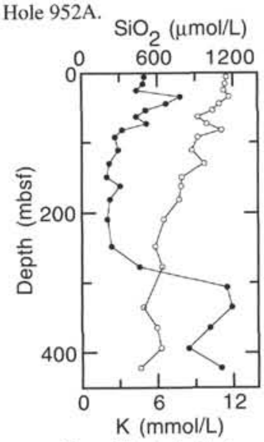

Figure 17. Interstitial-water silica (filled circles) and potassium (open circles), Hole 952A.

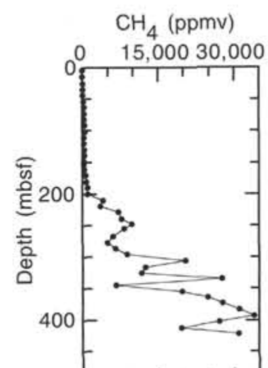

Figure 18. Methane concentrations in headspace samples, Hole 952A.

PHYSICAL PROPERTIES

Introduction

The shipboard physical properties measurements program at Site 952 included nondestructive measurements of bulk density, bulk

Table 7. Methane and ethane concentrations (ppmv) in headspace samples, Hole 952A.

Core, section, interval (cm)	Depth (mbsf)	C_1	$C_{2=}$	C_2	C_1/C_2
157-952A-					
1H-4, 0–5	4.50	5			
2H-5, 0–5	14.44	7			
3H-5, 0–5	25.30	91			
4H-5, 0–5	34.80	105			
5H-5, 0–5	44.30	122			
6H-5, 0–5	53.80	257			
7H-5, 0–5	63.30	280			
8H-5, 0–5	72.80	289			
9H-5, 0–5	82.30	327			
10H-5, 0–5	91.80	405			
11H-5, 0–5	101.30	399			
12H-5, 0–5	110.80	247			
13H-5, 0–5	120.30	204			
14H-5, 0–5	129.80	287			
15H-5, 5–5	139.30	303			
16X-5, 0–5	148.80	233			
17X-4, 0–5	153.70	133			
18X-5, 0–5	161.60	314			
19X-5, 0–5	171.20	557			
20X-5, 0–5	180.90	686			
21X-5, 0–5	190.50	929		0.4	2320
22X-5, 0–5	200.10	1,000		0.6	1670
23X-5, 0–5	209.80	4,000		0.7	5710
24X-5, 0–5	219.40	3,510		0.7	5010
25X-5, 0–5	229.10	7,040		1	5410
26X-3, 0–5	235.70	7,750		1	5540
27X-5, 0–5	248.40	9,710	0.3	3	2940
28X-3, 0–5	255.00	8,280		2	4140
29X-5, 0–5	267.60	6,140		2	3610
30X-5, 0–5	277.30	4,910		1	4460
31X-5, 0–5	287.00	6,490		3	2400
32X-5, 0–5	296.60	8,790		4	2040
33X-5, 0–5	306.20	20,290		7	2940
34X-5, 0–5	315.90	12,470		6	2110
35X-5, 0–5	325.50	11,630		5	2590
36X-5, 0–5	335.20	27,560	0.2	13	2090
37X-5, 0–5	344.90	66,000		5	1320
38X-5, 0–5	354.60	19,700	0.3	12	1640
39X-5, 0–5	364.20	24,700	0.2	12	2060
40X-5, 0–5	373.90	27,800	0.2	19	1460
41X-5, 0–5	383.60	31,040	0.1	19	1630
42X-5, 0–5	393.20	33,900	0.3	24	1410
43X-5, 0–5	402.90	27,070		17	1590
44X-5, 0–5	412.60	19,560		12	1630
45X-5, 0–5	422.20	30,930		30	1030

magnetic susceptibility, and *P*-wave velocity on whole sections of core using the MST as well as point measurements of compressional-wave velocity parallel to the core axis, shear strength, and index properties. Sample locations for the point measurements were selected from the least disturbed sections of the working half of the core.

Whole-core Measurements

MST

Whole-round measurements of GRAPE density and magnetic susceptibility were made on all cores from Hole 952A. *P*-wave velocity measurements were made on cores down to ~143 mbsf. Figures 22, 23, and 24 show data from the GRAPE density, *P*-wave velocity, and magnetic susceptibility sensors, respectively. The data are filtered by a running median of 12.5 cm intervals to eliminate spikes in the curves. Intervals longer than the filter length without data are indicated by gaps in the curves. For comparison, each of the MST data sets is plotted at a common scale in Figures 25 through 29 for ranges 0–100, 100–200, 200–300, 300–400, and 400–423 total depth mbsf, respectively. The three individual curves show significant correlation, suggesting that the consistent log response might be used for lithologic discrimination. For example, the distinctive positive spikes seen in the magnetic susceptibility data (Figs. 25 through 29), occur at the same level as distinctive decreases in the velocity. This response can be correlated with the volcanic gray turbidites observed throughout the core (see "Paleomagnetism" and "Lithostratigraphy," this chapter).

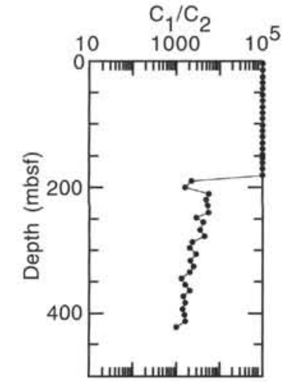

Figure 19. Methane/ethane (C_1/C_2) ratios in headspace samples, Hole 952A.

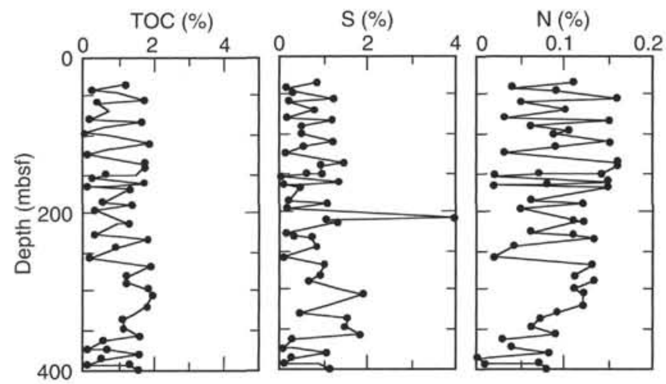

Figure 20. Concentration profiles of total organic carbon, total sulfur, and total nitrogen in Hole 952A.

Split-core Measurements

Measurements made on the split core include the index properties (wet-bulk density, wet-water content, porosity, grain density; Fig. 30), longitudinal-wave velocity (Fig. 31), and shear strength (Fig. 32). An average of approximately one sample per section was collected, though samples were sometimes concentrated to examine vertical variation in properties through a particular turbidite unit. When possible, sampling was coordinated to a common depth, resulting in determinations of all properties for a number of positions in the core. Core recovery in this hole was good, resulting in a continuous set of physical properties measurements.

Index Properties

Index properties were determined from discrete samples by gravimetric methods in each core throughout Hole 952A. Calculations of index properties have been made following Methods B and C (see "Explanatory Notes," this volume). Although some variation in the values calculated by the different methods clearly exists, this difference is particularly noticeable with grain density (see "Site 950," this volume). Method B was chosen for determination of the bulk density (Figure 30A) and Method C was utilized for the remainder of the determinations.

Table 8. Elemental and organic carbon compositions of sediments, Site 952.

Core, section, interval (cm)	Depth (mbsf)	Sediment type	Inorganic carbon (%)	$CaCO_3$ (%)	Total carbon (%)	TOC (%)	Total nitrogen (%)	Total sulfur (%)	C/N (ratio)
157-952A-									
4H-5, 31–32	35.11	O	5.93	49.4	7.11	1.18	0.11	0.81	10.7
5H-2, 34–35	40.14	V	7.00	58.3	7.21	0.21	0.04	0.13	5.3
5H-4, 52–53	43.32	O	5.69	47.4	6.60	0.91	0.09	0.28	10.1
6H-5, 116–117	54.96	O	4.16	34.7	5.88	1.72	0.16	1.16	10.8
7H-2, 37–38	59.17	O	8.48	70.6	8.87	0.39	0.05	0.17	7.8
8H-2, 105–106	69.35	O	5.84	48.6	6.52	0.68	0.10	0.73	6.8
9H-1, 136–137	77.66	V	6.85	57.1	6.99	0.14	0.03	0.13	4.7
9H-4, 74–75	81.54	O	5.42	45.1	7.02	1.60	0.15	1.16	10.7
10H-3, 94–95	89.74	O	6.17	51.4	6.75	0.58	0.06	0.50	9.7
11H-1, 89–90	96.19	V	7.69	64.1	7.78	0.04	0.10	BD	0.4
11H-3, 117–118	99.47	O	5.62	46.8	6.38	0.76	0.09	0.48	8.4
12H-3, 70–71	108.50	O	4.46	37.2	6.31	1.85	0.15	1.21	12.3
13H-3, 47–48	117.77	O	5.17	43.1	5.91	0.74	0.09	0.52	8.2
14H-1, 62–63	124.42	V	8.35	69.6	8.48	0.13	0.03	0.12	4.3
15H-2, 83–84	135.63	O	3.77	31.4	5.45	1.68	0.16	1.44	10.5
15H-5, 85–86	140.15	O	0.88	7.30	2.55	1.67	0.16	0.92	10.4
16X-5, 104–105	149.84	O	1.86	15.5	3.35	1.49	0.14	0.93	10.6
17X-1, 86–87	150.06	O	5.61	46.7	6.26	0.65	0.07	0.60	9.3
17X-4, 54–55	154.24	V	9.42	78.5	9.68	0.26	0.02	BD	13.0
18X-4, 48–49	160.58	O	3.95	32.9	5.65	1.70	0.15	1.33	11.3
18X-5, 128–129	162.88	O	6.38	53.1	7.05	0.67	0.08	0.43	8.4
19X-1, 22–23	165.42	V	5.88	49.0	6.01	0.13	0.02	0.11	6.5
19X-3, 72–73	168.92	O	2.39	19.9	3.74	1.35	0.15	0.44	9.0
21X-1, 16–17	184.66	I	6.68	55.6	7.23	0.55	0.06	0.19	9.2
21X-2, 95–96	186.95	O	5.71	47.6	7.06	1.35	0.12	1.06	11.3
22X-1, 90–91	195.00	V	7.32	61.0	7.67	0.35	0.05	0.18	7.0
23X-5, 70–71	210.50	O	3.59	29.9	4.84	1.25	0.12	3.95	10.4
23X-6, 29–30	211.59	O	3.92	32.7	5.06	1.14	0.11	1.11	10.4
23X-6, 60–61	211.90	O	4.11	34.2	5.05	0.94	0.11	1.26	8.5
25X-3, 64–65	226.74	V	6.43	53.6	6.79	0.36	0.06	0.15	6.0
25X-5, 40–41	229.50	O	0.08	0.7	1.23	1.15	0.11	0.33	10.5
26X-1, 51–52	233.21	O	0.75	6.2	2.50	1.75	0.13	0.68	13.5
27X-2, 5–7	243.95	O	0.41	3.4	1.31	0.90	0.04	0.82	22.5
28X-3, 54–55	255.54	O*	0.33	2.7	0.48	0.15	0.02	0.06	7.5
29X-5, 69–70	268.29	O	3.31	27.6.	5.18	1.87	0.13	0.98	14.4
30X-7, 29–30	280.59	O	3.16	26.3	4.40	1.24	0.11	0.84	11.3
31X-5, 37–38	287.37	O	4.24	35.3	5.45	1.21	0.13	0.71	9.3
32X-4, 126–127	296.36	O	0.78	6.5	2.60	1.82	0.11	1.29	16.5
33X-3, 74–75	303.94	O	1.49	12.4	3.39	1.90	0.12	1.86	15.8
34X-5, 117–118	317.07	O	0.88	7.3	2.65	1.77	0.12	1.09	14.8
35X-7, 31–32	328.81	O	0.85	7.1	2.23	1.38	0.09	0.44	15.3
36X-4, 86–87	334.56	O	1.49	12.4	2.54	1.05	0.07	1.52	15.0
37X-5, 124–125	346.14	O	1.30	10.8	2.45	1.15	0.06	1.48	19.2
38X-5, 76–77	355.36	O	1.64	13.7	3.18	1.54	0.09	1.78	17.1
39X-2, 132–133	361.02	O	1.99	16.6	2.56	0.57	0.03	0.26	19.0
40X-4, 80–81	373.20	O*	0.10	0.8	0.19	0.09	BD	0.08	ND
40X-4, 104–105	373.44	O	1.29	10.7	1.95	0.66	0.04	0.24	16.5
41X-3, 30–31	380.90	O	2.57	21.4	4.10	1.53	0.08	1.05	19.1
42X-1, 74–75	387.94	V	1.80	15.0	2.27	0.47	BD	0.24	ND
42X-4, 70–71	392.40	O*	0.09	0.7	0.19	0.10	0.01	0.05	10.0
42X-4, 112–113	392.82	O	1.64	13.7	2.98	1.34	0.07	0.85	19.1
43X-3, 5–6	399.95	O	1.81	15.1	3.33	1.52	0.08	1.11	19.0
43X-5, 60–61	403.50	D	1.50	12.5	1.75	0.25	BD	0.13	ND
43X-6, 94–95	405.34	D	1.26	10.5	1.31	0.05	BD	0.25	ND
44X-1, 78–79	407.38	O	1.93	16.1	3.48	1.55	0.04	0.39	38.8
44X-4, 92–93	412.02	O	1.83	15.2	3.71	1.88	0.10	1.49	18.8
44X-5, 7–8	412.67	V	2.92	24.3	3.25	0.33	0.01	0.12	33.0
45X-2, 58–59	418.28	O	1.09	9.1	2.82	1.73	0.09	1.49	19.2
45X-3, 116–117	420.36	O	0.13	1.1	2.10	1.97	0.11	1.30	17.9

Note: Abbreviations: O = organic-rich turbidite, V = volcanic turbidite, I = intermediate turbidite, O* = oxidized turbidite top, D = debris flow, BD = below detection, ND = not detected.

Values of the index properties from Hole 952A are presented in Table 9. The overall trends seen in Figure 30 are similar to those seen in the other MAP holes, showing an overall decrease in porosity (Figure 30) to ~55% slightly below 100 mbsf. Between this level and about 300 mbsf the average porosity appears to be roughly constant. Below 300 mbsf the average porosity appears to increase by about 5% possibly as a result of distortion of the cored segments caused by loss of confining pressure upon extraction from the seafloor. However, the change seen in grain density (Figure 30) may argue that this is due either to a change in the primary bulk composition or diagenesis. The distinctive change in properties seen at about 370 mbsf (Figure 29) corresponds to the first occurrence of coarse sands and occasional debris flows in the core. This contrast may be the cause of the distinctive seismic reflector that was the target for Hole 952A.

P-wave Velocity

The DSV apparatus was used successfully on core sections from Hole 952A for the first time on Leg 157. Earlier measurements were characterized by weak arrivals, introducing errors into the estimation of traveltime and a bias toward low velocities. The strength of the received signal was improved by modification of the data acquisition software and hardware. Particularly, the addition of a Tektronix 11401 digitizing oscilloscope to the instrument set up permitted stacking of the received waveform, which diminished the random noise and reinforced the coherent signal and resulted in improved picks of the first arrival and a set of reasonable velocities for the sediments (Table 10 and Fig. 31). Samples were taken approximately every section from Core 1H at 0.77 mbsf through Core 16H at 148.06

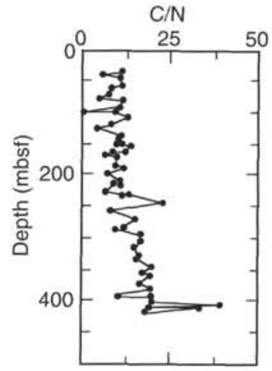

Figure 21. C/N ratio for samples, Hole 952A.

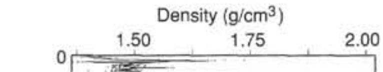

Figure 22. MST density, Hole 952A. Filtered data indicated by lines, raw data by discrete points.

mbsf. Data acquisition ended because below this level the paired transducers split the core upon penetration. Once the core was split the transducers did not couple to the sample and no signal was received by the Tektronix 11401. The velocities range from 1.48 to 1.64 km/s (Fig. 31) similar to the range observed in the MST *P*-wave velocity data (Fig. 23).

Shear Strength

The motorized vane shear and the handheld penetrometer were used to measure the sediment strength, providing a means of comparison between the two instruments. Vane shear measurements were made from Core 1H at 2.38 mbsf, averaging one per section through Core 21X at 188.85 mbsf. The vane shear apparatus failed during the next measurement as a result of mud entering the lower rotational sensor while the vane was being cleaned between measurements. This mud abraded the photo-lithographed disc used to sense rotation.

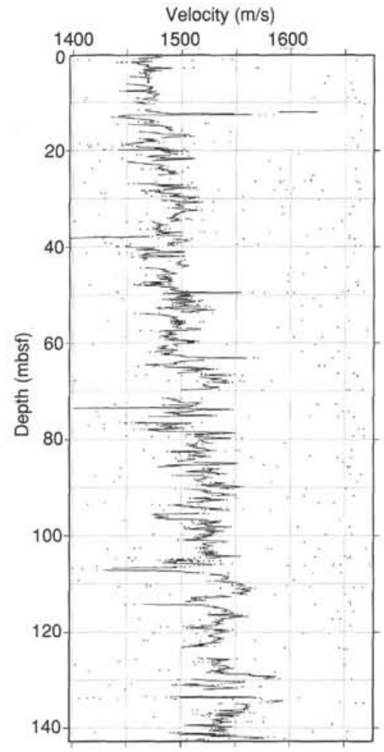

Figure 23. MST velocity, Hole 952A. Filtered data indicated by lines, raw data by discrete points.

Failure occurred when the disc was blank, but this was corrected by replacing the lower rotational sensor with a spare and installing shields on both rotational sensors. Penetrometer measurements were made beginning on Core 6H at 53.86 mbsf and continued until the sediment no longer yielded to the penetrometer probe. Below Core 29X at 271.34 mbsf the probe either chipped the core face or left a small impression. Data are presented in Table 11 and are plotted against depth downhole in Figure 32. Notice that the vane shear and penetrometer values correlate well throughout the interval over which both measurements were made. The data show a general trend of increasing strength downhole from about 0 kPa to 230 kPa, but with a wide scatter throughout, corresponding to lithologic changes within the turbidites. Limitations in the instrumentation may also account for some of the data scatter. In contrast to previous holes, the deeper carbonate turbidites were as strong or stronger than the interbedded clay-rich turbidites, suggesting a change in the primary composition or perhaps the diagenetic history.

DOWNHOLE MEASUREMENTS

Logging Operations

The quad combination tool string was run successfully at Hole 952A. The deployment of the other two planned tool strings was precluded by time constraints arising from the poor hole conditions. The WHC was used to counter ship heave resulting from the mild sea state conditions (0.2–0.7 m heave) during logging and the base of the drill pipe was initially set at 91.6 mbsf. A summary of the logging tool strings used on Leg 157, the basis of their measurement principles, and logging operations are discussed in the "Explanatory Notes" chapter (this volume). A summary of the logging operations at Hole 952A is given in Table 12.

Total penetration in Hole 952A was 425.9 mbsf, but the quad combination tool string was only able to reach 200 mbsf on the first attempt because of an obstruction. Data were recorded at a logging

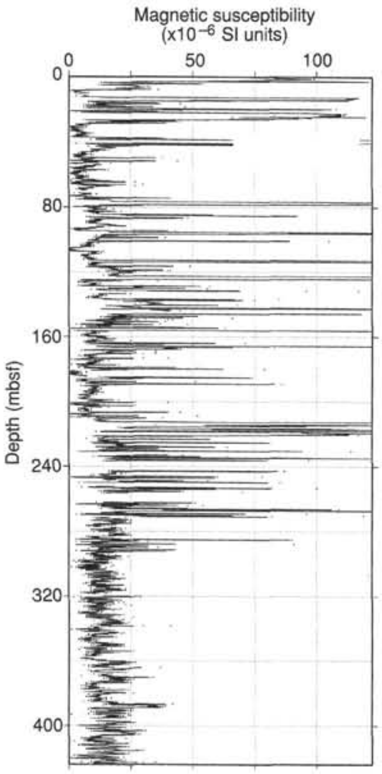

Figure 24. MST magnetic susceptibility, Hole 952A. Filtered data indicated by lines, raw data by discrete points.

speed of 900 ft/hr from 196 to 92 mbsf; a repeat run was then recorded from 157 mbsf to the base of pipe (pulled to 76 mbsf). In order to try to log the lower portion of the hole, the tool string was removed from the hole and the pipe was set just below the obstruction at 200 mbsf, having first been run down to the bottom of the hole. The quad combination was redeployed and the section from 293 to 179 mbsf was logged at 900 ft/hr. At 293 mbsf there was a further obstruction and the tool string was removed from the hole for a second time and the hole was reamed to the bottom and swept with mud to try to clean out any debris. The pipe was then set at 304 mbsf, below the second obstruction, and the quad tool was redeployed. Unfortunately the tool string was unable to make any significant progress into open hole below the end of the drill pipe. A short section was logged from 300 to 291 mbsf, having pulled up the pipe to 291 mbsf, and logging operations had to be terminated because of time constraints.

Log Quality

The main logs from Hole 952A are shown in Figures 33 and 34. The logs are generally of good quality, although above 76 mbsf in the drill-pipe section, the sonic, induction, and density data are invalid, and the natural gamma-ray data are highly attenuated by the presence of the drill pipe. Since the hole was logged in two main sections, some data in the center of the logged section (170–204 mbsf) is also recorded through drill pipe and therefore is highly attenuated. The shaded areas on Figures 33 and 34 indicate the areas that are affected. Hole 952A is rugose in parts, shown by the hole caliper in Figure 34. The white area in the center of the figure shows the diameter of a gauge hole drilled with the XCB coring bit, while the shaded areas show how much wider the hole is than originally drilled. In the comparison of log bulk density to discrete measurements on core (Fig. 35), the log bulk density appears to have some low density "drop-outs" that for the most part correlate with zones of wider borehole. This occurs when pad contact with the borehole wall is incomplete,

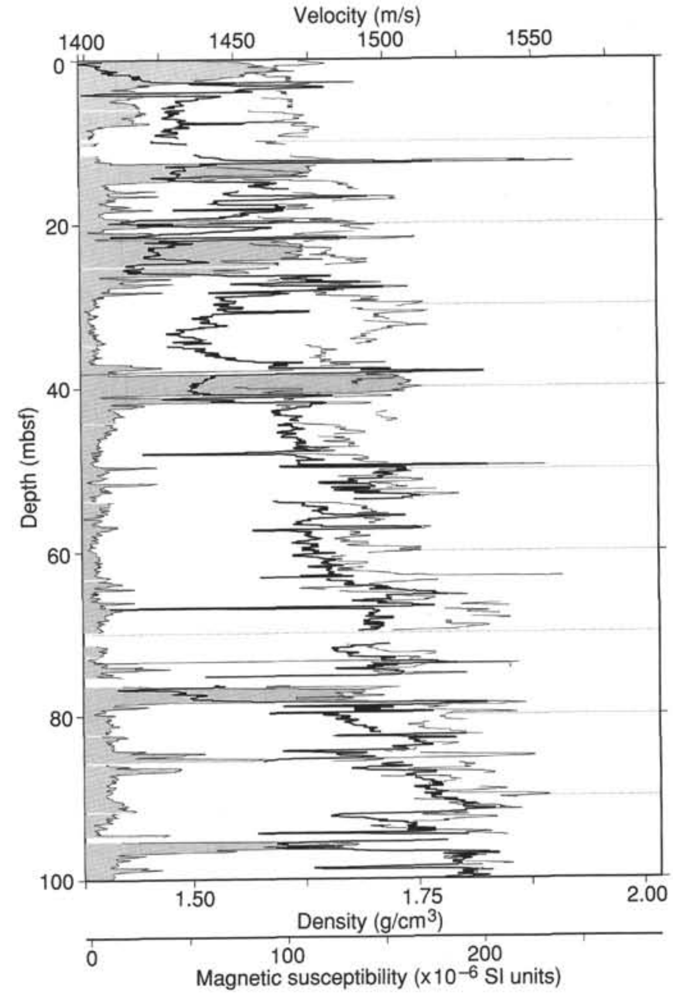

Figure 25. Filtered MST magnetic susceptibility (shading), velocity (light trace), and gamma-ray density (bold trace) for 0–100 mbsf, Hole 952A.

resulting in a small amount of borehole fluid being included with the measurement of sediment density.

For the most part, the velocity data from the logs are of very good quality. Some cycle skipping and other noise is present in the raw log data, but shipboard processing of the traveltimes eliminated most of these excursions. The sonic velocity presented in Figure 34 is the processed data. Post-cruise waveform analysis could improve the quality of these data.

Hole width also affects the natural gamma-ray activity log by raising the count rate where the hole is narrow and lowering it where it is wide. Post-cruise processing will correct for these environmental factors.

Results

Lithology-log Units

The interval logged in Hole 952A (~76–290 mbsf) covers lithologic Unit Ia to Ib (Quaternary to early Miocene), based on the recovered cores (see "Lithostratigraphy," this chapter). The sequence is dominated by unlithified thick turbidite muds separated by thin pelagic ooze in the upper 225 mbsf, and by green turbidites separated by pelagic clay beneath. The core material in the upper part of this hole (above ~280 mbsf) is very similar to the sequences encountered at Sites 950 and 951.

An initial comparison of the logs recorded at this hole and those at Hole 950 show a remarkable similarity. At Hole 950A the se-

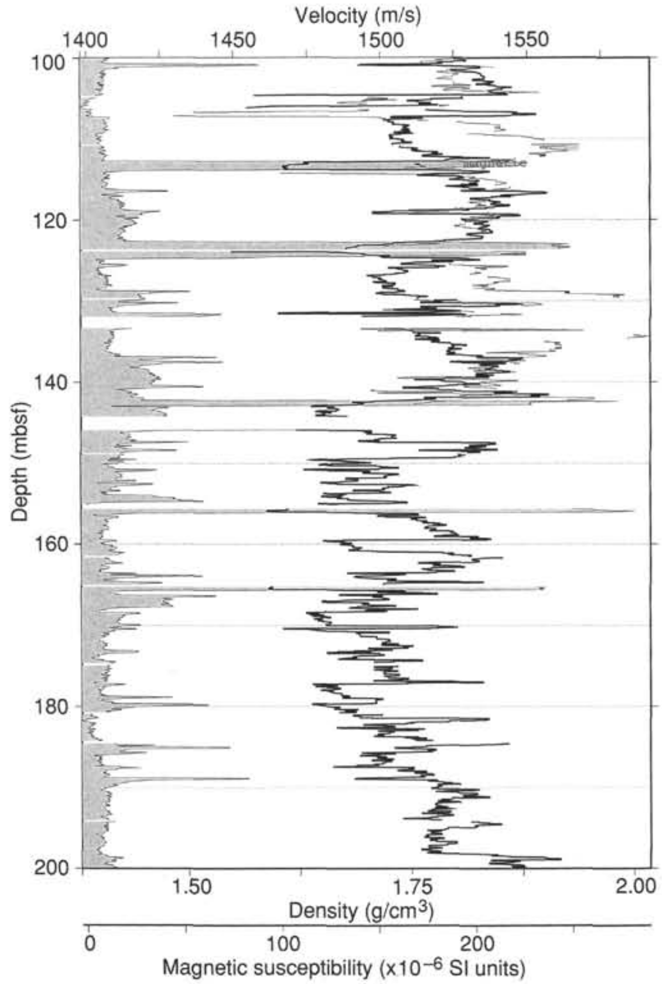

Figure 26. Filtered MST magnetic susceptibility (shading), velocity (light trace), and gamma-ray density (bold trace) for 100–200 mbsf, Hole 952A.

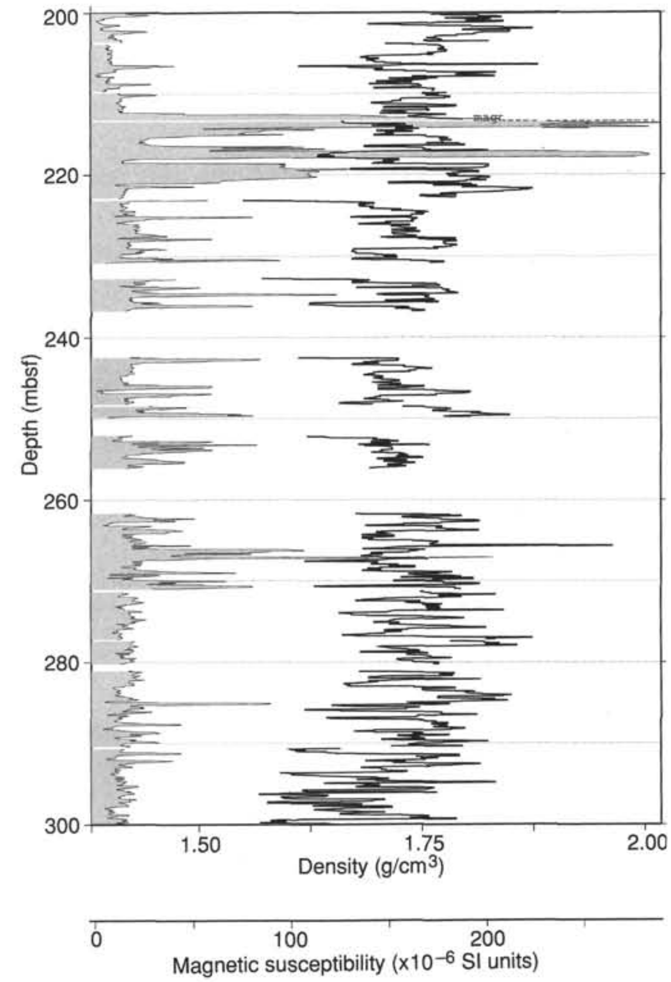

Figure 27. Filtered MST magnetic susceptibility (shading) and gamma-ray density (bold trace) for 200–300 mbsf, Hole 952A.

quence was divided into five logging units based on the wireline data. The most diagnostic of the logs were from the geochemical tool string, which was not run at Hole 952A. Since the gamma-ray logs from the two sites are so similar, the log units chosen at Hole 952A are defined at the correlative point in the gamma-ray record to Hole 950A. Hole 952A is hence divided into three main units, which broadly correspond to the lithologic units described in the cores.

Log Unit I covers the region from the top of the logged section ~76 to 200 mbsf. This unit is characterized by a cyclical gamma-ray log reflecting the varying clay component of this sequence of thick interbedded turbidites (Fig. 33). The high gamma-ray values correspond to the clay-rich organic and volcanic turbidites, and the low values correspond to the low-clay, carbonate-rich turbidites. The physical log responses of density, resistivity, and sonic velocity (Fig. 34) also exhibit this cyclicity and show an increase of values with depth, following a normal compaction trend. At the base of this log unit is a thick volcanic turbidite, estimated by the log data to be 3.5 m thicker than the corresponding turbidite in Hole 950A.

Log Unit II (200–233 mbsf), as in Hole 950A, is a transitional zone between log Units I and III. This transition represents the change from the thick, periodic, more carbonate-rich sequence of turbidites of log Unit I to the carbonate-poor, less cyclic, and generally thinner turbidites of log Unit III below. This transition is reflected in the logs by an increasing gamma-ray and a sharp reversal in trend of the velocity log (Figs. 33 and 34).

Log Unit III (233–280 mbsf; the base of the logged section) is characterized by a higher and less cyclic gamma-ray (Fig. 33) reflecting the higher clay and low carbonate content of the formation, as observed at Hole 950C (see "Downhole Measurements" section of "Site 950" chapter, this volume). The physical log responses show a decrease in variance on transition into this unit but no major trend downhole (Fig. 34).

Correlation between Sites 950 and 952

The most striking feature of the wireline data is the correlation of the gamma-ray log with that of Hole 950A (Fig. 36). The correlation is excellent and it should allow for a detailed depth comparison between the two sites, enabling differences in sedimentation rates to be determined. The offset in depth noted in the cores between the two sites is confirmed by the logs, with the corresponding lithologies about 8 m higher in Hole 952A in the upper portion of the hole covered by the logs (200–80 mbsf). Below this level the offset is less marked, just 2–3 m higher in Hole 952. This depth change appears to be focused over the interval 185–200 mbsf where a distinctive volcanic turbidite unit is thicker in Hole 952 than in Hole 950A (Fig. 36).

It was noted in the description of core material that some of the carbonate turbidites were variously present between Sites 950, 951, and 952 and were suspected of being localized events from nearby

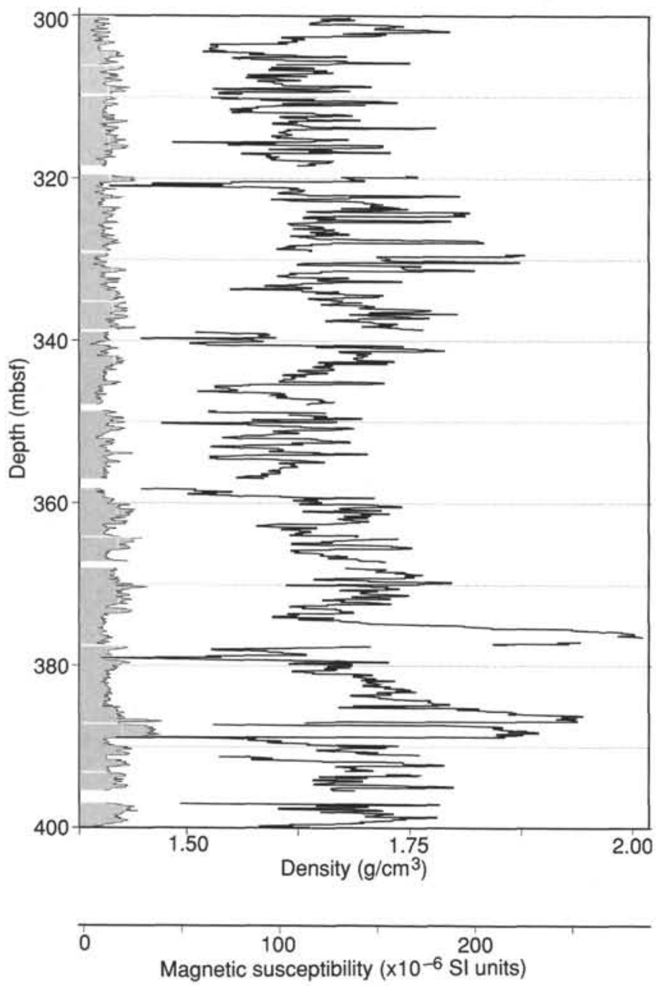

Figure 28. Filtered MST magnetic susceptibility (shading) and gamma-ray density (bold trace) for 300–400 mbsf, Hole 952A.

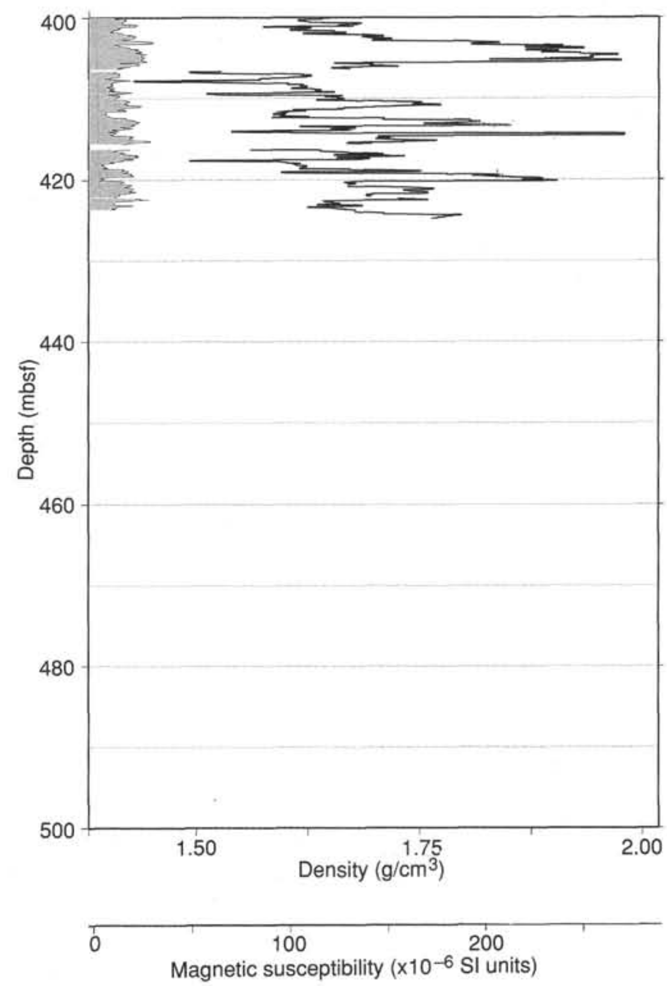

Figure 29. Filtered MST magnetic susceptibility (shading) and gamma-ray density (bold trace) for 400 to total depth mbsf, Hole 952A.

seamounts. The logs seem to confirm this; for example, at ~140 mbsf Hole 950A has three distinct carbonate units, discernible as three troughs in the gamma-ray log (Fig. 48, "Site 950" chapter, this volume). In Hole 952A at the corresponding interval (~132 mbsf), only one carbonate was recovered in the cores and only one low gamma-ray peak is observed on the gamma-ray log (Fig. 36). This confirms that the observed difference in the number of carbonate units is not attributable to incomplete recovery, but is a function of local variations in deposition.

Temperature

The Lamont-Doherty temperature tool was deployed three times on the quad combination tool string in Hole 952A. An accurate thermal gradient cannot be obtained from these measurements; cold seawater is circulated in the hole during drilling, which cools the adjacent formation. A minimum of three bottom-hole temperature measurements over a period of time are required to extrapolate the virgin bottom-hole temperature and hence calculate the true thermal gradient. The quad tool string reached three different depths on each logging run, and in addition, fluid circulated between the logging runs, disrupting the thermal rebound of the hole. Nevertheless, a temperature of 9.95°C was obtained at 293 mbsf, and with a mud-line temperature of 2.5°C the thermal gradient must be greater than 25°C/km.

Porosity Estimates from Resistivity

Porosity can be determined from the resistivity logs by using Archie's equation (Archie, 1942):

$$S_w{}^a = aR_w/f^mR_t,$$

where S_w is the water saturation, equal to one for these virtually hydrocarbon-free sediments, R_w is the resistivity of the formation water, f is the fractional porosity, R_t is the measured formation resistivity, and both a and m are constants depending on lithology and pore space geometry.

In this case we calculated porosity using the medium phaser induction resistivity log (IMPH) from the dual induction tool, with set values of $a = 1$ and $m = 2.0$. R_w is calculated based on its known relationships to temperature and salinity (Keller, 1982), temperature was taken from the Lamont-Doherty temperature tool, and interstitial salinities from core measurements (see "Inorganic Geochemistry," this

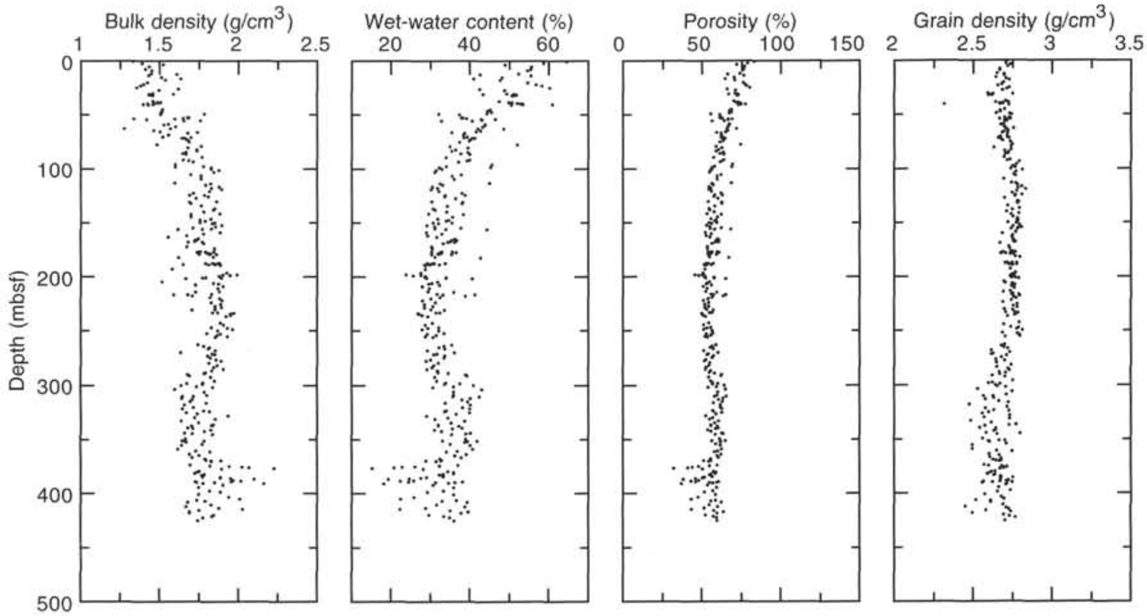

Figure 30. Bulk density (Method B), wet-water content, porosity (Method C), and grain density (Method C), Hole 952A.

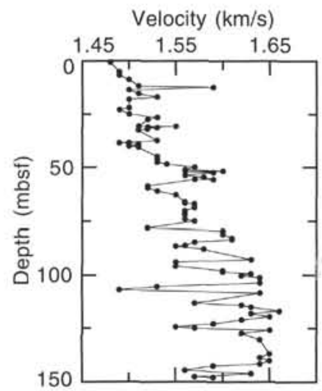

Figure 31. Longitudinal compressional-wave velocity, Hole 952A.

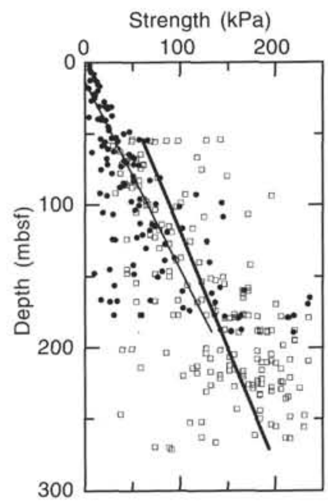

Figure 32. Strength data determined by vane shear (filled circles) and hand-held penetrometer methods (open squares), Hole 952A.

chapter). The calculated porosities show an excellent correlation with those determined from discrete core samples (Fig. 37), verifying the high quality of the induction log data.

SEDIMENT ACCUMULATION RATES

Sediment accumulation rates for Site 952 are based on 17 nannofossil, 2 planktonic foraminifer, and 6 paleomagnetic age determinations (Table 13). As in the previous two sites, most of the age data is concentrated in the upper part of the hole (0–200 mbsf) where calcium carbonate is better preserved in the pelagic layers. All datum levels were identified in pelagic layers except for the FO of *Discoaster quinqueramus* (8.4 Ma), which was in a turbidite. The estimations of accumulation rates in the deeper part of the hole will be improved by later study of nannofossil FOs in turbidite sequences.

Sediment accumulation rate curves have been produced firstly for stacked pelagic layers alone (Figs. 38 and 39) and secondly for the total sediment including turbidites and pelagic layers (Fig. 40). The pelagics-only curve is based on the stacked thicknesses of pelagic clays, marls, and oozes and gives an indication of the background accumulation rate.

Pelagic Accumulation Rates

The pelagic accumulation rate curve at Site 952 is not as well constrained as at the previous two sites. The paleomagnetic data appears to be less reliable, due in part to probable missing sediment between some of the APC cores, and in part to a poorer signal. An approximately constant accumulation rate of 4.3 m/m.y. from zero to 2.6 Ma can be calculated, producing a lower rate of 1.3 m/m.y. from 2.6 to 5.04 Ma. Two nannofossil datum levels, the FO of *Discoaster triradiatus* and LO of *Discoaster pentaradiatus*, suggest the change in accumulation rates occur at a younger age of 2.15 Ma rather than 2.6 Ma. However, the improved preservation of calcium carbonate, which is the cause of the increased rates for the last 2.6 Ma in Sites 950 and 952 is seen in the sediments nearer to the 2.6 Ma date. Both possibilities are shown in Figure 38.

In the lower part of the sequence, below 5.04 Ma, the sediment accumulation rate is poorly constrained (Fig. 39). The FO of *Discoaster*

Table 9. Index properties, Hole 952A.

Core, section, interval (cm)	Depth (mbsf)	WCw (%)	WCd (%)	BDb (g/cm³)	BDc (g/cm³)	GDb (g/cm³)	GDc (g/cm³)	DDb (g/cm³)	DDc (g/cm³)	Porb (%)	Porc (%)	VRb	VRc
157-952A-													
1H-1, 45–47	0.45	64.43	181.14	1.33	1.32	2.93	2.71	0.47	0.47	83.82	82.74	5.18	4.80
1H-2, 102–104	2.52	58.66	141.92	1.39	1.38	2.84	2.71	0.58	0.57	79.73	78.95	3.93	3.75
1H-3, 60–62	3.60	48.91	95.72	1.53	1.51	2.87	2.74	0.78	0.77	72.85	71.88	2.68	2.56
1H-4, 76–78	5.26	55.50	124.72	1.43	1.42	2.86	2.72	0.64	0.63	77.67	76.81	3.48	3.31
1H-6, 56–58	8.06	55.37	124.07	1.41	1.41	2.64	2.67	0.63	0.63	76.17	76.36	3.20	3.23
1H-7, 25–27	9.25	54.56	120.06	1.45	1.42	2.89	2.67	0.66	0.65	77.20	75.76	3.39	3.12
2H-3, 38–40	11.82	52.22	109.28	1.45	1.45	2.65	2.65	0.69	0.69	73.87	73.87	2.83	2.83
2H-3, 103–105	12.47	42.61	74.25	1.61	1.59	2.79	2.69	0.92	0.91	66.91	66.13	2.02	1.95
2H-4, 76–78	13.70	55.40	124.20	1.43	1.42	2.83	2.70	0.64	0.63	77.42	76.57	3.43	3.27
2H-5, 94–96	15.38	48.04	92.44	1.51	1.50	2.70	2.64	0.79	0.78	70.91	70.45	2.44	2.38
2H-6, 89–91	16.83	40.82	68.97	1.63	1.62	2.76	2.71	0.97	0.96	65.03	64.55	1.86	1.82
2H-7, 64–66	18.08	47.52	90.55	1.54	1.52	2.80	2.73	0.81	0.80	71.24	70.69	2.48	2.41
3H-1, 70–72	20.00	54.48	119.70	1.42	1.43	2.67	2.69	0.65	0.65	75.76	75.87	3.12	3.14
3H-2, 124–126	22.04	56.64	130.61	1.40	1.40	2.69	2.68	0.61	0.61	77.43	77.35	3.43	3.42
3H-3, 75–77	23.05	58.03	138.24	1.38	1.38	2.64	2.66	0.58	0.58	78.05	78.18	3.56	3.58
3H-4, 119–121	24.99	60.09	150.55	1.35	1.36	2.63	2.73	0.54	0.54	79.46	80.04	3.87	4.01
3H-5, 108–110	26.38	42.28	73.25	1.62	1.60	2.80	2.71	0.93	0.92	66.70	65.95	2.00	1.94
3H-6, 64–66	27.44	48.66	94.79	1.49	1.50	2.64	2.68	0.77	0.77	70.97	71.29	2.44	2.48
4H-2, 36–38	30.66	49.31	97.30	1.46	1.48	2.48	2.59	0.74	0.75	70.16	71.12	2.35	2.46
4H-2, 51–53	30.81	43.32	76.41	1.59	1.59	2.74	2.75	0.90	0.90	67.12	67.23	2.04	2.05

Notes: WCw = water content (% wet sample weight), WCd = water content (% dry sample weight), BD = bulk density, GD = grain density, DD = dry density, Por = porosity, and VR = void ratio. Suffixes "b" and "c" on column heads indicate value calculated using Method B and Method C, respectively (see "Explanatory Notes," this volume).

Only a part of this table is reproduced here. The entire table appears on the CD-ROM (back pocket).

Table 10. *P*-wave velocities, Hole 952A.

Core, section, interval (cm)	Depth (mbsf)	Velocity (km/s)	Temp (°C)
157-952A-			
1H-1, 77–84	0.77	1.48	
1H-4, 60–67	5.10	1.49	
1H-6, 116–123	8.66	1.50	18.8
1H-5, 74–81	6.74	1.49	19.2
2H-3, 100–107	12.44	1.59	
2H-3, 36–43	11.80	1.51	
2H-4, 74–81	13.68	1.50	
2H-5, 93–100	15.37	1.51	
2H-6, 87–94	16.81	1.53	
2H-7, 61–68	18.05	1.50	19.3
3H-2, 122–129	22.02	1.50	18.8
3H-3, 73–80	23.03	1.49	18.5
3H-4, 116–123	24.96	1.50	18.5
3H-5, 108–115	26.38	1.53	18.8
3H-6, 62–69	27.42	1.52	19.1
4H-2, 133–140	31.63	1.52	18.4
4H-2, 96–103	31.26	1.53	19.0
4H-2, 67–74	30.97	1.52	19.5
4H-2, 49–56	30.79	1.55	20.1
4H-2, 32–39	30.62	1.51	20.0

Only a part of this table is reproduced here. The entire table appears on the CD-ROM (back pocket).

Table 11. Strength measurements, Hole 952A.

Core, section, interval (cm)	Depth (mbsf)	Vane (kPa)	Res (kPa)	Pen (kPa)
157-952A-				
1H-2, 88–89	2.38	4.7	1.1	
1H-4, 60–61	5.10	4.8	1.3	
1H-5, 78–79	6.78	6.4	3.2	
1H-6, 120–121	8.70	9.1	4.8	
2H-3, 40–41	11.84	10.1	4.3	
2H-3, 104–105	12.48	5.8	1.5	
2H-4, 78–79	13.72	12.5	4.4	
2H-5, 93–94	15.37	13.1	6.8	
2H-6, 91–92	16.85	15.5	6.9	
2H-7, 65–66	18.09	3.7	1.8	
3H-1, 70–71	20.00	13.4	7.4	
3H-2, 126–127	22.06	9.5	5.8	
3H-3, 77–78	23.07	10.6	5.7	
3H-4, 120–121	25.00	10.2	4.9	
3H-5, 110–111	26.40	6.8	2.4	
3H-6, 66–67	27.46	20.3	9.9	
4H-2, 36–37	30.66	20.5	6.9	
4H-2, 53–54	30.83	15.1	3.9	
4H-2, 71–72	31.01	23.1	13	
4H-2, 100–101	31.30	27.8	3.7	

Note: Vane = undrained shear strength as measured by the vane shear, Res = residual shear strength, and Pen = unconfined shear strength as measured by the penetrometer, converted to kPa.

Only a part of this table is reproduced here. The entire table appears on the CD-ROM (back pocket).

kugleri between 25.68 and 26.36 m in the stacked pelagic sequence (342.8–364.5 mbsf) is based on very few specimens. The occurrence of *Reticulofenestra pseudoumbilicus* at 27.61 m in the stacked pelagic sequence (415.35 mbsf) suggests an age younger than 13.1 Ma for this level near the base of the drilled sequence. The position of these two datum levels in the stacked pelagic sequence suggests a slightly higher pelagic accumulation rate for the pelagic interval below 5.04 Ma, although some difficulty was experienced in estimating the thicknesses of pelagic layers in the deeper parts of Hole 952A.

Total Sediment Accumulation Rates

The average accumulation rate between zero and 5.56 Ma (0–187 mbsf) is 31.1 m/m.y. (Fig. 40). The datum levels below 5.56 Ma are poor and do not constrain the curve well, but a continuation of the same rate to at least 8.4 Ma (262 mbsf) is feasible. Beyond this the rate would need to be somewhat higher to 415 mbsf although the exact rate is unknown.

ROCK-EVAL

Rock-Eval Pyrolysis Characterization of Organic Matter at MAP Sites 950, 951, and 952

Organic matter preserves a record of transport processes, surface-water productivity, and degree of diagenetic alteration. Thermal alteration may also be discerned. Organic-rich turbidites on the MAP, have been shown to display homogeneous repeated layers of sediment, generally containing between 0.5% and 2% organic carbon

Table 12. Summary of logging operations, Hole 952A.

Date (August 1994)	Time (UTC)	Activity
18	16:15	Last core on deck. Prepare hole for logging.
19	00:45	Rig up NGT-LSS-CNT-HLDT-DIT (+TLT).
	01:35	RIH with NGT-LSS-CNT-HLDT-DIT.
	03:20	Start downgoing log from ~95 to TD 200 mbsf where downward progress halted by an obstruction.
	04:49	Upgoing log at 900 ft/hr from 196 to 92 mbsf. RIH.
	04:51	Repeat upgoing log at 900 ft/hr from 157 mbsf to EOP (pulled to 76 mbsf).
	05:20	POOH. Decision to set pipe below obstruction in attempt to log bottom half of hole.
	07:30	Trip down to TD with drill pipe, pipe set at 207 mbsf.
	10:05	RIH with NGT-LSS-CNT-HLDT-DIT (+TLT).
	12:17	Downward progress halted by an obstruction at 294 mbsf. Upgoing log from 293 mbsf to EOP (pulled to 179 mbsf) at 900 ft/hr. POOH.
	14:46	Put on top drive and ream to TD, flush hole with sepiolite mud. Pipe set at 304 mbsf.
	20:35	RIH with NGT-LSS-CNT-HLDT-DIT (+TLT). Obstruction encountered immediately in open hole. Pull pipe to 291 mbsf. Redeploy tool and record upgoing log from 300 to 291 mbsf.
	23:05	POOH. Time constraints prohibit further logging attempts.
20	00:40	Tool out of hole. Rig down (1 hr). End of logging operations.

Note: Drillers TD = 425.9 mbsf, WD = 5442.7 mbrf, EOP = 91.59 mbsf.

with C/N ratios varying from 6 to 22. Most of the turbidites display an oxidized top in which all labile organic carbon has been destroyed. This indicates that seafloor conditions have been consistently highly oxygenated, so the ultimate source of the organic matter must be elsewhere.

Sediments with relatively high organic matter contents have been studied before in shallower water settings (e.g., Curray, Moore, et al., 1982) and have been proposed as modern equivalents of black shales. As such, they are of interest regarding their oil and gas potential, their present degree of maturity, and the source of their organic matter. During Leg 157, Rock-Eval pyrolysis (Peters, 1986) was used onboard ship to characterize organic facies on the MAP, where homogeneous organic-rich turbidites occur throughout the sequences at Sites 950, 951, and 952.

Samples

A few comments should be made concerning the analytical data (Table 14), which are subject to occasional aberrations. For example, Section 157-952A-31X-45 yielded a high organic carbon value of 3.99%, but other parameters are very low. This could be due to the measured carbonate value being too low; the calculated TOC by difference would then be too high. This particular sample originated from a gray (=volcanic) turbidite, and should not contain much organic carbon. Anomalous Section 157-951A-25X-32 produced an organic carbon value of 5.12%; repeated analyses gave the same organic carbon value. In this case, the Rock-Eval parameters are reasonable and high values probably represent contamination (e.g., core liner or drilling fluid). Overall, however, such contamination appears to be negligible in the data set.

A total of 32 samples (Table 14) were analyzed on the Rock-Eval instrument. Samples were chosen from results of earlier CSN-analyses and consisted of two categories: (1) those containing >1.3% organic carbon and (2) those containing between 0.5%–1.0% organic carbon. Sample weights were confined to 100 and 101 mg to ensure reproducibility of measurements. A variety of parameters are obtained by the Rock-Eval pyrolysis method (Table 14). These are discussed below with reference to the maturity of the sediments, source-rock type, and potential.

Maturity of Sediments

The degree of maturity of the sediment (i.e., the degree of alteration toward oil or gas production) may be indicated by two criteria: (1) T_{max} and (2) production index (PI). T_{max} for samples with TOC >1.3% (Fig. 41) ranged from 400°C to 430°C, indicating an immature condition for these sediments. A maximum value of 430°C was found at 109 mbsf (TOC = 1.85%) at Site 952. The lean-TOC category sometimes showed T_{max} values below 400°C, but in general, low TOC contents gave unpredictable parameters, which are difficult to assess.

The PI should be used with discretion, because of the potential migration of hydrocarbons. However, maturity is normally indicated by the oil-formation zone, beginning at PI values of between 0.05 and 0.10; maximum oil formation is normally indicated by PI of 0.30 to 0.40. Average PI values are around 0.2 for the MAP organic-rich turbidites (Fig. 41), which would put these sediments in the oil formation zone (Peters, 1986).

Origin of Organic Matter

The source of the organic matter may be derived from shipboard data by either using the CNS-data to compute C/N ratios, or by plotting the hydrogen indices (HI) (Table 14) against oxygen indices (OI) in a variation of the van Krevelen diagram (Espitalié et al., 1977). In immature sediments, marine-derived organic matter has HI values of 200 to 400 mg/HC/gC, while terrigenous organic matter has HI values of 100 mg/HC/gC or less. However, the HI tends to be lowered if TOC is low (<0.5%) or if mineral matrix effects are large (i.e. if the clay mineral content is high in comparison with pure kerogen samples). Clay mineral contents of MAP organic-rich turbidites are invariably high, and these may influence several Rock-Eval parameters. The hydrogen index may be lowered and the oxygen index increased by the presence of both clay minerals and carbonates (Espitalié et al., 1980, 1985).

Figure 42 shows HI plotted against OI Sites 950, 951, and 952. The majority of the data points fall in a field between kerogen type II (marine) and kerogen type III (terrigenous). This is interpreted as representing a mixture between the two types of organic matter. Bearing in mind likely mineral matrix effect, the data set should be shifted toward area II, where the marine component prevails. C/N values generally also fall in-between the marine and terrigenous categories, so there is agreement between the two methods. It is concluded that organic matter at MAP Sites 950, 951, and 952 consists of a mixture of marine and terrigenous sources, with a predominance of marine-derived material.

Source Rock Potential

Characterization of source rocks is done by an assessment of TOC contents, their petroleum potential ($S_1 + S_2$), the degree of maturity (as given by T_{max} and PI), their hydrocarbons content (given by S_1 and

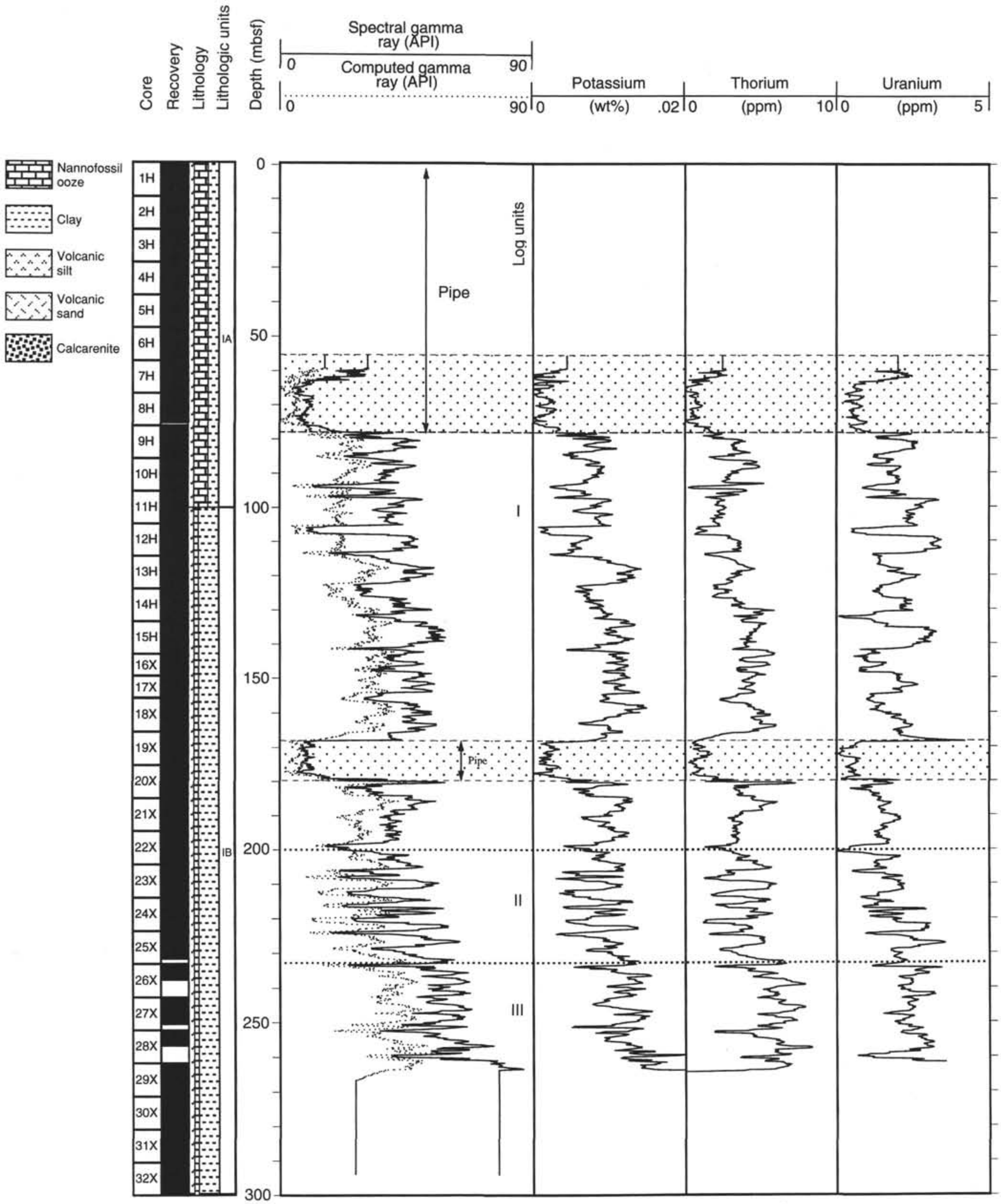

Figure 33. Hole 952A natural gamma-ray data from the NGT recorded on the quad combination tool string. The left track shows the total and the computed gamma-ray counts; tracks for K, U, and Th components of the total gamma-ray signal follow. Dotted pattern indicates intervals where log responses are attenuated by the drill pipe.

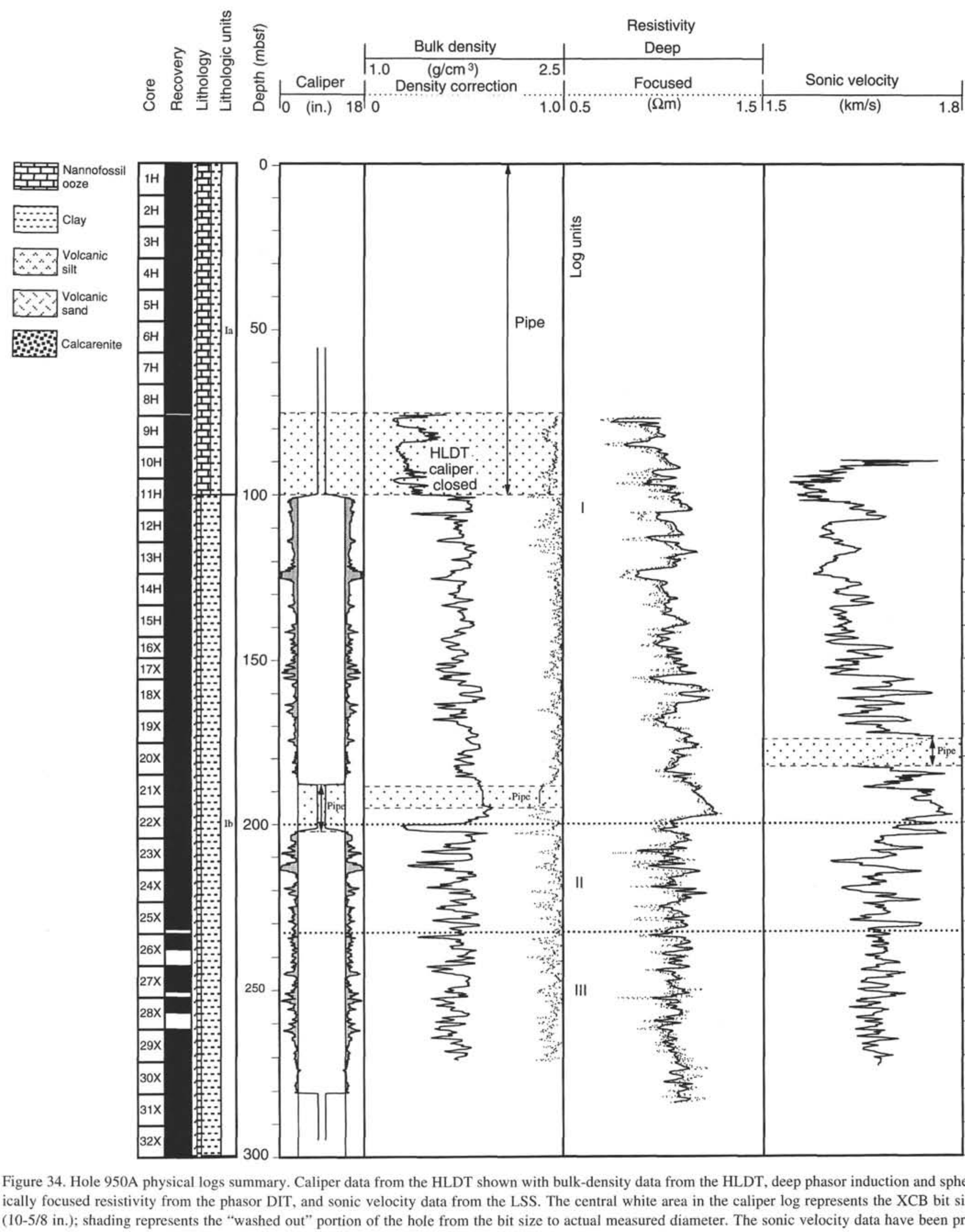

Figure 34. Hole 950A physical logs summary. Caliper data from the HLDT shown with bulk-density data from the HLDT, deep phasor induction and spherically focused resistivity from the phasor DIT, and sonic velocity data from the LSS. The central white area in the caliper log represents the XCB bit size (10-5/8 in.); shading represents the "washed out" portion of the hole from the bit size to actual measured diameter. The sonic velocity data have been processed to remove cycle skips.

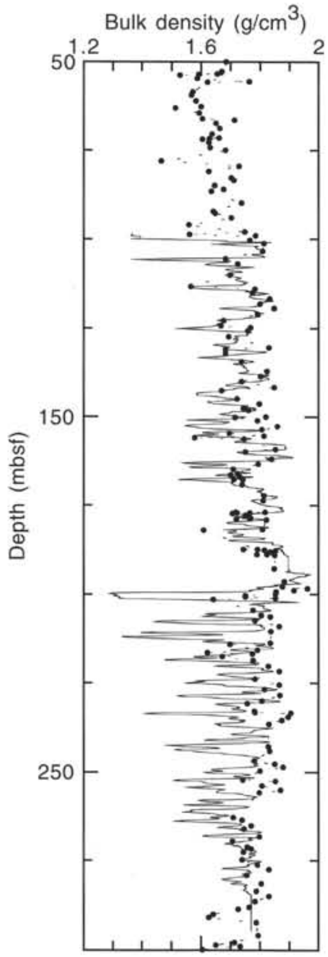

Figure 35. Hole 952A bulk-density log from the HLDT plotted as a function of depth against density measurements on discrete core samples (see "Physical Properties," this chapter).

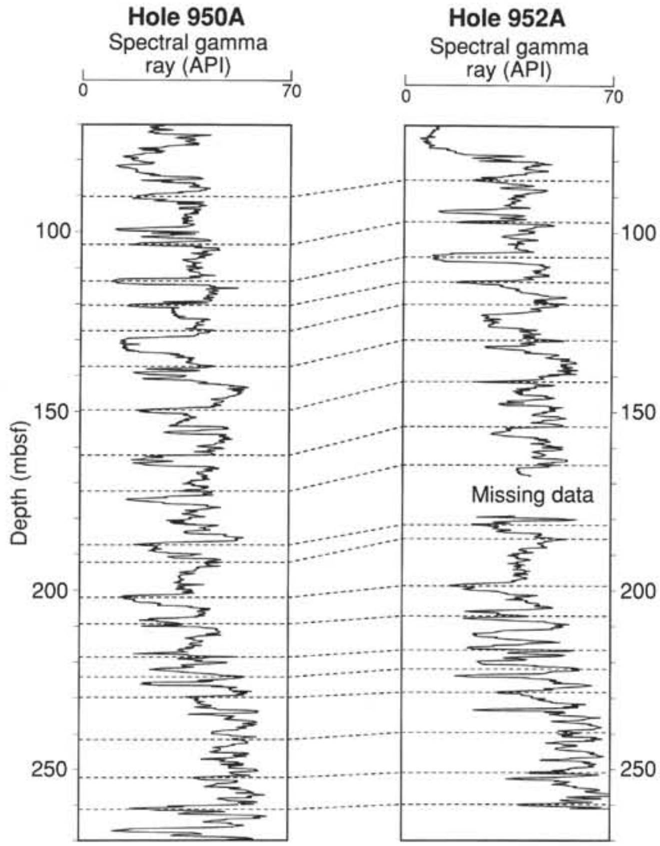

Figure 36. Comparison of the total gamma-ray logs recorded at Holes 950A and 952A. The dotted tie lines indicate visual correlation points between the two logs.

the type of organic matter, as indicated by HI/OI or HI/T_{max} diagrams). To classify source rocks, the total petroleum potential is given by $S_1 + S_2$ (i.e., the amount of hydrocarbon that has already been produced and is found in the sediment rocks, plus the amount of hydrocarbons that can be produced by heating and breaking up the kerogen in the sediment). $S_1 + S_2$ is measured in mgC/g sediment. This combined value can be used to classify the sediment as a poor to very good source rock. $S_1 + S_2$ values obtained in the present study varied between 0.32 and 6.21 mgC/g sediment (Fig. 43). Samples containing 5 mgC/g are considered to be good source rocks. An average value for Site 950 over the depth interval 247–294 mbsf (where a representative section can be found) is 3.7 mgC/g, classifying these turbidites as fair source rocks. At Site 951, the sequence between 181–310 mbsf gives an average value of 3.1 mgC/g sediment, which also indicates a fair source rock. At Site 952 the interval from 260–360 mbsf yields an average $S_1 + S_2$ value of 4.4 mgC/g, again representing a fair source rock.

The petroleum potential (PC) corresponds to the maximum quantity of producible hydrocarbons from a source rock. Results in this study are given in Figure 43, which shows that PC follows S_1 and S_2 in these sediments. Predictably, TOC-lean samples show a distinctly lower hydrocarbon potential with respect to both S_1, S_2, and PC values.

Discussion

Earlier studies have shown that the organic-rich turbidites have been transported along pathways north and south of the Canary Islands from the continental slope of northwestern Africa (Weaver et al., 1992; Masson, 1994). The source area lies at the intersection of the oxygen-minimum layer with the continental slope and is an area of high productivity in the ocean (Lancelot, Seibold, et al., 1977; Sibuet, Ryan, et al., 1979). Results for Sites 950–952 indicate a predominantly marine source of the organic matter but with some terrestrial input, which is compatible with MAP turbidites being derived from high-productivity marine environments off the northwestern Africa coast. Aeolian lipids have been detected in earlier studies of continental slope sediments at Site 397 (Sibuet, Ryan, et al., 1979).

The relatively homogeneous content and composition of organic-rich matter in organic turbidites at the three MAP sites offer the possibility of studying long-term and short-term variations in marine and terrigenous organic carbon fluxes (cf. Stein, 1991). These in turn should provide evidence of changing organic productivity and climate during a long, well-documented time period, with the likelihood of establishing correlations with similar long-term records at Sites 369, 370, 397, 645, 657, 658, 907, and 909 (Lancelot, Seibold, et al., 1977; Sibuet, Ryan, et al., 1979; Srivastava, Arthur, Clement, et al., 1987;Ruddiman, Sarnthein, Baldauf, et al., 1988; Myhre, Thiede, Firth, et al., 1995). Organic turbidites on the MAP offer a source rock of good potential for gas and oil, but the level of thermal maturity is low.

REFERENCES

Archie, G.E., 1942. The electrical resistivity log as an aid in determining some reservoir characteristics. *Trans. Am. Inst. Min. Metall. Pet. Eng.*, 146:54–62.

Curray, J.R., Moore, D.G., et al., 1982. *Init. Repts. DSDP*, 64 (Pts. 1 and 2): Washington (U.S. Govt. Printing Office).

de Lange, G.J., Jarvis, I., and Kuijpers, A., 1987. Geochemical characteristics and provenance of late Quaternary sediments from the Madeira

Abyssal Plain, North Atlantic. *In* Weaver, P.P.E., and Thomson, J. (Eds.), *Geology and Geochemistry of Abyssal Plains.* Geol. Soc. Spec. Publ. London, 31:147–165.

Ericson, D.B., Ewing, M., Wollin, G., and Heezen, B.C., 1961. Atlantic deep-sea sediment cores. *Geol. Soc. Am. Bull.,* 72:193–286.

Ericson, D.B., and Wollin, G., 1956. Correlation of six cores from the equatorial Atlantic and Caribbean. *Deep-Sea Res.,* 3:104–125.

————, 1968. Pleistocene climates and chronology in deep-sea sediments. *Science,* 162:1227–1234.

Espitalié, J., Laporte, J.L., Leplat, P., Madec, M., Marquis, F., Paulet, J., and Boutefeu, A., 1977. Méthode rapide de caractérisation des roches mères, de leur potentiel pétrolier et de leur degré d'évolution. *Rev. Inst. Fr. Pet.,* 32:23–42.

Espitalié, J., Madec, M., and Tissot, B., 1980. Role of mineral matrix in kerogen pyrolysis: influence on petroleum generation and migration. *AAPG Bull.,* 64:59–66.

Espitalié, J., Senga Makadi, K., and Trichet, J., 1985. Role of the mineral matrix during kerogen pyrolysis. *In* Schenck, P.A. (Ed.), *Advances in Organic Geochemistry 1983:* Oxford (Pergamon Press).

Keller, G.V., 1982. Electrical properties of rocks. *In* Carmichael, R.S. (Ed.), *Handbook of Physical Properties of Rocks* (Vol. 1): Boca Raton, FL (CRC Press), 217–293.

Lancelot, Y., Seibold, E., et al., 1978. *Init. Repts. DSDP,* 41: Washington (U.S. Govt. Printing Office).

Masson, D.G., 1994. Late Quaternary turbidity current pathways to the Madeira Abyssal Plain and some constraints on turbidity current mechanisms. *Basin Res.,* 6:17–33.

Myrhe, A.M., Thiede, J., Firth, J.V., et al., 1995. *Proc. ODP, Init. Repts.,* 151: College Station, TX (Ocean Drilling Program).

Peters, K.E., 1986. Guidelines for evaluating petroleum source rock using programmed pyrolysis. *AAPG Bull.,* 70:318–329.

Pujol, C., and Duprat, J., 1983. Quaternary planktonic foraminifers of the southwestern Atlantic (Rio Grande Rise) Deep Sea Drilling Project Leg 72. *In* Barker, P.F., Carlson, R.L., Johnson, D.A., et al., *Init. Repts. DSDP,* 72: Washington (U.S. Govt. Printing Office), 601–615.

Rothwell, R.G., Pearce, T.J., and Weaver, P.P.E., 1992. Late Quaternary evolution of the Madeira Abyssal Plain, Canary Basin, NE Atlantic. *Basin Res.,* 4:103–131.

Ruddiman, W., Sarnthein, M., Baldauf, J., et al., 1988. *Proc. ODP, Init. Repts.,* 108 (Section 1): College Station, TX (Ocean Drilling Program).

Searle, R.C., 1987. Regional setting and geophysical characterization of the Great Meteor East area in the Madeira Abyssal Plain. *In* Weaver, P.P.E., and Thomson, J. (Eds.), *Geology and Geochemistry of Abyssal Plains.* Spec. Publ. Geol. Soc. London, 31:49–70.

Sibuet, J.-C., Ryan, W.B.F., et al., 1979. *Init. Repts. DSDP,* 47 (Pt. 2): Washington (U.S. Govt. Printing Office).

Srivastava, S.P., Arthur, M., Clement, B., et al., 1987. *Proc. ODP, Init. Repts.,* 105: College Station, TX (Ocean Drilling Program).

Stein, R., 1991. Organic carbon accumulation in Baffin Bay and paleoenvironment in High Northern Latitudes during the past 20 m.y. *Geology,* 19:356–359.

Weaver, P.P.E., and Kuijpers, A., 1983. Climatic control of turbidite deposition on the Madeira Abyssal Plain. *Nature,* 306:360–363.

Weaver, P.P.E., and Rothwell, R.G., 1987. Sedimentation on the Madeira Abyssal Plain over the last 300,000 years. *In* Weaver, P.P.E., and Thompson, J. (Eds.), *Geology and Geochemistry of Abyssal Plains.* Geol. Soc. Spec. Publ. London, 31:71–86.

Weaver, P.P.E., Rothwell, R.G., Ebbing, J., Gunn, D., and Hunter, P.M., 1992. Correlation, frequency of emplacement and source directions of megaturbidites on the Madeira Abyssal Plain. *Mar. Geol.,* 109:1–20.

Weaver, P.P.E., Thomson, J., and Jarvis, I. 1989. The geology and geochemistry of Madeira Abyssal Plain sediments: a review. *In* Freeman, T.J. (Ed.), *Advances in Underwater Technology, Ocean Science and Offshore Engineering* (Vol. 18): London (Graham and Trotman), 51–78.

Young, J.R. Flores, J.-A., and Wei, W., 1994. A summary chart of Neogene nannofossil magnetobiostratigraphy. *J. Nannoplankton Res.,* 16:21–27.

Ms 157IR-106

NOTE: For all sites drilled, core-description forms ("barrel sheets") and core photographs can be found in Section 3, beginning on page 181. Smear-slide and thin-section data are given in Section 4, beginning on page 305. The CD-ROM (back pocket, this volume) contains physical properties and geochemical data, MST data, logging data, and color core photographs (Sites 950 and 953 only).

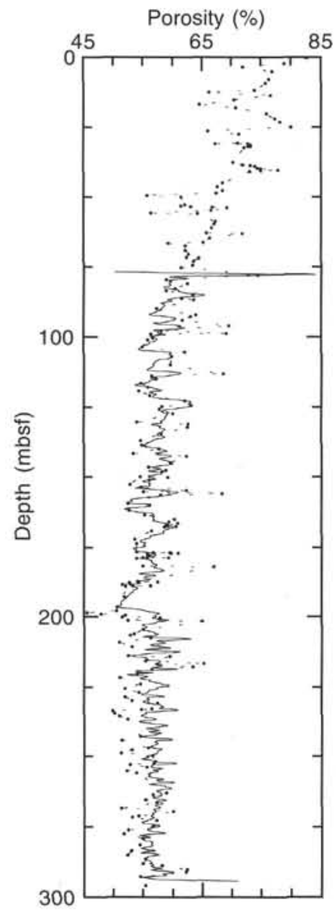

Figure 37. Hole 952A porosity derived from the medium phaser induction of the DIT, compared with porosity measurements on discrete core samples. The input resistivity data and the final porosity log are unsmoothed.

Table 13. Datum levels used in calculation of sediment accumulation rate curves.

	Event	Sample (cm) Top	Sample (cm) Bottom	Depth (mbsf) Top	Depth (mbsf) Bottom	Pelagic depth (m) Top	Pelagic depth (m) Bottom	Age (Ma)
		157-952A-	157-952A-					
1	LO *P. lacunosa*	3H-5, 111	3H-6, 72	26.41	27.52	1.99	2.61	0.46
2	Brunhes bottom	4H-6, 70–90	—	37.00	—	3.26	—	0.78
3	LO *R. asanoi*	4H-2, 48	4H-3, 69	30.78	32.49	2.88	3.04	0.83
4	Jaramillo top	6H-2, 15–50	—	49.00	—	4.50	—	0.99
5	Jaramillo bottom	6H-6, 40–60	—	55.50	—	5.84	—	1.07
6	LO *Gephyrocapsa* spp. (>5.5 µm)	6H-3, 39	6H-6, 43	51.19	55.73	4.75	5.86	1.24
7	Olduvai top	8H-1, 20	—	67.00	—	8.04	—	1.77
8	FO *G. truncatulinoides*	8H-4, 12–14	8H-6, 32–34	71.42	74.62	8.28	9.57	1.92
9	LO *D. brouweri*	8H-5, 18	8H-6, 68	72.98	74.98	8.40	9.81	1.95
10	Olduvai bottom	8H-6, 30	9H-2, 80	74.5	78.50	8.5	10.28	1.95
11	FO *D. triradiatus*	9H-2, 116	9H-5, 14.5	78.96	82.45	10.35	10.55	2.15
12	FO *G. inflata*	10H-6, 30–32	11H-2, 68–70	93.60	97.48	11.19	11.47	2.19
13	LO *D. pentaradiatus*	9H-6, 127.5	10H-1, 108.5	85.08	86.89	10.81	11.15	2.44
14	Gauss top	10H-1, 60	10H-6, 120	86.40	94.50	11.05	11.21	2.60
15	LO *D. surculus*	10H-1, 108.5	10H-6, 119	86.89	94.49	11.15	11.21	2.61
16	LO *D. tamalis*	10H-6, 119	11H-2, 70	94.49	97.50	11.21	11.97	2.76
17	LO *R. pseudoumbilicus*	13H-6, 89	14H-2, 17	122.69	125.47	12.13	12.24	3.77
18	FO *D. tamalis*	15H-3, 61	15H-5, 120	136.91	140.62	12.59	12.87	4.01
19	LO *Amaurolithus* spp.	15H-5, 120	16X-2, 83	140.62	145.13	12.87	12.97	4.39
20	FO *D. asymmetricus*	18X-4, 91	19X-1, 115	161.01	166.35	13.68	14.03	4.79
21	FO *C. rugosus*	19X-1, 115	19X-6, 58	166.35	173.28	14.03	14.35	5.04
22	LO *D. quinqueramus*	20X-CC, 2	22X-7, 28.5	184.33	203.39	14.95	15.76	5.56
23	FO *D. quinqueramus*	26X-3, 91	29X-3, 103	236.61	265.63	17.60	19.88	8.40
24	FO *D. kugleri*	37X-3, 90	39X-5, 29.5	342.80	364.50	25.68	26.36	12.20
25	FO *R. pseudoumbilicus*	44X-6, 125	—	415.35		27.61	—	13.10

Notes: Numbers in left column refer to numbers in Figures 38–40. The pelagic depths refer to the depth of datum levels in the stacked pelagic sequence.

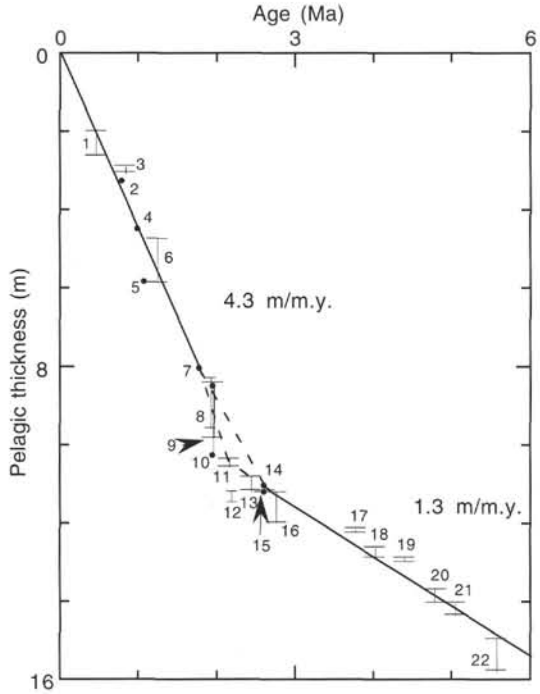

Figure 38. Sediment accumulation rates for the pelagic sequence of Hole 952A from zero to 6 Ma. Vertical bars represent distance between sample points. Numbers refer to datum levels given in Table 13.

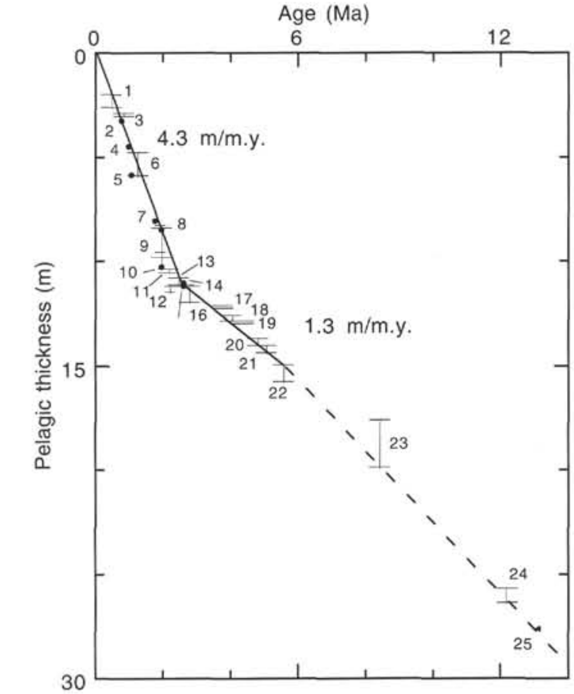

Figure 39. Sediment accumulation rates for the pelagic sequence of Hole 952A from zero to 14 Ma. Numbers refer to datum levels given in Table 13.

Table 14. Pyrolysis data from Rock-Eval analysis of sediment samples from Sites 950, 951, and 952.

Core, section, interval (cm)	Depth (mbsf)	T_{max} (°C)	S_1 (mgC/g)	S_2 (mgC/g)	S_3 (mgC/g)	TOC (wt%)	PC	HI	OI	PI	S_2/S_3
157-950A-											
4H-2, 60–61	30.00	403	1.32	4.89	3.98	1.95	0.51	250	204	0.21	1.22
18X-2, 100–101	157.00	391	0.13	0.19	2.11	0.58	0.02	32	363	0.41	0.09
28X-1, 48–49	247.00	419	0.60	2.49	3.05	1.75	0.25	142	174	0.19	0.81
29X-5, 64–65	262.00	424	0.95	3.76	2.15	1.89	0.39	198	113	0.20	1.74
30X-5, 65–66	272.00	412	0.94	3.27	2.74	1.88	0.35	173	145	0.22	1.19
32X-7, 21–22	294.00	415	0.57	2.26	2.59	1.58	0.23	143	163	0.20	0.87
157-951A-											
12H-4, 61–62	104.40	419	0.65	3.98	3.02	1.81	0.38	219	166	0.14	1.31
17X-1, 17–18	140.97	408	0.43	1.36	2.94	0.67	0.14	202	438	0.24	0.46
17X-4, 106–107	146.36	391	0.26	0.36	2.39	1.74	0.05	20	137	0.42	0.15
21X-2, 24–25	181.14	411	0.58	2.49	2.82	1.62	0.25	153	174	0.19	0.88
25X-3, 32–33	221.32	414	0.69	2.65	2.87	5.12	0.27	51	56	0.21	0.92
157-951B-											
1X-1, 48–49	255.48	415	0.55	2.25	2.51	1.62	0.23	138	154	0.20	0.89
3X-4, 94–95	279.74	421	0.61	2.64	2.40	1.53	0.27	172	156	0.19	1.10
6X-5, 58–59	309.78	408	0.67	2.23	2.89	1.79	0.24	124	161	0.23	0.77
8X-3, 99–100	326.49	406	0.14	0.34	2.37	0.65	0.04	52	364	0.29	0.14
157-952A-											
6H-5, 116–117	54.96	420	0.46	2.20	3.40	1.72	0.22	127	197	0.17	0.64
12H-3, 70–71	109.00	430	0.59	3.49	3.41	1.85	0.34	188	184	0.14	1.02
17X-1, 86–87	150.06	396	0.13	0.40	2.13	0.65	0.04	61	327	0.25	1.18
18X-5, 128–129	162.88	392	0.16	0.33	2.03	0.67	0.04	49	302	0.33	0.16
19X-3, 72–73	168.92	407	0.45	1.39	3.04	1.35	0.15	102	225	0.24	0.45
23X-6, 60–61	211.90	406	0.50	1.35	2.91	0.94	0.15	143	309	0.27	0.46
26X-1, 51–52	233.21	421	0.64	2.49	2.48	1.75	0.26	142	141	0.21	1.00
29X-5, 69–70	268.29	418	1.06	4.73	2.89	1.87	0.48	252	154	0.18	1.63
31X-1, 45–46	281.45	417	0.04	0.01	2.40	3.99	0.00	0	60	1.00	0.00
32X-4, 126–127	296.36	421	0.89	3.17	2.66	1.82	0.33	174	145	0.22	1.19
34X-5, 117–118	317.07	415	1.04	3.43	2.54	1.77	0.37	193	143	0.23	1.35
38X-5, 76–77	355.36	402	0.99	2.42	2.63	1.54	0.28	157	170	0.29	0.92
41X-3, 30–31	380.90	414	0.59	2.65	2.60	1.53	0.27	173	169	0.18	1.01
43X-3, 5–6	399.95	415	0.61	2.41	2.44	1.52	0.25	158	160	0.20	0.98
44X-4, 92–93	412.02	415	0.85	4.18	2.59	1.88	0.41	222	137	0.17	1.61
45X-2, 58–59	418.28	415	0.92	3.63	2.33	1.73	0.37	209	134	0.20	1.55
45X-3, 116–117	420.36	421	0.67	4.34	1.36	1.97	0.41	220	69	0.13	3.19

Notes: TOC = total organic carbon, PC = petroleum potential, HI = hydrogen index, OI = oxygen index, PI = production index.

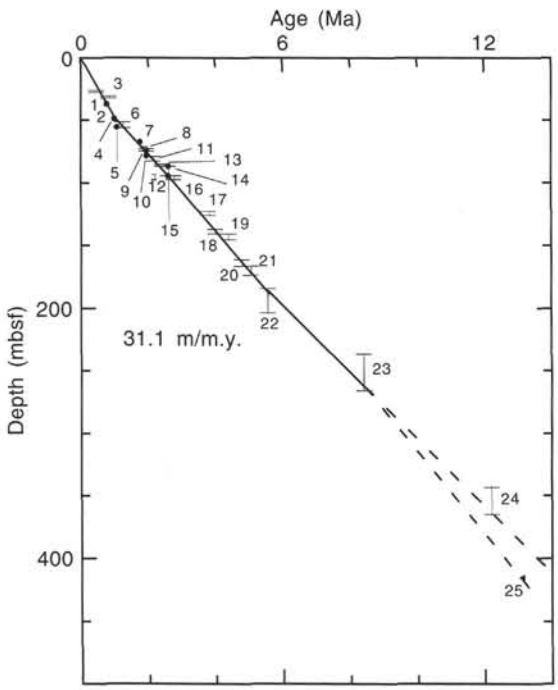

Figure 40. Sediment accumulation rates for the total sediment sequence of Holes 952A. Vertical bars represent distance between sample points. Numbers refer to datum levels given in Table 13.

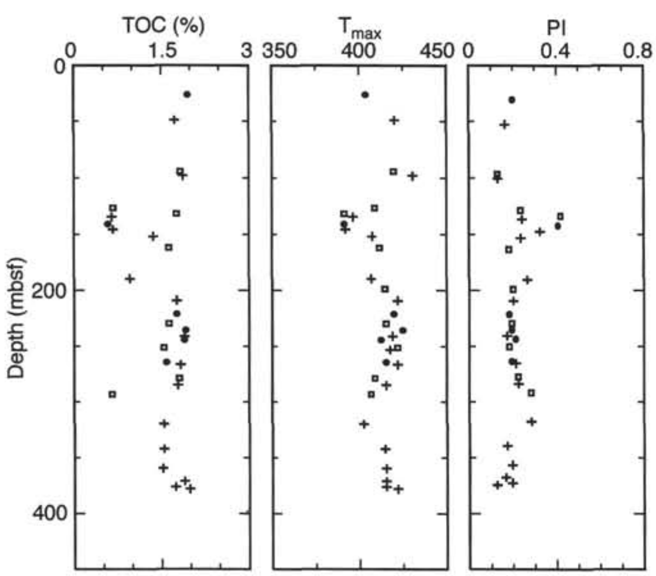

Figure 41. Variation of TOC, T_{max}, and production index (PI) as a function of depth. Filled circles = Site 950, open squares = Site 951, crosses = Site 952.

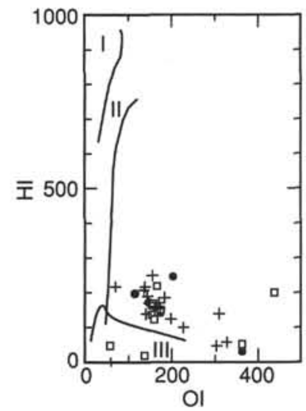

Figure 42. Hydrogen index (HI) as a function of oxygen index (OI). Filled circles = Site 950, open squares = Site 951, crosses = Site 952.

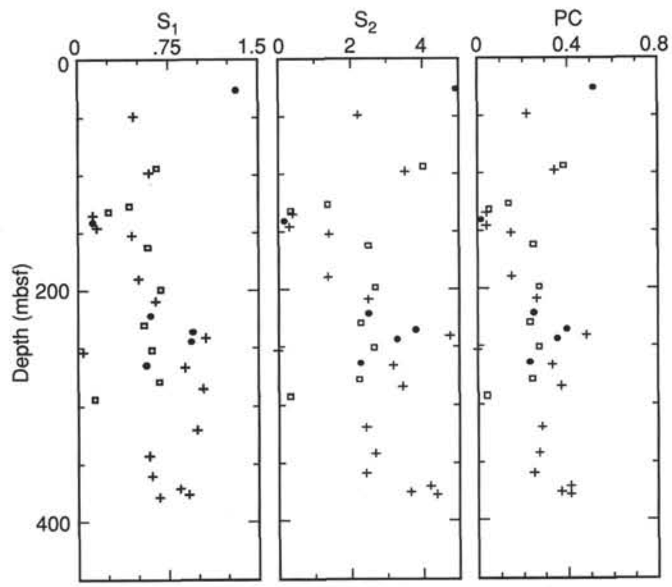

Figure 43. Variation of S_1 and S_2 and production capacity (PC) as a function of depth. Filled circles = Site 950, open squares = Site 951, crosses = Site 952.

SHORE-BASED LOG PROCESSING
HOLE 952A

Bottom felt: 5442.7 mbrf (used for depth shift to seafloor)
Total penetration: 425.9 mbsf
Total core recovered: 415.18 m (98%)

Logging Runs

Logging string 1: DIT/LSS/HLDT/CNTG/NGT (three sections)

Wireline heave compensator was used to counter ship heave resulting from the mild sea conditions (0.2–0.7 m).

Bottom-hole Assembly

The following bottom-hole assembly depths are as they appear on the logs after differential depth shift (see "Depth shift" section) and depth shift to the seafloor. As such, there might be a discrepancy with the original depths given by the drillers on board. Possible reasons for depth discrepancies are ship heave, use of wireline heave compensator, and drill string and/or wireline stretch.

DIT/LSS/HLDT/CNTG/NGT (main, upper section): Bottom-hole assembly at 92 mbsf.

DIT/LSS/HLDT/CNTG/NGT (repeat, upper section): Bottom-hole assembly at 76 mbsf.

DIT/LSS/HLDT/CNTG/NGT (lower section): Bottom-hole assembly at 181 mbsf.

Even though three intervals were logged, only the upper two have meaningful data. For this reason, these two zones are referred to as upper and lower section.

Processing

Depth shift: No differential depth shift necessary in the upper part of the hole. Upper and lower sections do no present sufficient overlap for depth correlation. All logs have been depth shifted to the seafloor (–5442.7 m).

Gamma-ray processing: NGT data have been processed to correct for borehole size and type of drilling fluid.

Acoustic data processing: No reprocessing necessary.

Quality Control

During the processing, quality control of the data is mainly performed by cross-correlation of all logging data. Large (>12 in.) and/or irregular borehole affects most recordings, particularly those that require eccentralization (CNTG, HLDT) and a good contact with the borehole wall.

Hole diameter was recorded by the hydraulic caliper on the HLDT tool (CALI), and the caliper on the FMS string (C1 and C2).

Data recorded through bottom-hole assembly should be used qualitatively only because of the attenuation on the incoming signal. NGT data were recorded through pipe in the 168–180 mbsf interval and above 76 mbsf.

Hole diameter was recorded by the hydraulic caliper on the HLDT tool (CALI). The data have been merged as follows:

Gamma ray: data spliced at 100 and 168 mbsf.

Density and caliper: data spliced at 125 mbsf.

Neutron: data spliced at 125 and 181 mbsf.

Resistivity: data spliced at 100 and 195 mbsf (no good deep resistivity [IDPH] recorded in the lower section).

Sonic: data spliced at 105 mbsf.

Note: Details of standard shore-based processing procedures are found in the "Explanatory Notes" chapter, this volume. For further information about the logs, please contact:

Cristina Broglia
Phone: 914-365-8343
Fax: 914-365-3182
E-mail: chris@ldeo.columbia.edu

Elizabeth Pratson
Phone: 914-365-8313
Fax: 914-365-3182
E-mail: beth@ldeo.columbia.edu

Hole 952A: Natural Gamma Ray-Resistivity-Sonic Logging Data

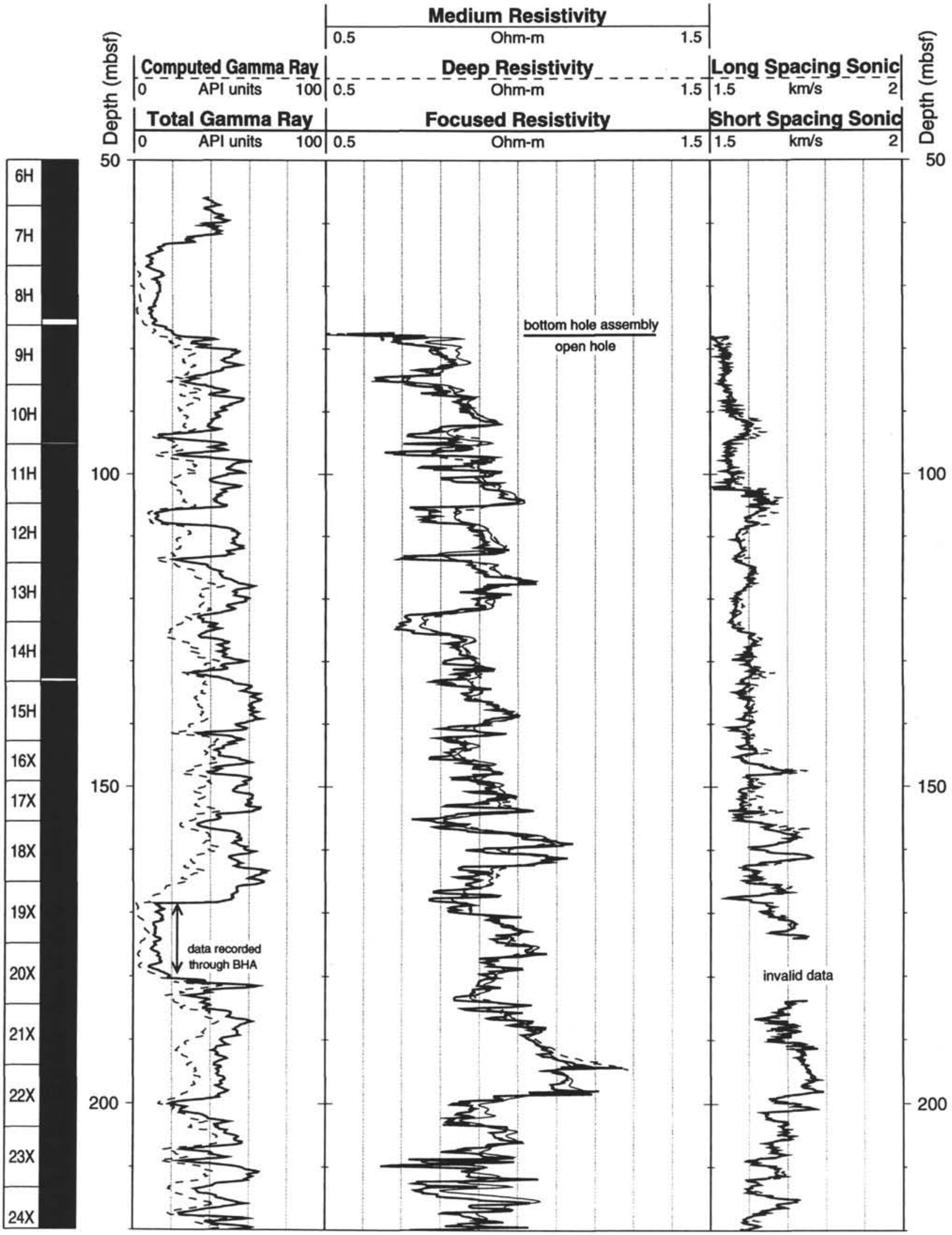

Hole 952A: Natural Gamma Ray-Resistivity-Sonic Logging Data (cont.)

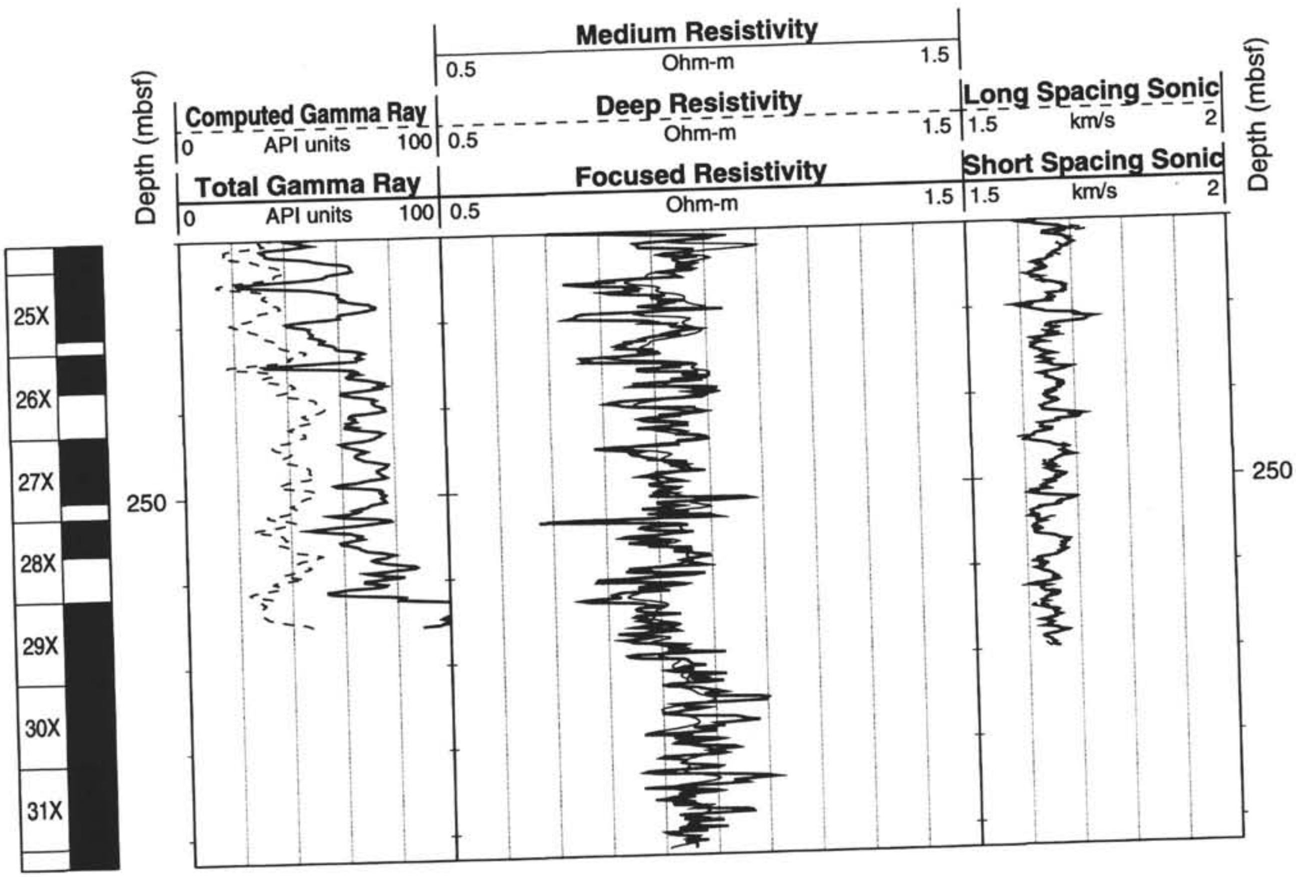

Hole 952A: Natural Gamma Ray-Density-Porosity Logging Data

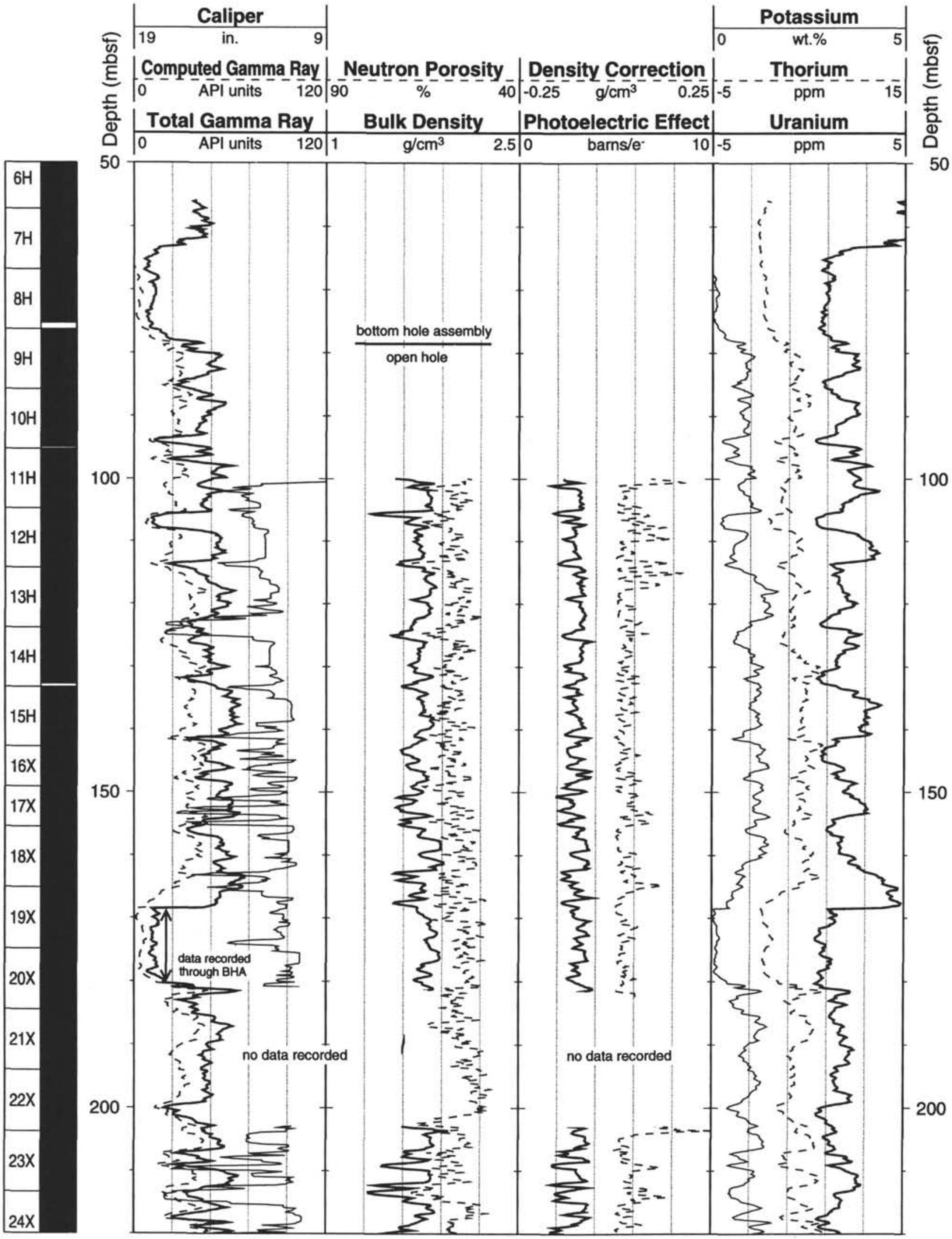

Hole 952A: Natural Gamma Ray-Density-Porosity Logging Data (cont.)